

8-27-2009

Indentation analysis and mechanical modeling of multilayered composites

Guanlin Tang

Follow this and additional works at: https://digitalrepository.unm.edu/me_etds

Recommended Citation

Tang, Guanlin. "Indentation analysis and mechanical modeling of multilayered composites." (2009).
https://digitalrepository.unm.edu/me_etds/3

This Dissertation is brought to you for free and open access by the Engineering ETDs at UNM Digital Repository. It has been accepted for inclusion in Mechanical Engineering ETDs by an authorized administrator of UNM Digital Repository. For more information, please contact disc@unm.edu.

GuanlinTang

Candidate

Mechanical Engineering

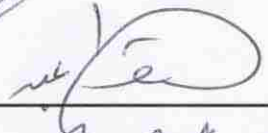
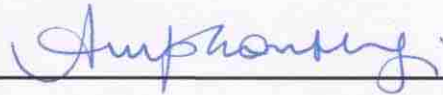
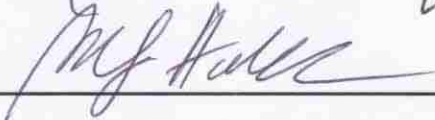
Department

This dissertation is approved, and it is acceptable in quality and form for publication:

Approved by the Dissertation Committee:



, Chairperson

 Tariq Khraishi

**INDENTATION ANALYSIS AND
MECHANICAL MODELING OF
MULTILAYERED NANOCOMPOSITES**

BY

GUANLIN TANG

B.S. Mechanical Engineering, Zhejiang University, 2002
M.S. Mechanical Engineering, University of New Mexico, 2004

DISSERTATION

Submitted in Partial Fulfillment of the
Requirements for the Degree of

**Doctor of Philosophy
Engineering**

The University of New Mexico
Albuquerque, New Mexico

August, 2009

2009, Guanlin Tang

DEDICATION

I would like to dedicate this dissertation to my parents Jitie Tang and Lijun Wang, and my husband Shuangwei Xie.

谨以此文献给我敬爱的父亲唐继铁,母亲王丽君和我的丈夫谢双伟。

ACKNOWLEDGMENTS

I heartily acknowledge Dr. Yu-Lin Shen, my advisor and dissertation chair, for encouraging me through the years of study and research.

I also thank my committee members Dr. Marwan Al-Haik, Dr. Tariq Khraishi and Dr. Arup K. Maji for their valuable insights and assistance in this study.

Gratitude is extended to National Science Foundation for supporting this research work.

**INDENTATION ANALYSIS AND
MECHANICAL MODELING OF
MULTILAYERED NANOCOMPOSITES**

BY

GUANLIN TANG

ABSTRACT OF DISSERTATION

Submitted in Partial Fulfillment of the
Requirements for the Degree of

**Doctor of Philosophy
Engineering**

The University of New Mexico
Albuquerque, New Mexico

August 2009

INDENTATION ANALYSIS AND MECHANICAL MODELING OF MULTILAYERED NANOCOMPOSITES

by

Guanlin Tang

B.S., Mechanical Engineering, Zhejiang University, 2002

M.S., Mechanical Engineering, University of New Mexico, 2004

Ph.D., Mechanical Engineering, University of New Mexico, 2009

ABSTRACT

A numerical study was undertaken to investigate the mechanical properties of metal-ceramic nanolayered composites. The model system features alternating thin films of aluminum (Al) and silicon carbide (SiC). Finite element modeling was employed to analyze the nanoindentation and microcompression behavior. This modeling study treats the heterogeneous structure of the material explicitly, and seeks to correlate the overall material response with the intrinsic deformation characteristics.

We first report on the nanoindentation behavior of the Al/SiC composites. Two material systems were considered: Al/SiC multilayers free of substrate and Al/SiC above the silicon (Si) substrate. The numerical model features a conical indenter within the axisymmetric simulation framework. For the Al/SiC multilayers free of substrate, a valid composite elastic response can be retrieved beyond a certain depth. The effective modulus was found to be

representative of the out-of-plane modulus of the multilayer composite. For the Al/SiC multilayers above Si substrate, the effects of the substrate material and heterogeneity of the composite play an important role in the modulus and hardness determination. Significant tensile stresses can be generated locally along certain directions. The unloading process leads to an expansion of the tension-stressed area and continuation of plastic flow in parts of the Al layers. The unloading response is therefore much more complex than the conventional elastic recovery process as seen in homogeneous materials.

Attention was then turned to the viscoplastic effects during indentation. Within the present modeling framework, we found that a hold time at the peak load can help to obtain a reliable hardness value, while elastic modulus does not seem to be affected by the hold. The multilayers display a less significant time-dependent behavior, compared to the case of a single-layer material.

Finally we report on the composite pillar behavior under micro-compression tests. It was found that the base material connected to the pillar plays a significant role in the measured mechanical response. It is essential to take into account the base and indenter compliances to obtain a reliable stress-strain relationship. The multilayered pillar deforms in a non-uniform way under compression, especially when a tapered side wall included in the numerical model.

TABLE OF CONTENTS

DEDICATION	IV
ACKNOWLEDGMENTS	V
ABSTRACT	VII
LIST OF FIGURES.....	XII
LIST OF TABLES	XVIII
CHAPTER 1 INTRODUCTION	1
CHAPTER 2 LITERATURE REVIEW	4
CHAPTER 3 BACKGROUND STUDY: HOMOGENEOUS MATERIALS AND SIMPLE FILM- SUBSTRATE SYSTEMS	11
3.1 MODEL	11
3.2 INDENTATION MODELING.....	12
3.3 NUMERICAL RESULTS	15
<i>a) Material properties</i>	15
<i>b) Calibration of β factor</i>	17
<i>c) Substrate effects</i>	19
<i>d) Effects of plastic properties of Al</i>	21
<i>e) SiC film on Si substrate</i>	22
<i>f) Indenter size effects</i>	23
3.4 CONCLUSIONS.....	26
CHAPTER 4 EFFECTIVE ELASTIC RESPONSE OF “INFINITE” LAYERS	27
4.1 OVERALL ELASTIC PROPERTIES.....	27
4.2 INDENTATION MODELING.....	32
4.3 NUMERICAL RESULTS	34

<i>a) Overall elastic properties</i>	34
<i>b) Indentation analysis of Al₅₀/SiC₅₀ composite</i>	36
<i>c) Other Al/SiC thickness ratios</i>	39
4.4 CONCLUSIONS	41
CHAPTER 5 EFFECTIVE INDENTATION RESPONSE OF “FINITE” LAYERS	42
5.1 EXPERIMENTAL BACKGROUND	42
5.2 INDENTATION MODELING	43
<i>a) 7-layer Al/SiC on Si</i>	45
<i>b) 41-layer Al/SiC on Si</i>	46
5.3 NUMERICAL RESULTS	46
<i>a) 7 layer Al/SiC on Si</i>	46
<i>b) 41-layer Al/SiC on Si</i>	53
5.4 CONCLUSIONS	62
CHAPTER 6 ANALYSIS OF INDENTATION INDUCED DEFORMATION FIELD AND LOCAL DAMAGE	64
6.1 EXPERIMENT OBSERVATIONS	64
6.2 NUMERICAL SIMULATIONS	65
<i>a) Stress and deformation contours</i>	65
<i>b) History of stress and strain</i>	77
<i>c) Correlation with local damages</i>	82
6.3 CONCLUSIONS	83
CHAPTER 7 LOADING RATE EFFECTS	85
7.1 MODEL	85
7.2 NUMERICAL RESULTS	89
<i>(a) Load-displacement curve of Al/Si model</i>	89
<i>(b) Young’s modulus and hardness of the Al/Si model</i>	102

(c) <i>Load-displacement curve of the Multilayer/Si model</i>	103
(d) <i>Young's modulus and hardness of the multilayer/Si model</i>	109
7.3 CONCLUSIONS.....	110
CHAPTER 8 MICROCOMPRESSION OF PILLARS	111
8.1 NUMERICAL SIMULATION OF SI PILLAR.....	111
(a) <i>Base height effect of Si pillar model</i>	112
(b) <i>Base width effect of the Si pillar model</i>	116
(c) <i>Friction and fillets</i>	117
8.2 NUMERICAL SIMULATION OF THE AL/SiC PILLAR	118
(a) <i>Elastic modulus of the multilayer composite pillar</i>	118
(b) <i>Elastic modulus of the multilayer composite pillar with taper</i>	121
(c) <i>Stress and deformation evolutions</i>	124
8.3 COMPARISON WITH EXPERIMENTS	127
8.4 CONCLUSIONS.....	128
CHAPTER 9 CONCLUSIONS AND FUTURE WORK	130
REFERENCES	134

LIST OF FIGURES

FIGURE 1.1: SCANNING ELECTRON MICROGRAPHS OF AL/SiC MULTILAYERS CROSS-SECTIONED BY FOCUSED ION BEAM (FIB): (A) 7-LAYER AL₅₀SiC₅₀ AND (B) 41 LAYER AL₅₀SiC₅₀, COURTESY OF N. CHAWLA AND D. R. P. SINGH3

FIGURE 2.1: SCHEMATIC OF A NANOINDENTER [38].5

FIGURE 2.2: SCHEMATICS OF INDENTER WITH DIFFERENT TIPS.6

FIGURE 2.3: SCHEMATIC OF THE BERKOVICH INDENTER (A) INDENTER IMPRESSION TIP WITH THE FACE ANGLE OF 65.3° AND THE CONTACT DEPTH OF HC. (B) TOP VIEW OF THE IMPRESSION AREA [90].7

FIGURE 2.4: SCHEMATIC OF CONTACT BETWEEN A SPECIMEN AND A CONICAL INDENTER DURING AN INDENTATION TEST [39].8

FIGURE 3.1: (A) SCHEMATIC SHOWING A HOMOGENEOUS BLOCK. (B) SCHEMATIC SHOWING A SINGLE FILM ON SUBSTRATE.11

FIGURE 3.2: (A) SCHEMATIC SHOWING THE SPECIMEN OF PURE AL AND THE BOUNDARY CONDITIONS FOR INDENTATION MODELING. THE SPECIMEN AND INDENTER BOTH POSSESS AXIAL SYMMETRY ABOUT THE LEFT BOUNDARY. THE RIGID INDENTER HAS A SEMI-ANGLE OF 70.3°. (B) SCHEMATIC SHOWING THE SPECIMEN OF A SINGLE FILM ON SI SUBSTRATE WITH ALL OTHER CONDITIONS THE SAME AS IN (A).12

FIGURE 3.3: (A) A REPRESENTATIVE MESH OF A SINGLE AL FILM ON SI SUBSTRATE. (B) DETAILED MESH AT THE UPPER LEFT CORNER OF THE MODEL IN (A).15

FIGURE 3.4: (A) STRESS-STRAIN RESPONSE OF AL (B) STRESS-STRAIN RESPONSE OF SiC, USED AS INPUT IN THE FINITE ELEMENT MODELING.16

FIGURE 3.5: A REPRESENTATIVE INDENTATION LOAD-DISPLACEMENT RESPONSE OBTAINED FROM THE FINITE ELEMENT MODELING. THIS CURVE CORRESPONDS TO THE HOMOGENEOUS MODEL OF PURE AL, WITH THE MAXIMUM INDENTATION DEPTH AT 700 NM.18

FIGURE 3.6: NUMERICAL RESULT SHOWING THE INDENTATION DERIVED YOUNG’S MODULUS OF AL AS A FUNCTION OF THE INDENTATION DEPTH WITH $\beta = 1.06$ FOR THE RIGID INDENTER.18

FIGURE 3.7: INDENTATION-DERIVED ELASTIC MODULUS AS A FUNCTION OF THE INDENTATION DEPTH FOR AL ON SI.19

FIGURE 3.8: INDENTATION-DERIVED HARDNESS AS A FUNCTION OF THE INDENTATION DEPTH FOR AL ON SI.	20
FIGURE 3.9: INDENTATION-DERIVED ELASTIC MODULUS AS A FUNCTION OF THE INDENTATION DEPTH FOR AL WITH DIFFERENT YIELD STRENGTH ON SI.	22
FIGURE 3.10: INDENTATION-DERIVED ELASTIC MODULUS AS A FUNCTION OF THE INDENTATION DEPTH FOR SiC ON SI.	23
FIGURE 3.11: SCHEMATIC OF THE ELASTIC INDENTERS.	24
FIGURE 3.12: (A) ELASTIC MODULUS AS A FUNCTION OF THE INDENTATION DEPTH FOR DIFFERENT INDENTERS (B) HARDNESS AS A FUNCTION OF THE INDENTATION DEPTH FOR DIFFERENT INDENTERS.	25
FIGURE 4.1: SCHEMATIC SHOWING THE ALTERNATING METAL-CERAMIC LAYERS CONSIDERED IN THIS STUDY.	28
FIGURE 4.2: SCHEMATICS SHOWING THE (A) LONGITUDINAL AND (B) TRANSVERSE LOADING CONFIGURATIONS FOR MODELING THE OVERALL ELASTIC RESPONSE OF THE MULTILAYERED COMPOSITE.	31
FIGURE 4.3: SCHEMATIC SHOWING THE MULTILAYER MODEL AND THE BOUNDARY CONDITIONS FOR INDENTATION MODELING. THE SPECIMEN AND INDENTER BOTH POSSESS AXIAL SYMMETRY ABOUT THE LEFT BOUNDARY. THE RIGID INDENTER HAS A SEMI-ANGLE OF 70.3°.	34
FIGURE 4.4: NUMERICAL RESULT SHOWING THE OVERALL YOUNG’S MODULUS ALONG THE LONGITUDINAL DIRECTION (E_{11}) AND TRANSVERSE DIRECTION (E_{22}) OF THE AL/SiC MULTILAYERS. FOR COMPARISON THE MODULUS VALUES BASED ON THE ONE-DIMENSIONAL ASSUMPTION (EQUATIONS (4.4) AND (4.5)) ARE ALSO INCLUDED.	35
FIGURE 4.5: A REPRESENTATIVE INDENTATION LOAD-DISPLACEMENT RESPONSE OBTAINED FROM THE FINITE ELEMENT MODELING. THIS CURVE CORRESPONDS TO THE MULTILAYER MODEL AL50/SiC50, WITH THE MAXIMUM INDENTATION DEPTH AT 100 NM.	37
FIGURE 4.6: INDENTATION-DERIVED ELASTIC MODULUS, OBTAINED FROM THE FINITE ELEMENT ANALYSIS, OF THE AL50/SiC50 COMPOSITE AS A FUNCTION OF THE INDENTATION DEPTH. THE RESULT OF PURE AL IS ALSO INCLUDED FOR REFERENCE. IN ADDITION TO THE HOMOGENIZED MODEL, TWO CURVES FOR THE MULTILAYER MODEL ARE PRESENTED: ONE WITH AL BEING THE TOPMOST LAYER AND THE OTHER WITH SiC BEING THE TOPMOST LAYER.	38

FIGURE 4.7: INDENTATION-DERIVED ELASTIC MODULUS AS A FUNCTION OF THE INDENTATION DEPTH FOR THE COMPOSITES AL75/SiC25, AL50/SiC50 AND AL25/SiC75.	39
FIGURE 4.8: COMPARISON OF THE OVERALL LONGITUDINAL MODULUS E_{11} AND TRANSVERSE MODULUS E_{22} WITH THE INDENTATION-DERIVED MODULUS VALUES OF THE COMPOSITES AL75/SiC25, AL50/SiC50 AND AL25/SiC75.....	40
FIGURE 5.1: SCHEMATIC SHOWING THE ALTERNATING METAL-CERAMIC LAYERS ON SUBSTRATE CONSIDERED IN THIS STUDY.	43
FIGURE 5.2: SCHEMATIC SHOWING THE MULTILAYER ON SUBSTRATE MODEL AND THE BOUNDARY CONDITIONS FOR INDENTATION MODELING. THE SPECIMEN AND INDENTER BOTH POSSESS AXIAL SYMMETRY ABOUT THE LEFT BOUNDARY. THE RIGID INDENTER HAS A SEMI-ANGLE OF 70.3°	44
FIGURE 5.3: EXPERIMENTAL AND MODELING RESULTS OF THE YOUNG’S MODULUS AS A FUNCTION OF INDENTATION DEPTH FOR THE (A) AL50/SiC30, (B) AL50/SiC50 AND (C) AL50/SiC70 MATERIALS.....	48
FIGURE 5.4: COMPARISON OF ELASTIC MODULUS OBTAINED FROM EXPERIMENTAL INDENTATION MEASUREMENT (“EXPT”), INDENTATION MODELING (“FEM”), AND MODELING OF OVERALL COMPOSITE MODULUS (“E11” AND “E22”) WHEN THE INDENTATION DEPTH IS AT (A) 18 NM, (B) 23 NM, (C) 42 NM AND (D) 60 NM.	52
FIGURE 5.5: SIMULATED LOAD-DISPLACEMENT CURVE DURING INDENTATION LOADING AND UNLOADING.	53
FIGURE 5.6: SCHEMATICS SHOWING THE TWO ADDITIONAL MODELS: (A) THE 41 LAYERS OF AL/SiC IS REPLACED BY THE HOMOGENIZED AL/SiC COMPOSITE ABOVE THE Si SUBSTRATE; (B) THE ENTIRE MATERIAL IS THE HOMOGENIZED AL/SiC COMPOSITE.	55
FIGURE 5.7: SIMULATED INDENTATION HARDNESS AS A FUNCTION OF INDENTATION DEPTH, FOR THE THREE MODELS “AL/SiC MULTILAYERS ON Si” (FIGURE 1), “HOMOGENIZED AL/SiC ON Si” (FIGURE 10(A)), AND “HOMOGENIZED AL/SiC” (FIGURE 10(B)).....	57
FIGURE 5.8: SIMULATED ELASTIC MODULUS AS A FUNCTION OF INDENTATION DEPTH OBTAINED FROM THE SIMULATED UNLOADING PART OF THE INDENTATION CURVE, FOR THE THREE MODELS “AL/SiC MULTILAYERS ON Si” (FIGURE 5.2), “HOMOGENIZED AL/SiC ON Si” (FIGURE 5.7(A)), AND “HOMOGENIZED AL/SiC” (FIGURE 5.7(B)).....	59

FIGURE 5.9: COMPARISON OF EXPERIMENTAL AND MODELING RESULTS ON THE HARDNESS AS A FUNCTION OF INDENTATION DEPTH.....	61
FIGURE 5.10: COMPARISON OF EXPERIMENTAL AND MODELING RESULTS ON THE INDENTATION-DERIVED YOUNG’S MODULUS AS A FUNCTION OF INDENTATION DEPTH.....	61
FIGURE 6.1: CROSS-SECTION IMAGE SHOWING INTERNAL DAMAGE UNDER THE INDENTATION IN THE AL/SiC NANOLAYERS. CRACKS IN THE AL LAYER AND AT THE MULTILAYERS/SUBSTRATE INTERFACE ARE VISIBLE, COURTESY OF N. CHAWLA AND D. R. P. SINGH.....	65
FIGURE 6.2 CONTOURS OF HYDROSTATIC STRESS NEAR THE INDENTATION SITE, WHEN THE INDENTATION DEPTH IS AT (A) 200 NM, (B) 500 NM, AND (C) AFTER UNLOADING.....	68
FIGURE 6.3 CONTOURS OF EQUIVALENT PLASTIC STRAIN NEAR THE INDENTATION SITE, WHEN THE INDENTATION DEPTH IS AT (A) 200 NM, (B) 500 NM, AND (C) AFTER UNLOADING.....	70
FIGURE 6.4 CONTOURS OF MAXIMUM PRINCIPAL STRESS NEAR THE INDENTATION SITE, WHEN THE INDENTATION DEPTH IS AT (A) 200 NM, (B) 500 NM, AND (C) AFTER UNLOADING.....	72
FIGURE 6.5 CONTOURS OF Σ_{22} NEAR THE INDENTATION SITE, WHEN THE INDENTATION DEPTH IS AT (A) 200 NM, (B) 500 NM, AND (C) AFTER UNLOADING. THE CONTOUR LEVELS ARE ADJUSTED TO HIGHLIGHT THE REGION WITH TENSILE STRESSES.....	74
FIGURE 6.6 CONTOURS OF SHEAR STRESS Σ_{12} NEAR THE INDENTATION SITE, WHEN THE INDENTATION DEPTH IS AT (A) 200 NM, (B) 500 NM, AND (C) AFTER UNLOADING.....	76
FIGURE 6.7 EVOLUTION OF (A) EQUIVALENT PLASTIC STRAIN AND (B) SEVERAL STRESS COMPONENTS OF A MATERIAL ELEMENT, INSIDE AN AL LAYER IN THE REGION HIGHLIGHTED BY THE RIGHT CIRCLE IN FIGURE 6.3 (B), DURING THE INDENTATION HISTORY. THE SYMBOLS VM, S12, S33, S11 AND S22 IN (B) REFER TO THE VON MISES EFFECTIVE STRESS AND THE STRESS COMPONENTS Σ_{12} , Σ_{33} , Σ_{11} AND Σ_{22} , RESPECTIVELY....	79
FIGURE 6.8 EVOLUTION OF (A) EQUIVALENT PLASTIC STRAIN AND (B) SEVERAL STRESS COMPONENTS OF A MATERIAL ELEMENT, INSIDE AN AL LAYER IN THE REGION HIGHLIGHTED BY THE LEFT CIRCLE IN FIGURE 6.3 (B), DURING THE INDENTATION HISTORY. THE SYMBOLS VM, S12, S33, S11 AND S22 IN (B) REFER TO THE VON MISES EFFECTIVE STRESS AND THE STRESS COMPONENTS Σ_{12} , Σ_{33} , Σ_{11} AND Σ_{22} , RESPECTIVELY.....	81

FIGURE 7.1: SCHEMATICS SHOWING THE TWO RATE DEPENDENT MODELS: (A) SINGLE AL FILM ABOVE THE SI SUBSTRATE; (B) AL/SiC COMPOSITE ABOVE THE SI SUBSTRATE.	86
FIGURE 7.2: LOAD-DISPLACEMENT CURVES OF THE AL/SI MODEL WITH LOADING RATES OF 10 μ N/S AND 1 μ N/S (A) OVERALL CURVE (B) BEGINNING PART OF THE UNLOADING CURVE.	90
FIGURE 7.3: LOAD-DISPLACEMENT CURVES OF THE AL/SI MODEL WITH LOADING RATES OF 10 μ N/S AND 1 μ N/S WITH 10 S HOLDING TIME(A) OVERALL CURVE (B) BEGINNING PART OF THE UNLOADING CURVE.....	91
FIGURE 7.4: LOAD-DISPLACEMENT CURVES OF THE AL/SI MODEL WITH LOADING RATE OF 1 μ N/S WITH NO HOLDING TIME AND 10 S HOLDING TIME (A) OVERALL CURVE (B) BEGINNING PART OF THE UNLOADING CURVE.....	93
FIGURE 7.5: LOAD-DISPLACEMENT CURVES OF THE AL/SI MODEL WITH LOADING RATE OF 10 μ N/S WITH NO HOLDING TIME AND 10 S HOLDING TIME (A) OVERALL CURVE (B) BEGINNING PART OF THE UNLOADING CURVE.....	94
FIGURE 7.6: LOAD-DISPLACEMENT CURVES OF AL ON SI MODEL WITH LOADING RATES OF 10 μ N/S AND 1 10 μ N/S (A) OVERALL CURVE (B) BEGINNING PART OF THE UNLOADING CURVE.	97
FIGURE 7.7: LOAD-DISPLACEMENT CURVES OF AL ON SI MODEL WITH LOADING RATES OF 1 μ N/S AND 10 μ N/S WITH 10 S HOLDING TIME(A) OVERALL CURVE (B) BEGINNING PART OF THE UNLOADING CURVE.....	98
FIGURE 7.8: LOAD-DISPLACEMENT CURVES OF AL ON SI MODEL WITH LOADING RATE OF 1 μ N/S WITH NO HOLDING TIME AND 10 S HOLDING TIME (A) OVERALL CURVE (B) BEGINNING PART OF THE UNLOADING CURVE.....	100
FIGURE 7.9: LOAD-DISPLACEMENT CURVES OF AL ON SI MODEL WITH LOADING RATE OF 10 μ N/S WITH NO HOLDING TIME AND 10 S HOLDING TIME (A) OVERALL CURVE (B) BEGINNING PART OF THE UNLOADING CURVE.....	101
FIGURE 7.10: LOAD-DISPLACEMENT CURVES OF 41-LAYER AL/SiC ON SI MODEL WITH LOADING RATES OF 10 μ N/S AND 1 μ N/S (A) OVERALL CURVE (B) BEGINNING PART OF THE UNLOADING CURVE.	105
FIGURE 7.11: LOAD-DISPLACEMENT CURVES OF 41-LAYER AL/SiC ON SI MODEL WITH LOADING RATES OF 10 μ N/S AND 1 μ N/S WITH 10 S HOLDING TIME (A) OVERALL CURVE (B) BEGINNING PART OF THE UNLOADING CURVE.....	106

FIGURE 7.12: LOAD-DISPLACEMENT CURVES OF 41-LAYER AL/SiC ON Si MODEL WITH LOADING RATE OF 1 μ N/S WITH NO HOLDING TIME AND 10 S HOLDING TIME (A) OVERALL CURVE (B) BEGINNING PART OF THE UNLOADING CURVE.....	107
FIGURE 7.13: LOAD-DISPLACEMENT CURVES OF 41-LAYER AL/SiC ON Si MODEL WITH LOADING RATE OF 10 μ N/S WITH NO HOLDING TIME AND 10 S HOLDING TIME (A) OVERALL CURVE (B) BEGINNING PART OF THE UNLOADING CURVE.....	108
FIGURE 8.1: SCHEMATICS SHOWING MICROCOMPRESSION ON A PILLAR WITH BASE.	111
FIGURE 8.2: SCHEMATICS SHOWING THE TWO PILLAR MODEL: (A) SINGLE PILLAR UNDER MICROCOMPRESSION; (B) PILLAR WITH BASE UNDER MICROCOMPRESSION.....	112
FIGURE 8.3 REPRESENTATIVE STRESS-STRAIN CURVE OF MICROCOMPRESSION SIMULATION ON Si.....	113
FIGURE 8.4: A) SIMULATED MODULUS VALUES OF Si PILLAR WITH DIFFERENT BASE HEIGHTS AND ASPECT RATIOS. B) THE SAME DATA PRESENTED IN A DIFFERENT GRAPHICAL FORM.....	115
FIGURE 8.5: SIMULATED MODULUS OF Si PILLAR WITH DIFFERENT BASE WIDTHS AND ASPECT RATIOS.	117
FIGURE 8.6: SCHEMATICS SHOWING THE AL/SiC MULTILAYER PILLAR ON A Si BASE.....	119
FIGURE 8.7: STRESS STRAIN CURVES OF MULTILAYER PILLAR MODEL AND TRUE COMPOSITE.	121
FIGURE 8.8: SCHEMATICS SHOWING THE PILLAR MODEL WITH TAPER	122
FIGURE 8.9: STRESS STRAIN CURVES OF MULTILAYER PILLAR WITH TAPER ANGLE OF 1°, 2° AND 4°.....	123
FIGURE 8.10: EQUIVALENT PLASTIC STRAIN OF THE PURE AL PILLAR AT COMPRESSION DEPTHS OF (A) 100 NM AND (B) 325 NM.	125
FIGURE 8.11: EQUIVALENT PLASTIC STRAIN OF THE PURE AL PILLAR WITH A 2° TAPER ANGLE AT COMPRESSION DEPTHS OF (A) 100 NM. AND (B) 325 NM.	125
FIGURE 8.12: VON MISES STRESS CONTOURS OF THE AL/SiC MULTILAYER PILLAR ON A Si BASE AT COMPRESSION DEPTHS OF (A) 100 NM, (B) 200 NM, AND (C) 325 NM.	126
FIGURE 8.13: VON MISES STRESS CONTOURS OF THE AL/SiC MULTILAYER PILLAR ON A Si BASE WITH A 2° TAPER ANGLE AT COMPRESSION DEPTH OF (A) 100 NM, (B) 200 NM, AND (C) 325 NM.	127
FIGURE 8.14: SEM IMAGES OF MULTILAYER PILLAR STRUCTURE (A) BEFORE COMPRESSION, AND (B) AFTER COMPRESSION, COURTESY OF N. CHAWLA AND D. R. P. SINGH.....	128

LIST OF TABLES

TABLE 4.1 FIVE INDEPENDENT ELASTIC CONSTANTS FOR THE THREE COMPOSITE MODELS: AL75/SiC25, AL50/SiC50 AND AL25/SiC75.	36
TABLE 7.1 PLASTIC PROPERTY OF AL AT STRAIN RATE OF 10^{-6}	88
TABLE 7.2 STRAIN RATE HARDENING	88
TABLE 7.3 MODULUS OF THE AL/SI MODEL	102
TABLE 7.4 HARDNESS OF THE AL/SI MODEL	103
TABLE 7.5 MODULUS OF 41 LAYER AL/SiC ON SI	109
TABLE 7.6 HARDNESS OF 41 LAYER AL/SiC ON SI	110
TABLE 8.1 YOUNG’S MODULUS OF SI PILLAR WITH A BASE WIDTH OF 500 μM	114
TABLE 8.2 YOUNG’S MODULUS OF SI PILLAR WITH A BASE HEIGHT OF 500 μM	116
TABLE 8.3 YOUNG’S MODULUS OF THE MULTILAYER PILLAR (FIGURE 8.6).....	120
TABLE 8.4 YOUNG’S MODULUS OF MULTILAYER PILLAR WITH TAPER.....	124

Chapter 1 Introduction

In the past several decades, the quality of our lives has been significantly improved by the inventions of various devices, including medical devices, computers, cell phones and satellite services. All these inventions are based on the development of novel materials: new metal alloys, new ceramics and polymers, and new biomaterials.

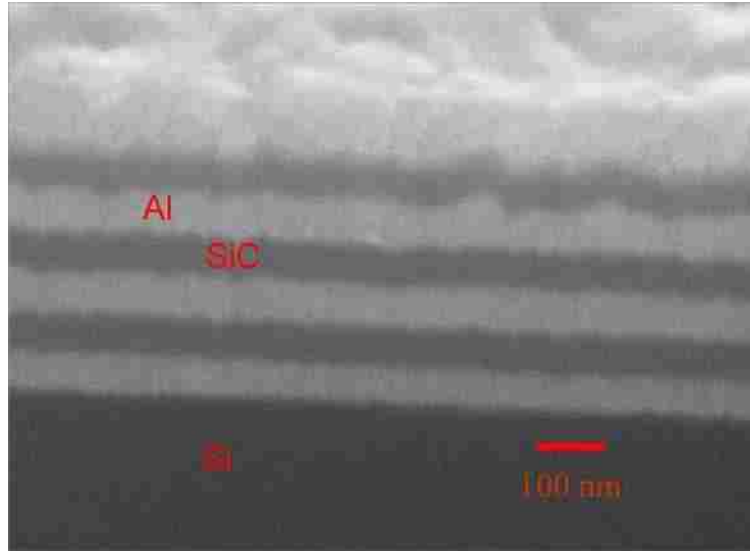
Most of the novel materials being studied today are small scaled materials, in some cases, nanomaterials. Nanomaterials are called “the future of materials”. Nanotechnology is an emerging and rapidly growing field. Generally materials or devices with the feature size of 100 nanometers or smaller, can be called nanomaterials or nanodevices. Many of the devices and systems used in modern industry are already in the nano-scale domain.

Nanomaterials may possess advantages of extremely high strength, fatigue resistance, thermal resistance, wear resistance and bio-compatibility, compared with traditional material. The current research interests on nanomaterials generally encompass the following three major areas: synthesis and fabrication, properties and characterization, and applications. Synthesis techniques include various physical and chemical processes as well as lithography. The properties include mechanical, thermal, chemical, electronic, magnetic, and optical, among others. Nanomaterials are finding applications in area spanning from structural coatings to microelectronics.

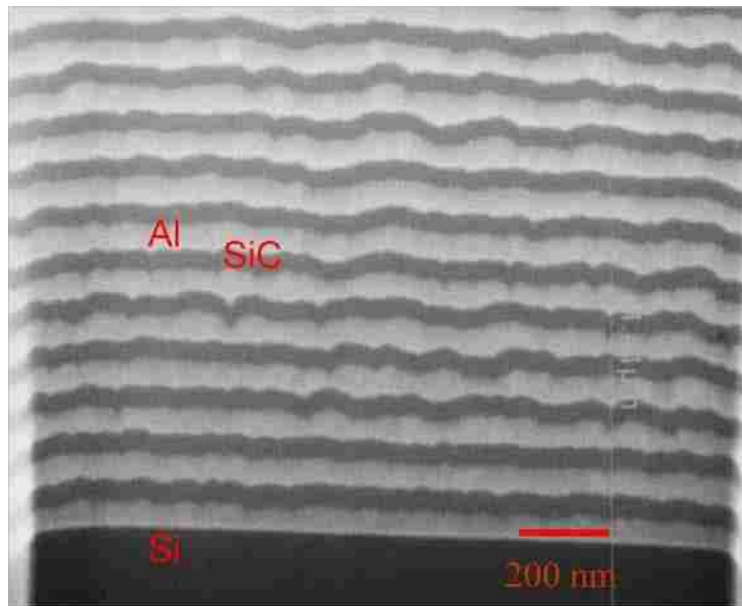
In this dissertation, the focus is on the mechanical properties of metal-ceramic nanocomposites. We utilized aluminum (Al)/silicon carbide (SiC) nanolaminates as a model system. The geometric layout is sufficiently simple so a systematic investigation can be attempted. On the practical side, micro or nanolayered metal-metal and metal-ceramic composites can possess high strength, high toughness and high damage tolerance so they may be further developed for a wide variety of structural applications.

Traditional mechanical testing methods for bulk materials are not easily used on small-scale structures. The indentation technique has become the most popular approach to characterize their mechanical properties. The microcompression test on specially fabricated specimens such as a pillar, which was developed only in the past several years, is another appealing technique.

In this work, numerical models were constructed and extensive simulations were carried out. We aim at correlating the modeling analyses with the experiments carried out by our collaborators at Arizona State University. Figure 1.1 (a) and (b) show two representative cross-sectioned images of the Al/SiC multilayer structure. The nanolaminated composites were fabricated by magnetron sputtering of Al and SiC thin films, which resulted in polycrystalline Al layers with a columnar grain structure and amorphous SiC layers, on a silicon (Si) substrate. All the analyses reported in this dissertation are centered around this nanocomposite system.



(a)



(b)

Figure 1.1: Scanning electron micrographs of Al/SiC multilayers cross-sectioned by Focused Ion Beam (FIB): (a) 7-layer Al₁₅₀SiC₅₀ and (b) 41 layer Al₁₅₀SiC₅₀, Courtesy of N. Chawla and D. R. P. Singh

Chapter 2 Literature review

Synthetic and natural composite laminates have been shown to exhibit a combination of excellent strength and toughness [1]. Composite laminates on the nano-scale with unique properties have been developed. These composites have been investigated in many different layered combinations: Metal-metal composites [2-8], metal-ceramic composites [9-15], and ceramic-ceramic composites [16-18]. Metal-ceramic nanolaminate systems can exhibit a combination of high strength, high toughness, damage tolerance, as well as their potential applications in functional devices [12, 13, 19-36].

Because these composites have a feature size at the nano-scale, characterization of their mechanical response has been relying on nanoindentation. Nanoindentation is an indentation test in which the indenting depth is at the scale of nanometers to micrometers.

Nanoindentation is also called instrumented indentation and depth-sensing indentation. It is a relatively new technology, which has been developed in the past three decades. An indentation test requires minimal material preparation, and can be performed multiple times on a single specimen. The choice of applied load and indenter tip geometry enables the probing of different volumes and shapes of materials. Many important topics about nanoindentation are covered in the book “Nanoindentation” [37], which includes most popular methods of nanoindentation tests, the theory behind the extraction of elastic modulus and hardness from the load-displacement data, and the methods of operation of the present commercial instruments. Also in an article “Instrumented indentation testing” [38], a very thorough introduction on nanoindentation was presented.

Figure 2.1 shows the schematic of a nanoindenter. Nanoindentation tests are controlled through computers. The distance the indenter travels is in the range of several nanometers to several micrometers. The forces are within several millinewtons. The system is sensitive to mechanical vibration and thermal drift. A specimen is required to have a very smooth and flat surface. In a test cycle of nanoindentation, loading and unloading process could be continuous. The distances and forces are constantly recorded throughout the test cycle. The load could also be applied through many small increments and each increment is followed by an unloading increment, which gives the contact stiffness at that particular load, which is called the continuous stiffness measurement (CSM) method. These recorded data are later used to determine hardness and elastic modulus.

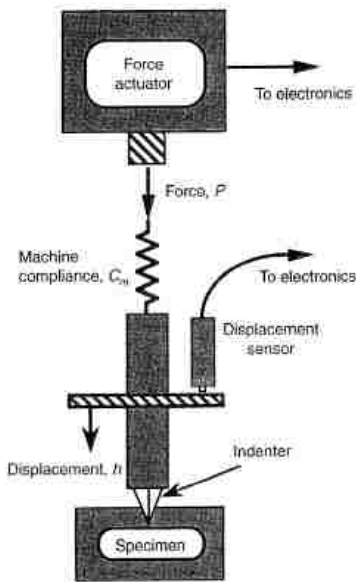


Figure 2.1: Schematic of a nanoindenter [38].

Figure 2.2 shows the schematic of different shapes of indenter tips. The Vickers indenter, Berkovich indenter and Knoop indenter are all pyramidal indenters, which have a normally sharp tip and could be used on small scale samples. Conical indenters also have a sharp tip, but it is hard to manufacture a true sharp tip for conical indenters in real life. The Rockwell indenter is a conical indenter with a round tip. Spherical indenters are usually made of hardened steel or tungsten carbide.

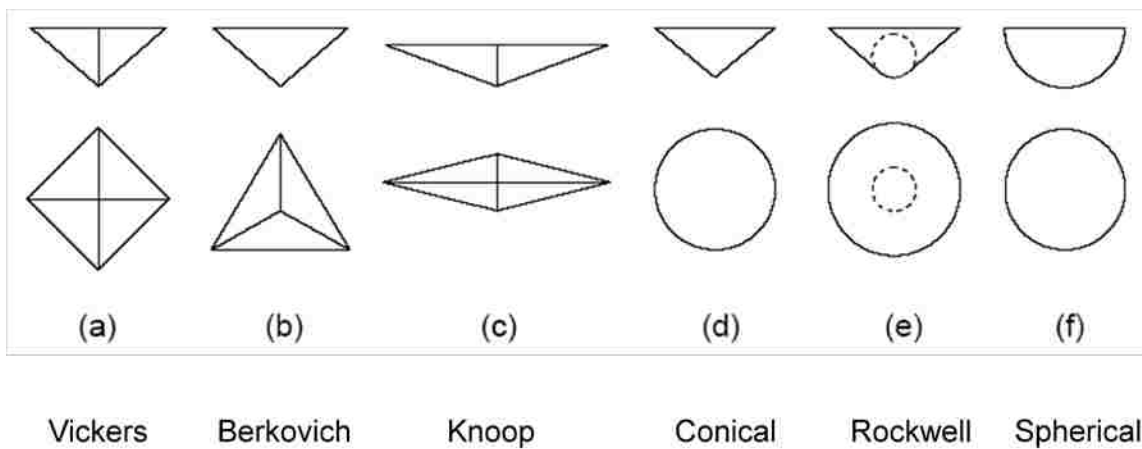


Figure 2.2: Schematics of indenter with different tips.

A Berkovich indenter is a three faced pyramid indenter, which is generally used in small-scale indentation tests. It normally has a face angle (angle between face and central axis) of 65.3° . Figure 2.3 shows a schematic of the Berkovich indenter. A very hard material, like diamond, is usually chosen to make the indenter.

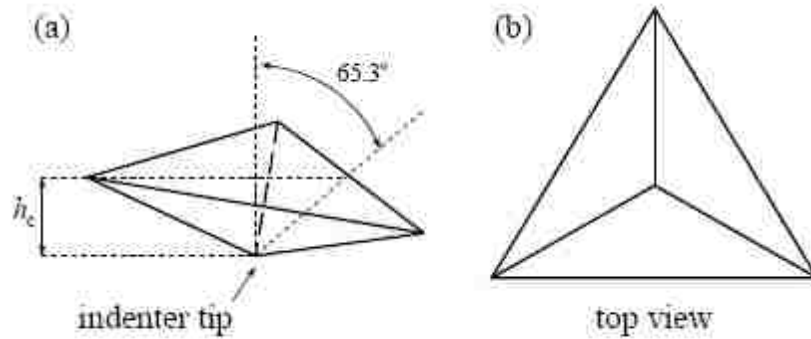


Figure 2.3: Schematic of the Berkovich indenter (a) Indenter impression tip with the face angle of 65.3° and the contact depth of h_c . (b) Top view of the impression area [90].

In conventional indentation tests, the contact area between the indenter and the specimen is directly measured from the residual impression left on the specimen. It is difficult to measure the area of the impression when the length scale is very small. For nanoindentation tests, the area is calculated through the depth the indenter penetrates into the specimen (h_c) and with known geometry of the indenter. Figure 2.4 shows the schematic of contact between a specimen and a conical indenter during an indentation test. Here h is the total displacement; h_c is the penetration depth; h_f is the final displacement after unloading; a is the radius of the contact area at the penetration depth of h_c . The method for obtaining elastic modulus and hardness of the test material will be given in Chapter 3.

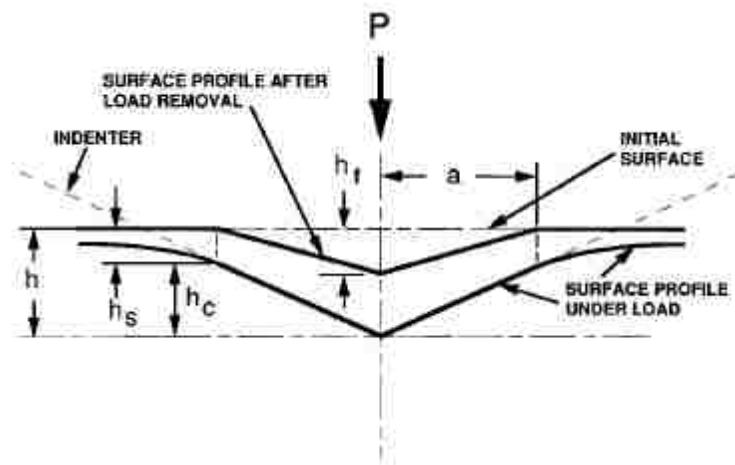


Figure 2.4: Schematic of contact between a specimen and a conical indenter during an indentation test [39].

Existing theories for extracting material properties from indentation response are based on the assumption that the material being indented is a homogeneous body with a unique set of properties [37, 39-45]. There have been a large number of works focusing on the finite element modeling of nanoindentation [e.g. 46-50]. However, many materials like nanolaminates contain microstructural constituents with distinctly different mechanical properties. How this heterogeneity will affect the measurement of effective material properties using indentation is still poorly understood [41]. A continuum-based numerical study focusing on the effective hardness of multilayers has been reported [51]. Under the ideal elastic-perfectly plastic assumption, it was shown that the indentation hardness, upon conversion to plastic flow stress, underestimates the overall strength of the composite. The stress state under the indenter in monolithic materials is inherently complex. This stress state is even more complex in metal-ceramic nanolaminates because of the intrinsic heterogeneity

introduced by alternating hard and soft layers. Most of these composites are made by deposition of thin films on a substrate, such as Si, which can also affect the indentation response [52]. Furthermore, internal damages may take place during the indentation process. The precise nature and evolution of damage in these composites are not well understood. Therefore, the present work to study and characterize the multilayered material becomes very important for gaining a fundamental understanding of the indentation behavior of the layered composite.

In the past several years, a new technique of microcompression on free standing pillar-shaped materials was developed to investigate the mechanical behavior at the micro- and nano-scale [53-64]. The pillar samples with the size of a few hundred nanometers to several micrometers are prepared by focused ion beam (FIB) milling. The compression tests are conducted using a modified nanoindentation device with a flat-punch indenter tip. The flat-punch indenter is usually produced by truncating the tip of a Berkovich indenter. The pillar is always attached to a base material (the original substrate). Some researchers have proposed new techniques such as directionally solidification [65], and photolithography [66, 67] to produce the pillar sample. In order to avoid the buckling which usually happens when compressing on a thin and long pillar, a technique of tensile tests rather than compression on the pillar sample has also been developed [68]. In most of the cases, the samples are cylindrical, although other type of pillar like a square cross section [69, 70], does exist.

In most of the studies, the sample is a single crystal and the purpose is to study the size

effects on elastic and plastic properties of the material [71]. Some finite element simulations were carried out to investigate the sample geometry and deformations during microcompression tests [72, 73]. There has not been work about microcompression tests on a multilayered pillar reported in the literature. In this dissertation, we perform numerical simulation on multilayer composite pillars and compare the numerical results with the experimental observations.

Chapter 3 **Background Study: Homogeneous Materials and Simple Film-Substrate Systems**

In this chapter, several simple models are utilized for the indentation simulation. We focus on the following issues: obtaining effective elastic modulus and hardness through indentation, the substrate effects on elastic modulus and hardness, and the role of plastic properties in calculating indentation-derived elastic modulus.

3.1 Model

Two model systems are considered for indentation. One is a homogeneous material (pure Al); the other is a single film on a Si substrate. Figure 3.1 (a) and (b) show a piece of homogeneous block and a single film on substrate, respectively. Several thin film materials are studied: Al films with various yield strengths and SiC film.

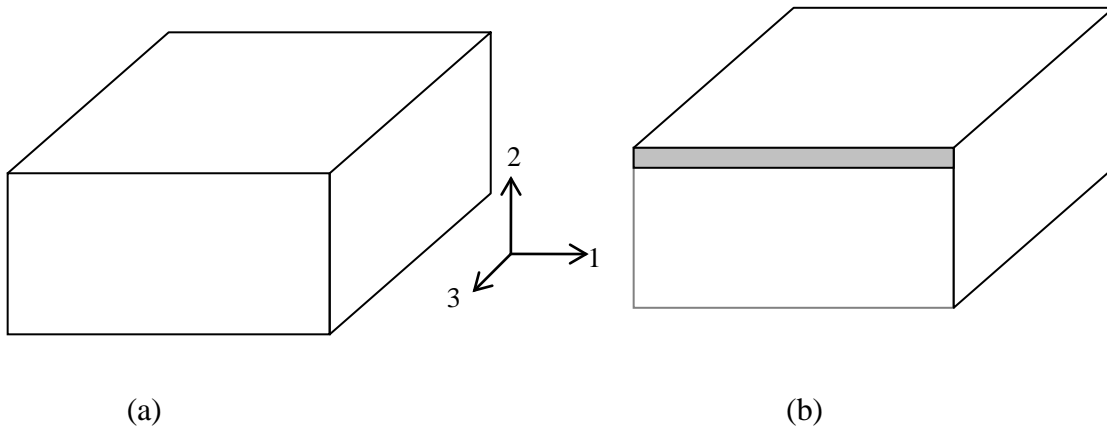


Figure 3.1: (a) Schematic showing a homogeneous block. (b) Schematic showing a single film on substrate.

3.2 Indentation modeling

Simulations of indentation were based on an axisymmetric model featuring a rigid conical indenter. Figure 3.2 (a) and (b) shows the schematic of the model of indentation onto the specimen. The left boundary is treated as the symmetry axis. The semi-angle of the conical indenter is 70.3° , resulting in a same projected area as that of a Berkovich indenter [37].

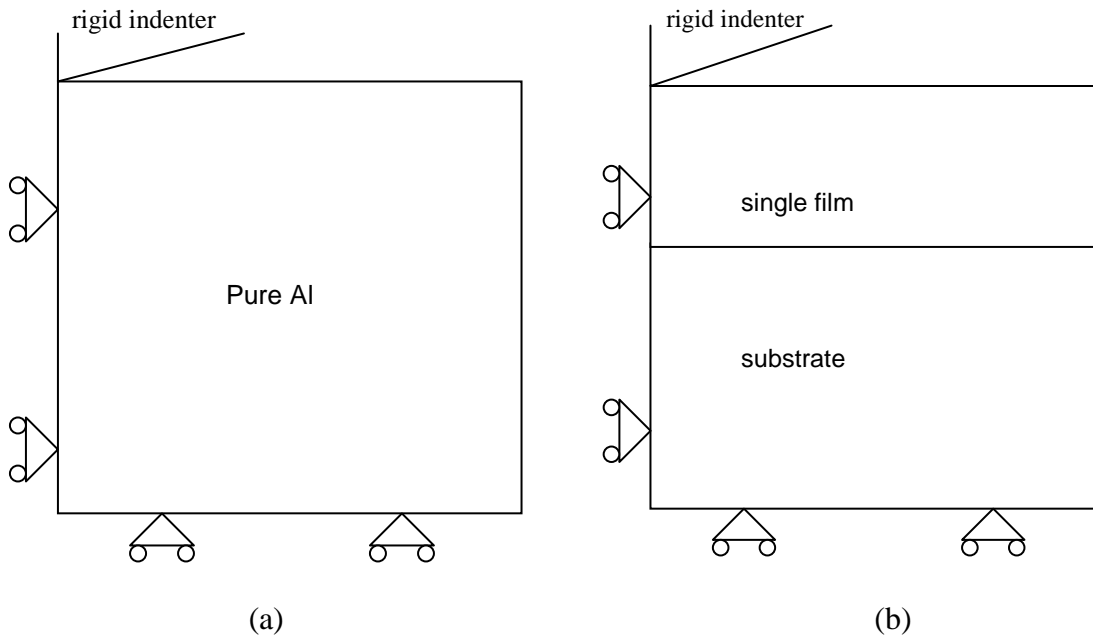


Figure 3.2: (a) Schematic showing the specimen of pure Al and the boundary conditions for indentation modeling. The specimen and indenter both possess axial symmetry about the left boundary. The rigid indenter has a semi-angle of 70.3° . (b) Schematic showing the specimen of a single film on Si substrate with all other conditions the same as in (a).

Although there is no intrinsic length scale in the analysis, it is convenient to associate the model with specific physical dimensions. The overall size of the entire specimen is taken as

40 μm in lateral span (radius) and 43 μm in height. During deformation the left boundary is allowed to move only in the 2-direction. The bottom boundary is allowed to move only in the 1-direction. The right boundary is not constrained. The top boundary is also free to move, except when contact with the indenter is established, the surface portion engaged by the indenter is restricted to follow the indenter contour. The coefficient of friction at the contact is taken to be 0.1, which is a typical value for the diamond/metal contact pair [74, 75].

The indentation-derived elastic modulus from the simulation is obtained according to the method proposed by Oliver and Pharr [39]. The method is based on the expression:

$$S = \beta \frac{2}{\sqrt{\pi}} E_r \sqrt{A} \quad (3.1)$$

where S is contact stiffness obtained from the initial unloading slope of an indentation load-displacement curve, A is the projected contact area at the onset of unloading, β is an indenter geometry-dependent dimensionless parameter close to unity, and E_r is the reduced modulus given by

$$\frac{1}{E_r} = \frac{1 - \nu^2}{E} + \frac{1 - \nu_i^2}{E_i}. \quad (3.2)$$

In Equation (3.2) E and ν are the Young's modulus and Poisson's ratio, respectively, of the material being tested, and E_i and ν_i are the Young's modulus and Poisson's ratio, respectively, of the indenter. The term containing E_i and ν_i in Equation (3.2) was not used in the present analysis (Chapter 3 and Chapter 4) because a rigid indenter is employed here. It will be used in the following chapters where the indenter is elastic. When calculating the

contact stiffness S , the data from top 50% of the curve is used to fit a quadratic equation (for conical indenter [39]) and then to obtain the slope at the initial point of the curve. When calculating the projected contact area A , the last nodal point on the top surface in contact with the indenter was identified in the deformed finite element mesh so the effect of pileup resulting from the indentation was taken into account.

The indentation-derived hardness from the simulation is obtained from the following expression:

$$H = \frac{P}{A} \quad (3.3)$$

where H is the hardness, P is the applied load (reaction force); and A is the projected contact area at the given load P .

The finite element program ABAQUS (Version 6.5, Dassault Systemes Simulia Corp., Providence, RI) was employed in the calculations. A total of 174267 linear elements were used in the model, with a finer mesh size near the upper-left corner. Figure 3.3 (a) shows the overall mesh of the whole model. Figure 3.3 (b) shows a zoomed in image of the upper left corner of the specimen. Most of the elements are four-node rectangular elements. Three-node triangular elements are included for smooth transitioning of element size.

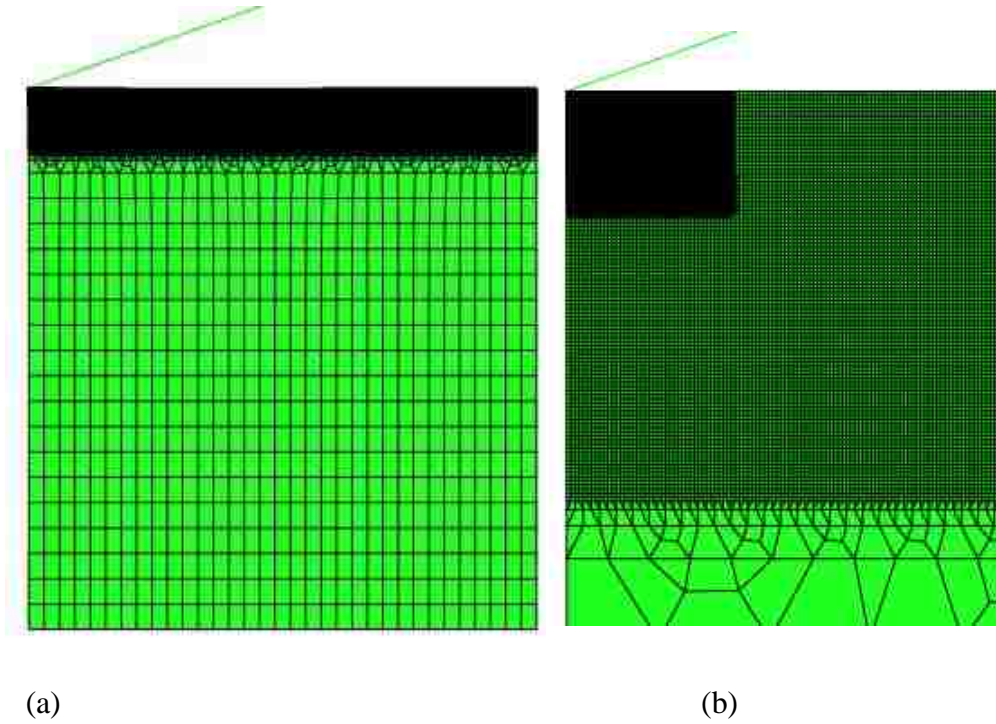


Figure 3.3: (a) A representative mesh of a single Al film on Si substrate. (b) Detailed mesh at the upper left corner of the model in (a).

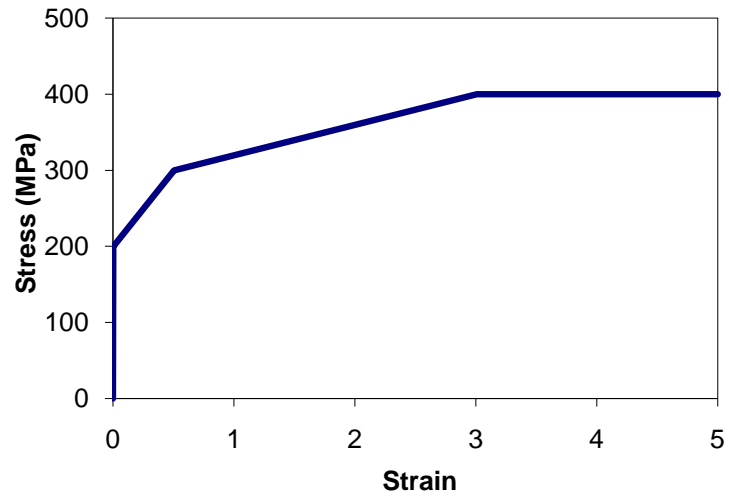
3.3 Numerical results

a) Material properties

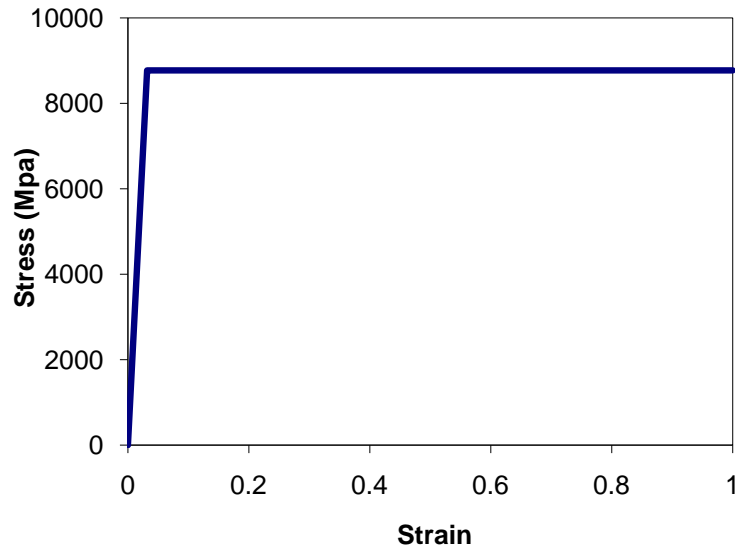
In the finite element modeling, the material properties of Al, SiC, Si and diamond are needed.

The Young's modulus E and Poisson's ratio ν , used as input parameters, were: $E_{Al} = 59$ GPa, $\nu_{Al} = 0.33$, $E_{SiC} = 277$ GPa, $\nu_{SiC} = 0.17$, $E_{Si} = 187$ GPa, $\nu_{Si} = 0.28$, $E_{Dia} = 1141$ GPa and $\nu_{Dia} = 0.07$. The input plastic response of Al, based on the tensile loading data of single-layer Al [30], is illustrated in Figure 3.4 (a) with initial yield strength of 200 MPa. The yield strength of SiC used in the modeling, 8770 MPa, was estimated from the indentation hardness of a single-layer SiC film (from experiment the SiC layers were amorphous and displayed a

plastic-type response [30]) and is shown in Figure 3.4 (b).



(a)



(b)

Figure 3.4: (a) Stress-strain response of Al (b) Stress-strain response of SiC, used as input in the finite element modeling.

b) Calibration of β factor

The indentation model is shown in Figure 3.2 (a). The specimen is pure aluminum with a thickness of 43 μm . Figure 3.5 shows a representative indentation load-displacement curve with a maximum indentation depth at 700 nm. The initial slope during unloading was used to calculate the indentation-derived elastic modulus of the material. As in Equation (3.1), the indentation-derived modulus is related with β , which is an indenter geometry-dependent dimensionless parameter close to unity. To determine the elastic modulus from our simulation, the parameter β needs to be calibrated first. Figure 3.6 shows the numerical results of the indentation-derived elastic modulus as a function of indentation depth. The maximum indentation depth considered is 700 nm. It shows a constant modulus value over the range of indentation depth. We need to adjust the β value to be able to recover a modulus of 59 GPa for Al. The value is found to be 1.06 and it will be used for all models with the same geometry and the same rigid indenter. Similarly we found β to be 1.04 for the model with the same geometry but with a diamond indenter to be used in the later chapters.

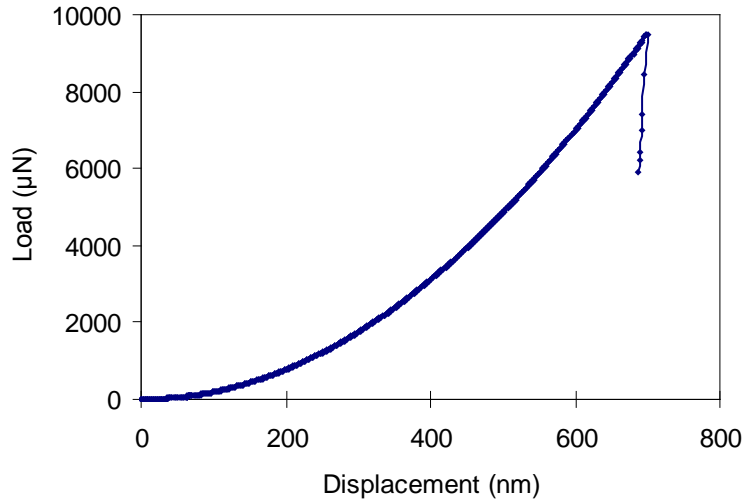


Figure 3.5: A representative indentation load-displacement response obtained from the finite element modeling. This curve corresponds to the homogeneous model of pure Al, with the maximum indentation depth at 700 nm.

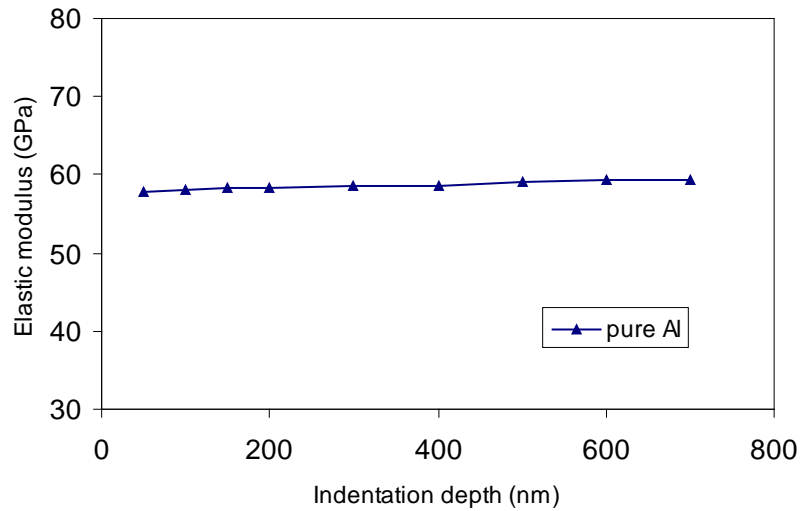


Figure 3.6: Numerical result showing the indentation derived Young's modulus of Al as a function of the indentation depth with $\beta = 1.06$ for the rigid indenter.

c) Substrate effects

The model is shown in Figure 3.2 (b). The upper portion is an Al film of 5 μm thickness while the bottom portion is a Si substrate of 38 μm thickness. Figure 3.7 shows the numerical results of the indentation-derived elastic modulus as a function of indentation depth. The maximum indentation depth shown is 1.5 μm . It does not show a constant modulus value over the range of indentation depth considered. Elastic modulus keeps increasing as the indentation goes deeper. This is due to the substrate effect which apparently exists throughout the indentation range. Note that the first indentation point shown in Figure 3.7 is only at 2% of the film thickness.

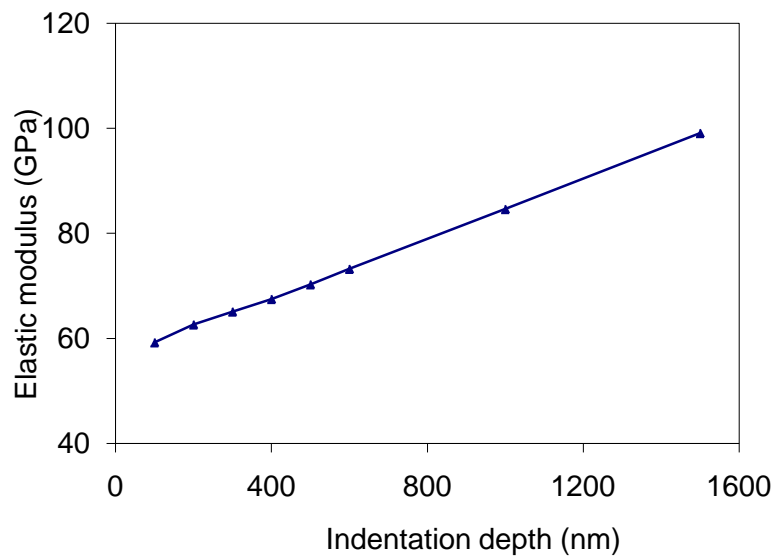


Figure 3.7: Indentation-derived elastic modulus as a function of the indentation depth for Al on Si.

Figure 3.8 shows the numerical results of the indentation-derived hardness as a function of indentation depth. The maximum indentation depth shown is 1.5 μm . It shows a near constant hardness value over the whole indentation range. The results in Figure 3.8 illustrated that, for hardness measurement, a fairly constant value can be obtained even if the indentation is relatively deep (up to 30% of the film thickness in Figure 3.8). As for the elastic modulus, the substrate effect is already significant even when the indentation is at a few percentage of the film thickness.

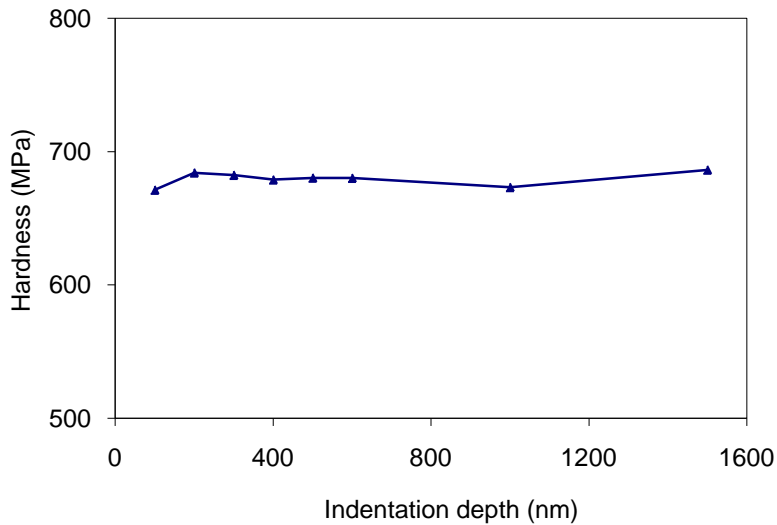


Figure 3.8: Indentation-derived hardness as a function of the indentation depth for Al on Si.

d) Effects of plastic properties of Al

The model has the same geometry as the one in section (c). The upper portion is an Al film of 5 μm while the bottom portion is a Si substrate of 38 μm . Three systems with different initial yield strength of Al are considered: 200 MPa, 1200 MPa and 2200 MPa. Figure 3.9 shows the numerical results of the indentation-derived elastic modulus as a function of indentation depth. The maximum indentation depth shown is 500 nm. The modulus values of Al with different yield strength are very close to one another. Therefore, under the current model configuration, the indentation-derived elastic modulus is essentially independent of the input plastic behavior in the finite element model. This is also consistent with other theoretical and/or numerical studies [42, 76]. In the remainder of this chapter and Chapter 4 where indentation derived elastic modulus of the Al/SiC multilayer composites are considered, the yield strength of SiC will be set to be the same as that of Al, to avoid indenting extremely hard layers for improving computational efficiency. In later chapters the “hard” SiC properties will be included in the model.

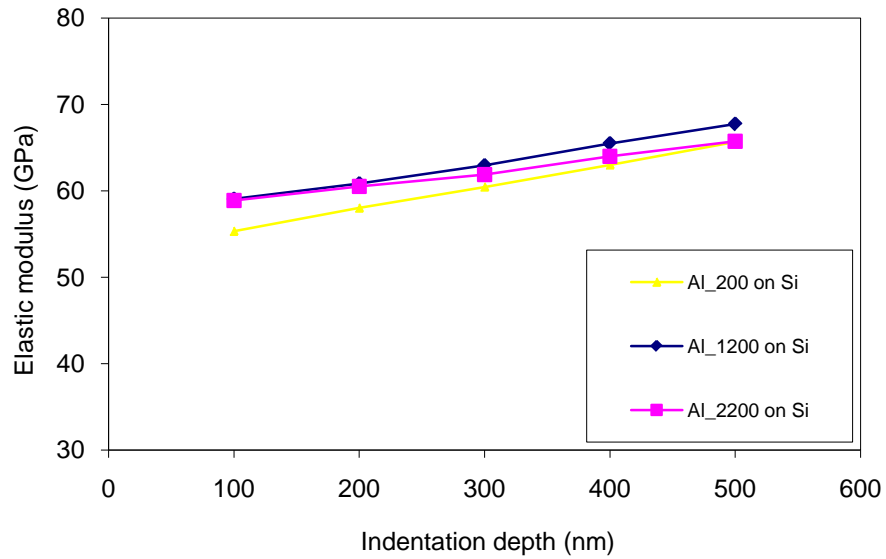


Figure 3.9: Indentation-derived elastic modulus as a function of the indentation depth for Al with different yield strength on Si.

e) SiC film on Si substrate

The model has the same geometry as the one in section (c). The upper portion is a SiC film of 5 μm while the bottom portion is a Si substrate of 38 μm . Figure 3.10 shows the numerical results of the indentation-derived elastic modulus as a function of indentation depth. The maximum indentation depth shown is 1 μm . It does not show a constant modulus value over the range of indentation depth considered. Elastic modulus keeps decreasing as the indentation goes deeper due to the substrate effect.

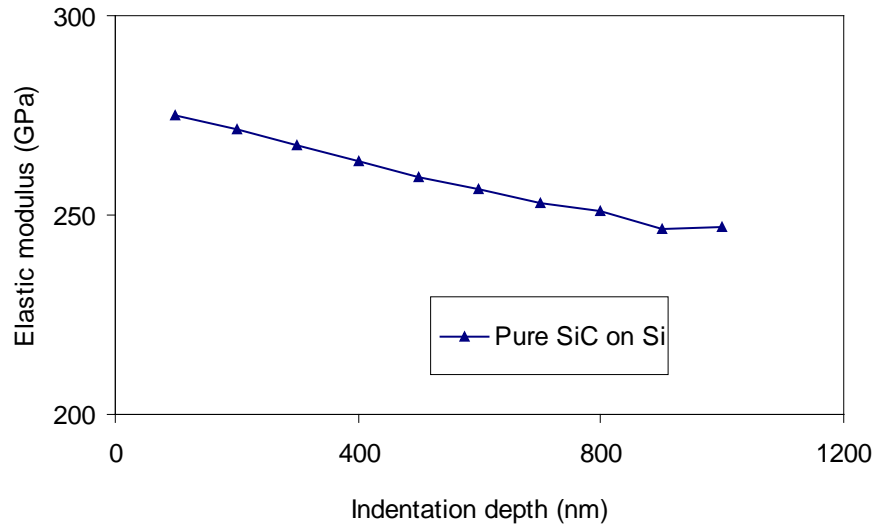
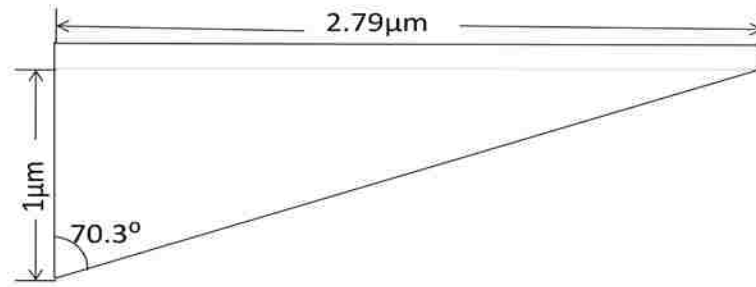


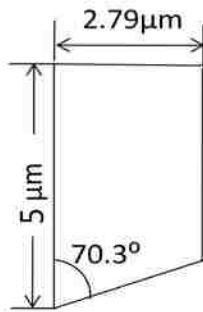
Figure 3.10: Indentation-derived elastic modulus as a function of the indentation depth for SiC on Si.

f) Indenter size effects

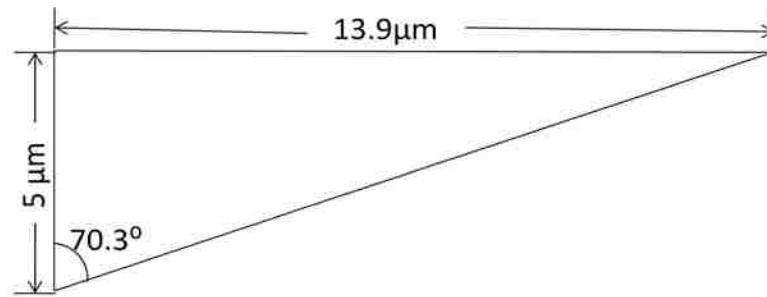
In this section, we investigate the effects of the size and shape of the indenter used in the finite element analysis. This is an important preliminary issue in all indentation modeling efforts, although to our knowledge, there has never been a systematic study reported. We construct three models with different elastic indenters and one model with a rigid indenter. The material being indented is a homogeneous Al body. Elastic indenter I (Figure 3.11 (a)) has a height of 1 μm ; elastic indenter II (Figure 3.11 (b)) has a height of 5 μm and it is tall and thin; elastic indenter III (Figure 3.11 (c)) has a height of 5 μm and it has a triangle shape. All the elastic indenters and the rigid indenter have a semi-angle of 70.3° .



(a)



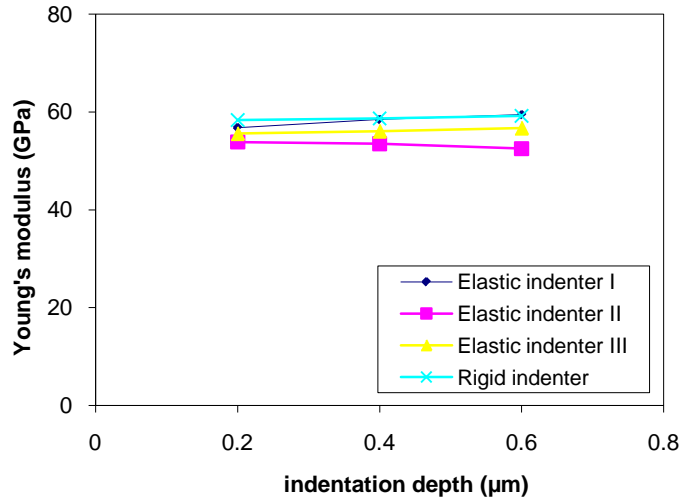
(b)



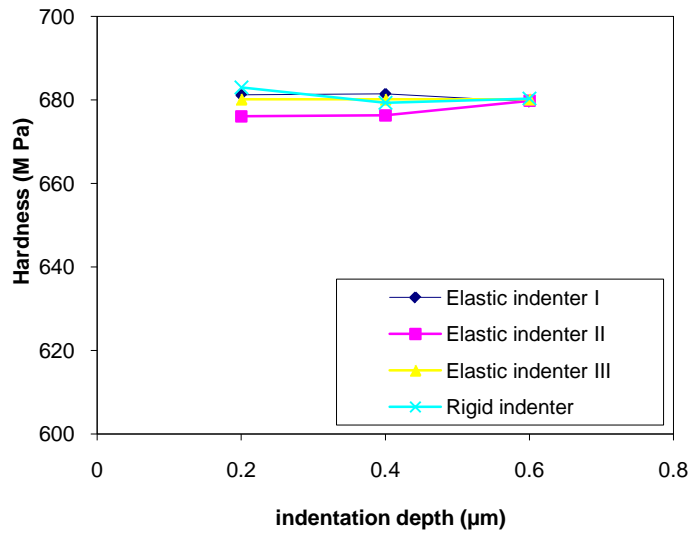
(c)

Figure 3.11: Schematic of the elastic indenters.

The elastic moduli and hardness resulting of the four models with different indenters are plotted in Figure 3.12 (a) and (b). The modulus values of the three models with elastic indenter were a little lower than, but still quite close to, the value of the model with rigid indenter. In general, the modulus value decreases with an increasing indenter size. For hardness values, there is no significant difference among the four models.



(a)



(b)

Figure 3.12: (a) Elastic modulus as a function of the indentation depth for different indenters (b) Hardness as a function of the indentation depth for different indenters.

3.4 Conclusions

The geometry-dependent dimensionless parameter β used in the calculation of indentation-derived modulus is calibrated to be 1.06 for rigid indenter model and 1.04 for elastic indenter model. For a model system of a single film on substrate, the substrate does make an impact on elastic modulus, but not as much on hardness. For elastic modulus the substrate effect exists even at very shallow indentation. The hardness value is not affected by the substrate within the range of indentation depth considered. For a single Al film with different yield strengths, the indentation-derived modulus values were found to be very close to one another. Therefore, under the current model configuration, the elastic modulus is essentially independent of the input plastic behavior in the finite element model. For models with different indenter sizes, the indentation-derived modulus value decreases with an increasing indenter size and the hardness is essentially not affected.

Chapter 4 Effective Elastic Response of “Infinite” Layers

In this chapter, we focus on the effective elastic modulus of the metal-ceramic multilayers obtained from indentation. Our model system consists of alternating layers of Al and SiC. The true effective elastic response of the composite was represented by a homogeneous anisotropic material. The elastic constants of the composite were obtained by a combination of analytical and numerical means under uniaxial compression loading. Finite element modeling of indentation into the homogeneous material was then employed to calculate the indentation-derived modulus. The indentation-derived modulus and the “true” composite modulus were compared. In addition, finite element modeling of indentation was conducted with the multilayers modeled explicitly. The primary objectives of this analysis are (i) to determine if the true elastic response of the multilayers can be extracted from instrumented indentation, and (ii) to see how the indentation-derived modulus compares with the actual anisotropic elastic properties of the composite. Results presented in this chapter have been published in [77].

4.1 Overall elastic properties

Figure 4.1 shows a schematic of the multilayer structure which is composed of a large number of alternating metal and ceramic layers. The individual layers are isotropic, each with an in-plane dimension (along the 1- and 3-directions) much greater than the out-of-plane dimension (the 2-direction). All interfaces between adjacent layers are assumed to be perfectly bonded so the displacement field across the interface is continuous. Although the

individual layer thickness may be conceived to be in the micrometer or nanometer range, there is no intrinsic length scale involved in the present scheme.

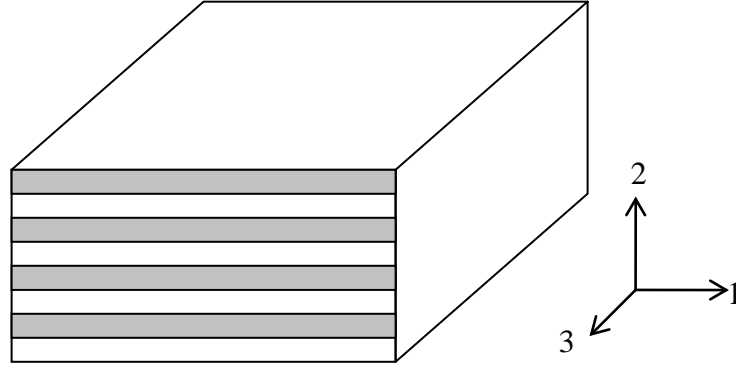


Figure 4.1: Schematic showing the alternating metal-ceramic layers considered in this study.

If the composite in Figure 4.1 is treated as a homogeneous material, its anisotropic elastic properties can be represented by a set of elastic constants. It is convenient to start with the generalized Hooke's law for an *orthotropic* material system:

$$\begin{bmatrix} \varepsilon_{11} \\ \varepsilon_{22} \\ \varepsilon_{33} \\ \gamma_{12} \\ \gamma_{13} \\ \gamma_{23} \end{bmatrix} = \begin{bmatrix} 1/E_{11} & -\nu_{21}/E_{22} & -\nu_{31}/E_{33} & 0 & 0 & 0 \\ -\nu_{12}/E_{11} & 1/E_{22} & -\nu_{32}/E_{33} & 0 & 0 & 0 \\ -\nu_{13}/E_{11} & -\nu_{23}/E_{22} & 1/E_{33} & 0 & 0 & 0 \\ 0 & 0 & 0 & 1/G_{12} & 0 & 0 \\ 0 & 0 & 0 & 0 & 1/G_{13} & 0 \\ 0 & 0 & 0 & 0 & 0 & 1/G_{23} \end{bmatrix} \begin{bmatrix} \sigma_{11} \\ \sigma_{22} \\ \sigma_{33} \\ \sigma_{12} \\ \sigma_{13} \\ \sigma_{23} \end{bmatrix}, \quad (4.1)$$

where ε , γ , σ , E , G and ν represent the normal strain, shear strain, stress, Young's modulus, shear modulus and Poisson's ratio, respectively. The coordinate axes are based on those defined in Figure 4. 1. For an orthotropic material the following relations hold true [78]:

$$\frac{\nu_{12}}{E_{11}} = \frac{\nu_{21}}{E_{22}}, \quad \frac{\nu_{13}}{E_{11}} = \frac{\nu_{31}}{E_{33}}, \quad \frac{\nu_{23}}{E_{22}} = \frac{\nu_{32}}{E_{33}}. \quad (4.2)$$

Therefore there are a total of 9 independent elastic constants (which may be taken as E_{11} , E_{22} , E_{33} , ν_{12} , ν_{13} , ν_{23} , G_{12} , G_{13} and G_{23}). The multilayered structure considered here is a special case of the orthotropic material: It is *transversely isotropic* along the 13-plane. As a consequence,

$$E_{11} = E_{33}, \quad G_{12} = G_{23}, \quad \nu_{21} = \nu_{23}, \quad \nu_{12} = \nu_{32}, \quad \nu_{13} = \nu_{31}, \quad G_{13} = \frac{E_{11}}{2(1 + \nu_{13})}. \quad (4.3)$$

There are now only 5 independent elastic constants, which may be chosen as E_{11} , E_{22} , ν_{12} , ν_{13} and G_{12} . These 5 constants are determined following the approach outlined below.

A simple way to compute the magnitudes of E_{11} and E_{22} of the composite, is to use the relations based on the isostrain condition (Voigt model) and isostress condition (Reuss model), respectively. The composite modulus E_c in the isostrain condition (E_{11}) is:

$$E_c = E_{Al} f_{Al} + E_{SiC} f_{SiC}, \quad (4.4)$$

while in the isostress case (E_{22}),

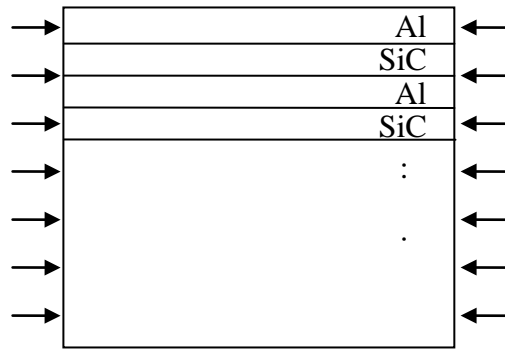
$$E_c = \frac{1}{\frac{f_{Al}}{E_{Al}} + \frac{f_{SiC}}{E_{SiC}}}. \quad (4.5)$$

Here f represents the volume fraction of the constituents denoted by the subscripts. It should

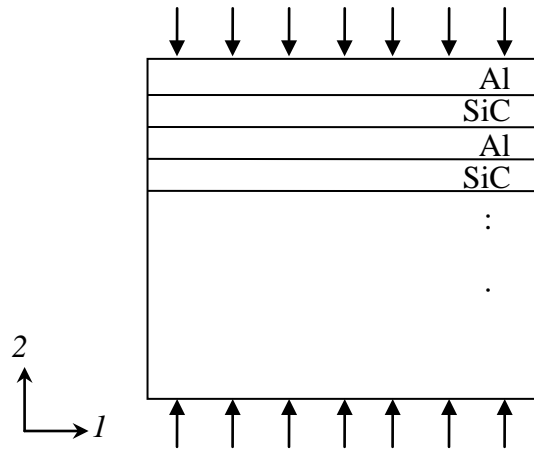
be noted that Equations (4.4) and (4.5) are derived under a one-dimensional assumption so care must be taken in directly applying them to the material considered here. For instance, when the layered composite is subject to loading along the 1-direction, uneven deformation in the 3-direction between layers will occur due to the different Poisson's ratios of Al and SiC. This will generate stresses in the 3-direction and, in turn, will affect the stresses in the 1-direction and thus the longitudinal composite modulus, E_{11} . Similarly, when the loading is along the 2-direction, the strains along the same direction in the two materials will not be the same. Unequal lateral deformations between the layers will occur, which will in turn affect stresses in the 2-direction, and thus, the transverse composite modulus, E_{22} . Thus, depending on the magnitude of the elastic constants, significant errors may exist if one uses these one-dimensional approximations (Equations (4.4) and (4.5)). As a consequence, in the present study we use finite element modeling of overall uniaxial loading of the multilayers to accurately determine the necessary elastic constants, as described below.

Figure 4.2 shows a schematic of compressive loading of the multilayered structure. The composite Young's moduli were calculated from the ratio of stress and strain along the direction of interest, and the composite Poisson's ratios were calculated from the respective strain ratios. In the actual numerical model only two representative layers were included with appropriate boundary conditions imposed such that a periodic stacking along the transverse (out-of-plane) direction and an infinite dimension in the longitudinal (in-plane) direction were ensured. This was accomplished by setting the top and bottom boundaries to remain horizontal and the side boundaries to remain vertical during deformation, similar to the

unit-cell approach for simulating particle-matrix composite systems [79, 80]. The calculated composite response is the “true” effective property of the entire multilayer structure with all three-dimensional features accounted for. The longitudinal loading configuration in Figure 4.2 (a) was used for obtaining E_{11} , ν_{12} and ν_{13} , and the transverse loading configuration in Figure 4.2 (b) was used for obtaining E_{22} .



(a)



(b)

Figure 4.2: Schematics showing the (a) longitudinal and (b) transverse loading configurations for modeling the overall elastic response of the multilayered composite.

The remaining elastic constant to be determined is G_{12} . It can be directly obtained from the analytical expression

$$G_{12} = \left[\frac{f_{Al}}{G_{Al}} + \frac{f_{SiC}}{G_{SiC}} \right]^{-1}, \quad (4.6)$$

which is based on the equivalent shear stress condition [81]. The five independent elastic constants are then used as input parameters for simulating indentation of the “homogenized” Al/SiC composite.

4.2 Indentation modeling

Simulations of indentation were based on an axisymmetric model featuring a rigid conical indenter as used in Chapter 3. Two models of the same geometry were considered: one with the Al and SiC layers explicitly accounted for and the other a homogeneous block possessing the anisotropic elastic property of the Al/SiC composite. They are henceforth referred to as the “multilayer model” and “homogenized model,” respectively. Note that the two models have exactly the same *overall* elastic behavior. Figure 4.3 shows the schematic of the model of indentation into the multilayer. In the upper portion of the model there are a total of 100 alternating layers of Al and SiC. Although this model is intended to represent the real composite with an “infinite” number of layers, a homogenized Al/SiC material having the anisotropic composite property is placed underneath the 100 explicit layers. The main purpose of this is to improve computational efficiency by allowing a coarser mesh size in the less deformed lower region. Very small elements have to be employed within the layered region to sufficiently resolve the geometry-limited deformation field.

The overall size of the entire specimen is the same as the model used in Chapter 3, which is 40 μm in lateral span (radius) and 43 μm in height. The region containing 100 layers of Al and SiC has a total thickness of 5 μm . In the case of the homogenized model, both the Al and SiC layers in Figure 4.3 were simply replaced by the homogenized Al/SiC composite. The boundary conditions are the same as those in Chapter 3. The input elastic properties of Al and SiC were given in Chapter 3. The input plastic response of SiC used in this chapter is set to be the same as that of Al to improve computational efficiency. A total of 173,105 linear elements were used in the model, with a finer mesh size near the upper-left corner. In the simulation the maximum indentation depth considered is within 2% of the total height and radius of the specimen, so the edge effect due to the side and bottom boundaries was negligible (according to our preliminary calculations).

In this work the calculation of the overall anisotropic elastic property for the homogenized model incorporates the entire span of Al/SiC volume (thickness) ratio from zero to one. Three specific Al/SiC volume ratios were selected for the indentation modeling: Al150/SiC50, Al25/SiC75 and Al75/SiC25 (here the numbers represent the thickness of the individual layer, in nm). Equations (3.1) and (3.2) are used to calculate elastic modulus with a β value of 1.06. The calculation of indentation-derived modulus (Equation (3.2)) E from E_r requires a known Poisson's ratio of the composite. Here we used the ν_{23} value obtained from the modeling of overall uniaxial loading of the Al/SiC composite, as described above.

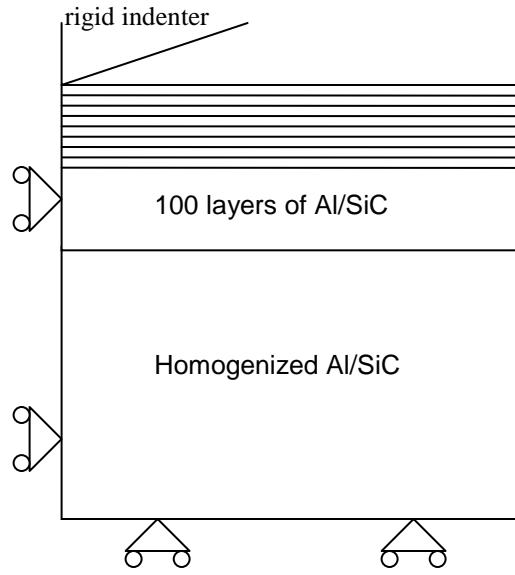


Figure 4.3: Schematic showing the multilayer model and the boundary conditions for indentation modeling. The specimen and indenter both possess axial symmetry about the left boundary. The rigid indenter has a semi-angle of 70.3°.

4.3 Numerical results

a) Overall elastic properties

We first present the overall elastic properties of the Al/SiC multilayer composite, on the basis of the approach described in Section 4.1. Figure 4.4 shows the numerically modeled Young's modulus values as a function of volume fraction of SiC. For comparison purposes the modulus values given by the one-dimensional approximation Equations (4.4) and (4.5) are also included in the figure. It can be seen that the difference between the longitudinal modulus (E_{11}) and transverse modulus (E_{22}) of the Al/SiC multilayers is quite large.

In general the numerically modeled E_{11} values are close to those given by Equation (4.4), but there is a significant discrepancy between the numerical E_{22} values and those from Equation (4.5). The inaccuracy of applying the one-dimensional approximation to composite modulus of the metal/ceramic multilayers is thus illustrated.

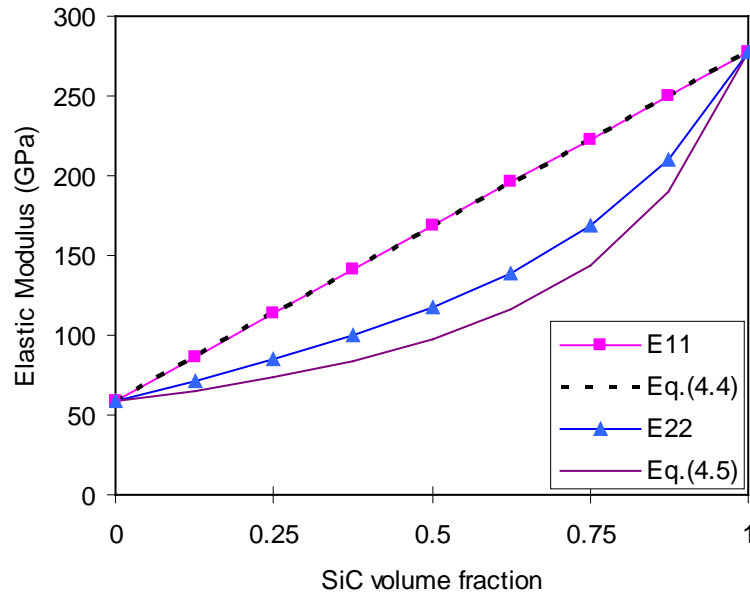


Figure 4.4: Numerical result showing the overall Young’s modulus along the longitudinal direction (E_{11}) and transverse direction (E_{22}) of the Al/SiC multilayers. For comparison the modulus values based on the one-dimensional assumption (Equations (4.4) and (4.5)) are also included.

The overall elastic response is needed as input properties for the homogenized composite during indentation modeling, for both the entire test material in the “homogenized model” or for the lower portion of the “multilayer model.” The five independent elastic constants for each of the three volume fractions used in the indentation modeling are listed in Table 4.1.

Table 4.1 Five independent elastic constants for the three composite models: Al75/SiC25, Al50/SiC50 and Al25/SiC75.

Composite	E_{11} (GPa)	E_{22} (GPa)	ν_{12}	ν_{13}	G_{12} (GPa)
Al75/SiC25	114.2	84.8	0.3215	0.2357	27.8
Al50/SiC50	168.7	116.9	0.2789	0.2002	37.4
Al25/SiC75	222.9	168.3	0.2265	0.1815	56.8

b) Indentation analysis of Al50/SiC50 composite

We now present the results from indentation modeling. Figure 4.5 shows a representative indentation load-displacement curve for the multilayer model of Al50/SiC50, with a maximum indentation depth at 100 nm (equal to two initial layer thicknesses in this case). All other models show the same qualitative features. The initial slope during unloading was used to calculate the indentation-derived elastic modulus of the composite.

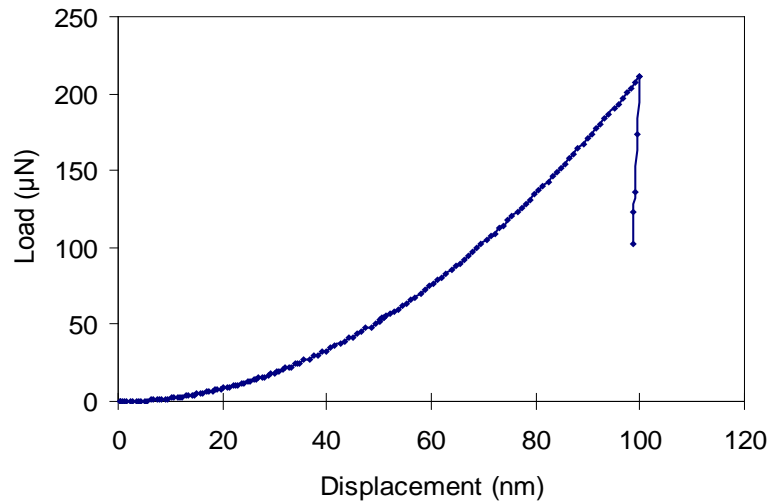


Figure 4.5: A representative indentation load-displacement response obtained from the finite element modeling. This curve corresponds to the multilayer model Al50/SiC50, with the maximum indentation depth at 100 nm.

Figure 4.6 shows the numerical results of the indentation-derived elastic modulus as a function of indentation depth, for the case of Al50/SiC50. The maximum indentation depth shown is 700 nm, which corresponds to a depth of 14 initial layer thicknesses. For reference the modeled result for a pure Al specimen is also included, which shows a constant modulus value over the range of indentation depth considered. The Al50/SiC50 composite response is represented by three curves in Figure 4.6: one of the homogenized model and two of the multilayer model. The difference in the two multilayer cases is the material used as the topmost layer, Al or SiC.

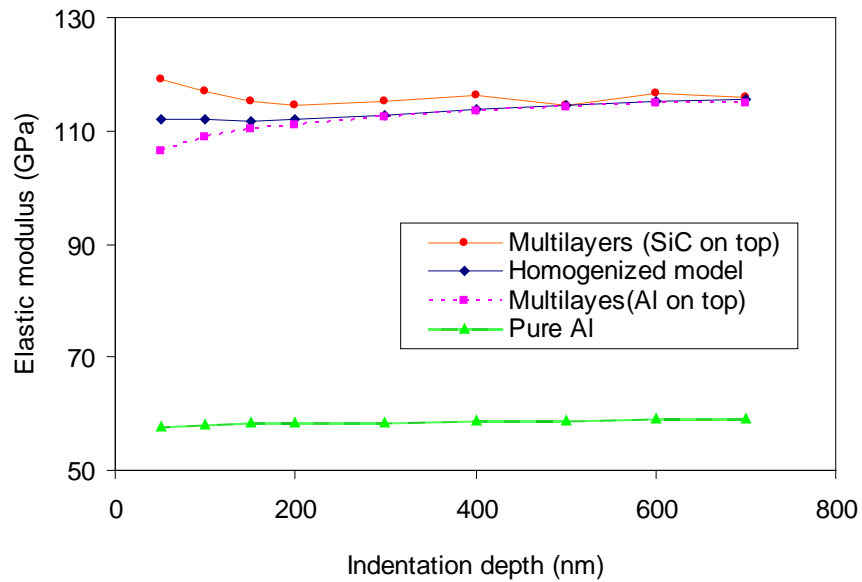


Figure 4.6: Indentation-derived elastic modulus, obtained from the finite element analysis, of the Al50/SiC50 composite as a function of the indentation depth. The result of pure Al is also included for reference. In addition to the homogenized model, two curves for the multilayer model are presented: one with Al being the topmost layer and the other with SiC being the topmost layer.

It can be seen from Figure 4.6 that, when the indentation is relatively shallow, the response of the multilayer model is sensitive to the first-layer material in contact with the indenter. If Al is the topmost layer, the elastic modulus is relatively low and vice versa. The three curves tend to converge when the indentation depth is large (beyond about 400-500 nm, or 8-10 initial layer thicknesses). The merging of the curve of the multilayer model (with Al on top) to that of the homogenized model appears at an even smaller indentation depth. We can conclude that, when performing nanoindentation tests on metal-ceramic multilayers

consisting of a large number of layers, a depth of indentation beyond several initial layer thicknesses may be sufficient for generating the “true” elastic response of the composite.

c) Other Al/SiC thickness ratios

Next we consider results of the Al75/SiC25 and Al25/SiC75 composites. Only the multilayer model with Al being the topmost layer is presented here. Figure 4.7 shows the modeled indentation-derived elastic modulus as a function of indentation depth. The result of Al50/SiC50 is also included in the figure for comparison. The modulus variation follows the same trend in all three cases. With a sufficient indentation depth a steady modulus value can be reached. The numerical values are 83.9 GPa, 114.9 GPa, and 167.9 GPa for Al75/SiC25, Al50/SiC50, and Al25/SiC75, respectively.

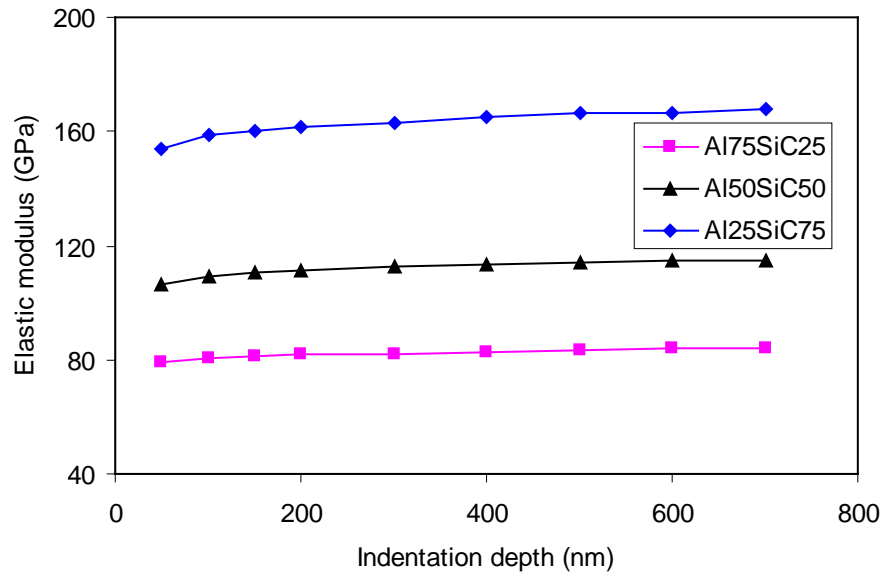


Figure 4.7: Indentation-derived elastic modulus as a function of the indentation depth for the composites Al75/SiC25, Al50/SiC50 and Al25/SiC75.

The correlation between the indentation-derived elastic modulus, which is a single value, and the effective anisotropic elastic property of the composite, is shown in Figure 4. 8. Here the modulus values (at the deepest indentation considered) for the three multilayer composites Al75/SiC25, Al50/SiC50 and Al25/SiC75 are overlaid on the plot showing the variation of composite E_{11} and E_{22} with the SiC volume fraction. It is evident that the three discrete points in Figure 4.8 are very close to the E_{22} curve. This observation suggests that the modulus obtained from indentation may be a good representation of the overall *transverse* elastic modulus of the multilayers.

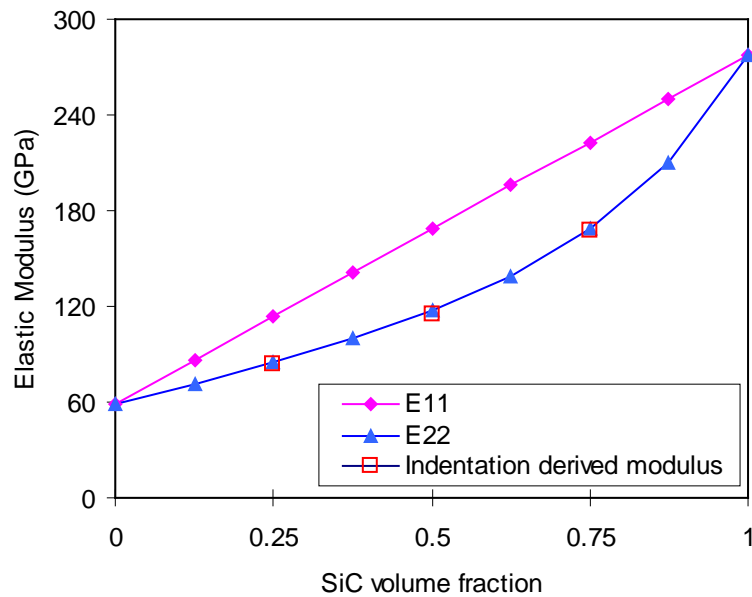


Figure 4.8: Comparison of the overall longitudinal modulus E_{11} and transverse modulus E_{22} with the indentation-derived modulus values of the composites Al75/SiC25, Al50/SiC50 and Al25/SiC75.

4.4 Conclusions

In this chapter a systematic finite element analysis was carried out to study the effective elastic modulus of metal-ceramic multilayers obtained from the indentation technique. The composite structure considered consists of a large number of layers and is free from any substrate effect. Using Al/SiC as a model system, the modulus values, calculated from the modeled indentation load-displacement curve during unloading, were compared with the overall elastic property of the composites. It is noted that Al crystals possess a high degree of isotropy and the SiC layers in this study are amorphous. The continuum approach employed in this work is therefore appropriate. It was found that, when the indentation reaches beyond about 8-10 initial thicknesses of the individual layers, the indentation response becomes representative of the entire composite. The multilayer modulus derived from the indentation test is consistent with the overall transverse (out-of-plane) modulus of the composite. The findings apply to a wide range of relative thicknesses between the metal and ceramic layers, and should serve as a useful guidance for experimental characterization of multilayer elastic behavior using instrumented indentation. The composite geometry used in this chapter consists of essentially “infinite” number of alternating metal and ceramic layers, so the possible effect of the underlying substrate material was avoided. In reality this condition is not always met. In the following chapter we will focus on experimental and numerical work involving Al and SiC nanolayers on a silicon substrate, for attempting a thorough understanding of the interaction between the substrate and the layers, as well as their combined effect on the indentation response.

Chapter 5 Effective Indentation Response of “Finite” Layers

In this chapter, models of multilayer composite on a substrate are considered. The substrate effect on the elastic modulus and hardness of a multilayered model is studied, and the results are compared with the experiments. The geometry of nanolayers in the experiment is the same as that used in the numerical modeling. Some results presented in this chapter have been published in [82].

5.1 Experimental background

The Al and SiC layers were magnetron-sputtered on the (111) single-crystal Si substrate. The base pressure of the dual-gun sputtering chamber was approximately 10^{-7} Torr (1.33×10^{-7} Pa). Targets of pure Al (99.99%) and SiC (99.5%) (Kurt Lesker, Clairton, PA) were used for sputtering in argon atmosphere, at an argon pressure of about 3 mTorr (0.4 Pa). The Al was sputtered using a DC sputter gun with a power of 95 W while the SiC was sputtered by a RF sputter gun at 215 W. The targets were pre-sputtered for about 10 min at 40 W for Al and 95 W for SiC to remove any oxides and impurities from the surface. Under these conditions, the deposition rates were 7.5 nm/min and 3.9 nm/min for Al and SiC, respectively.

Nanoindentation was conducted using a commercial nanoindenter (Nano-XP, MTS Systems, Minneapolis, MN). The CSM technique was employed to obtain the Young's modulus and hardness as a function of indentation depth [83]. Focused ion beam (FIB), scanning electron microscopy (SEM) and transmission electron microscopy (TEM) were employed for characterization of the cross-section microstructure. The post-indented samples were cross-

sectioned along the thickness for damage examination. A thin platinum layer was deposited on the sample prior to FIB machining to minimize ion beam damage. Further experimental details can be found in Ref. [31].

5.2 Indentation modeling

Two model systems are considered for indentation. One has 7 alternating layers of Al and SiC on a Si substrate; the other has 41 alternating layers of Al and SiC on a Si substrate.

Figure 5.1 shows a representative schematic of multilayer Al/SiC films on Si. These choices of Al/SiC layers were based on the actual number of layers in the experimental studies.

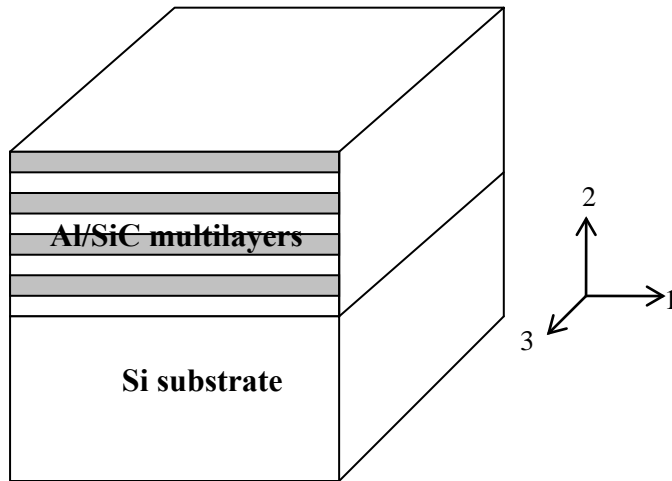


Figure 5.1: Schematic showing the alternating metal-ceramic layers on substrate considered in this study.

Simulations of indentation were based on an axisymmetric model featuring an elastic conical indenter. Figure 5.2 shows the schematic of the model of indentation. The left boundary is treated as the symmetry axis. The boundary conditions of the model are the same as those provided in Chapter 3 and Chapter 4. The input elastic and plastic properties of Al, SiC, Si and diamond were given in Chapter 3.

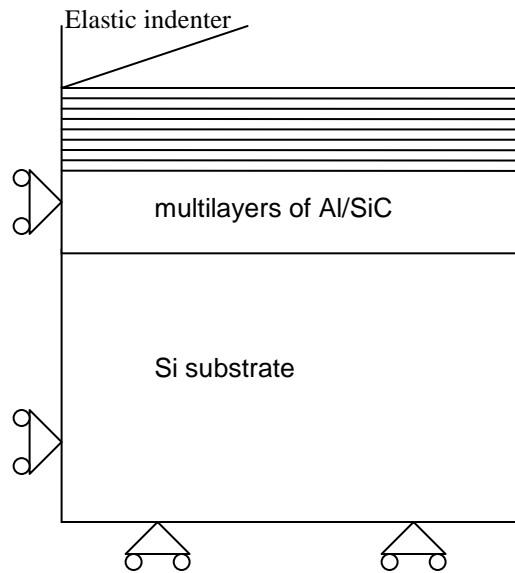


Figure 5.2: Schematic showing the multilayer on substrate model and the boundary conditions for indentation modeling. The specimen and indenter both possess axial symmetry about the left boundary. The rigid indenter has a semi-angle of 70.3°.

Equations (3.1) and (3.2) are used to calculate the elastic modulus. In our simulation the parameter β was determined to be 1.11 for the 7-layer model and 1.04 for the 41-layer model following the same approach provided in Chapter 3. The calculation of indentation-derived modulus (Equation (3.2)) E from E_r requires a known Poisson's ratio of the composite.

Again

we used the ν_{23} value obtained from the modeling of overall uniaxial loading of the Al/SiC composite, as described in Chapter 4. In experiments, the contact area A is calculated from the indenter geometric relation

$$A = 24.5h^2 \quad (5.2)$$

where h is the indentation depth. The area A obtained from Equation (5.2) is defined as the theoretical contact area ($A_{theoretical}$), which has no pile up or sink in taken into account. It should be noted that the post-indentation specimens showed that pile-up took place [31]. In the finite element modeling the contact area can be directly obtained from the deformed model showing pile-up (A_{true}). In the following discussion, we will include two sets of modulus and hardness values from experiments: one with theoretical contact area and the other with true contact area obtained from modeling.

a) 7-layer Al/SiC on Si

The indentation model we considered can be represented by Figure 5.2. The material model consists of 7 alternating Al and SiC layers above a silicon (Si) substrate. The overall size of the entire specimen is 1.5 μm in lateral span (radius) and 1 μm in height. In the upper portion of the model there are a total of 7 alternating layers of Al and SiC and the top layer is Al. Following the experimental conditions, three different volume ratios of Al/SiC are considered for indentation modeling: Al50/SiC30, Al50/SiC50 and Al50/SiC70 (again, the numbers represent the thickness of the individual layer, in nm). A total of 29,852 linear elements were used in the model, with a finer mesh size near the upper-left corner.

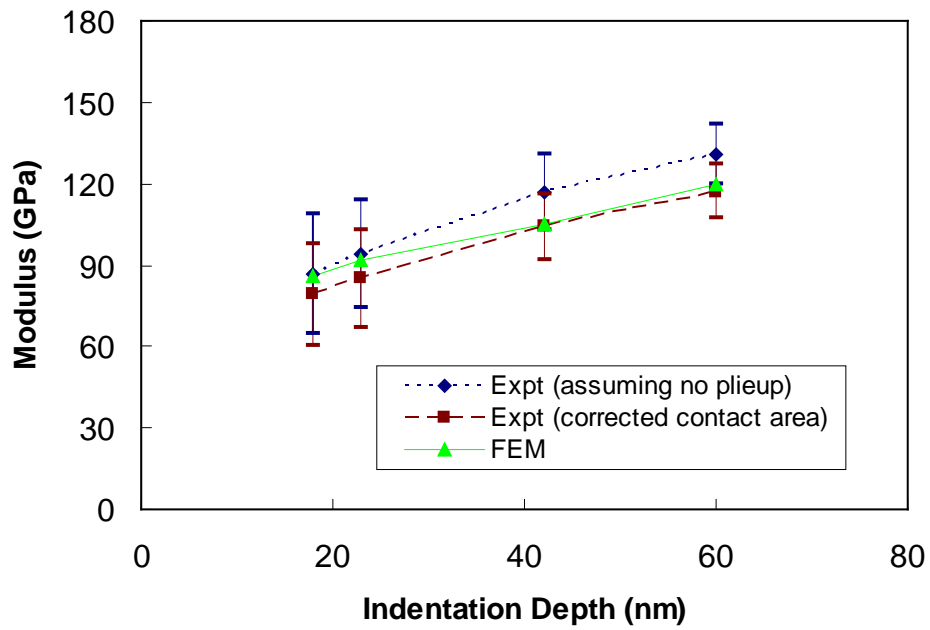
b) 41-layer Al/SiC on Si

The indentation model we considered can also be represented by Figure 5.2. The material model consists of 41 alternating Al and SiC layers above a silicon (Si) substrate. The overall size of the entire specimen is taken as 40 μm in lateral span (radius) and 43 μm in height. The top layer is Al. The thickness of each Al or SiC layer is 50 nm. A total of 173,105 linear elements were used in the model, with a finer mesh size near the upper-left corner.

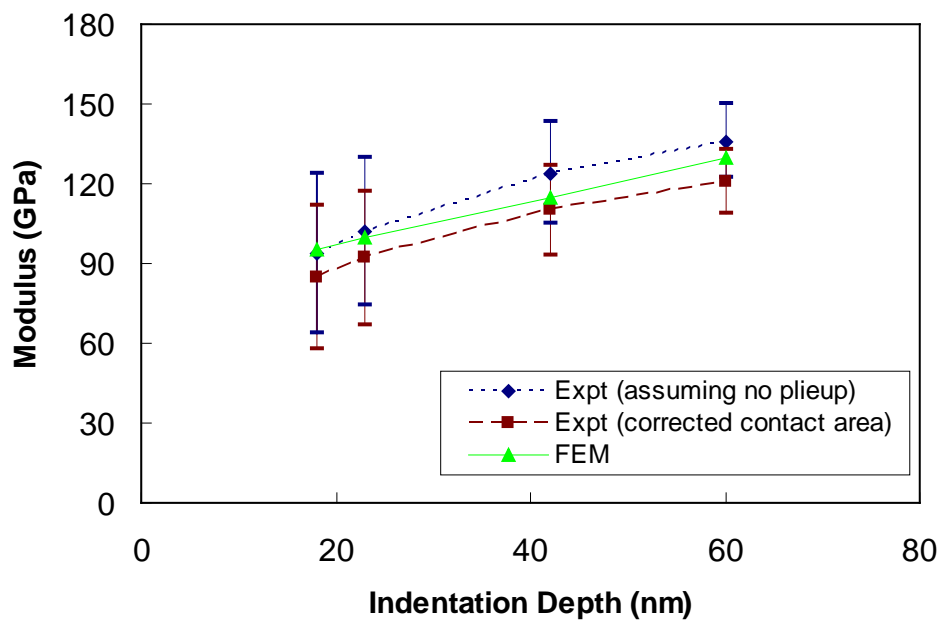
5.3 Numerical results

a) 7 layer Al/SiC on Si

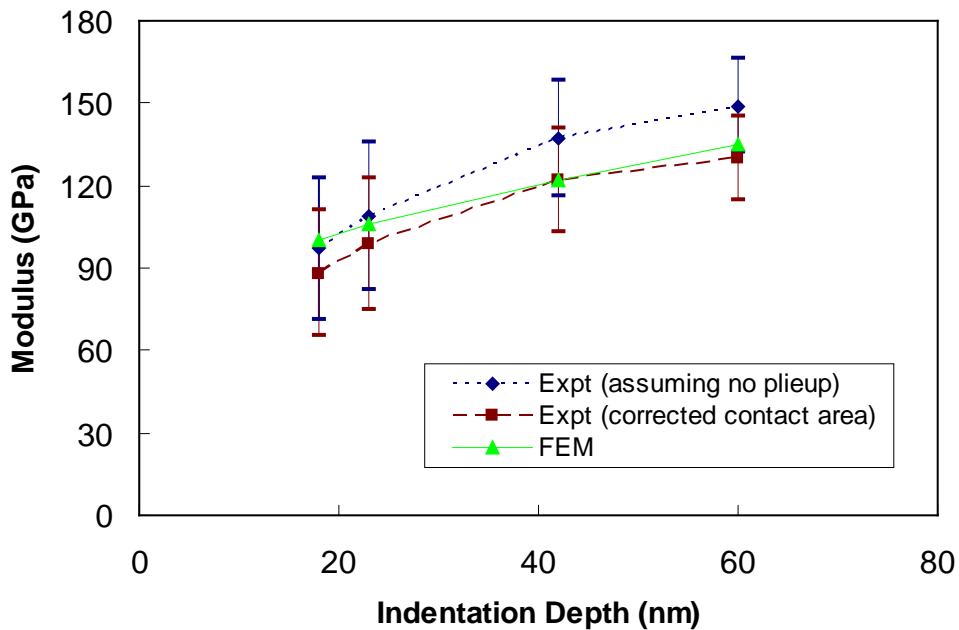
The elastic modulus values as a function of indentation depth, obtained from experiments and finite element modeling, for the Al50/SiC30, Al50/SiC50 and Al50/SiC70 materials are shown in Figures. 5.3 (a), (b), and (c), respectively. The range of indentation depth considered spans from 18 nm (well within the initial top Al thickness) to 60 nm (well into the first SiC layers). In each figure there are two sets of experimental data, which were obtained based on two different calculated contact areas ($A_{theoretical}$ and A_{true}). The one marked with “Expt (assuming no pile up)” is obtained from the contact area $A_{theoretical}$. The one marked with “Expt (corrected contact area)” is obtained from the contact area A_{true} .



(a)



(b)



(c)

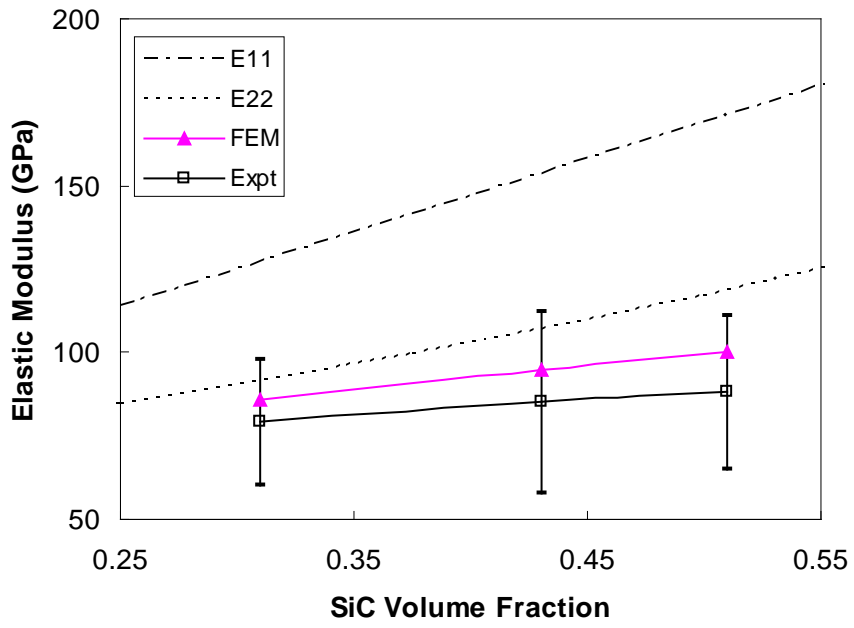
Figure 5.3: Experimental and modeling results of the Young’s modulus as a function of indentation depth for the (a) Al50/SiC30, (b) Al50/SiC50 and (c) Al50/SiC70 materials.

It can be seen that the contact area correction results in a reduction of modulus values due to the larger true contact area. The modulus increases with indentation depth because of the increasing influence of the SiC layers and the Si substrate. It is noted that, in all cases, the Young’s modulus values are greater than that of a single Al film (measured to be 59 GPa). Figures 5.3 (a)-(c) also show that the modeling result follows the same trend as the experiment. (The modeling result is based on the direct true contact area.) At shallow indentation, the modeling result is close to the “uncorrected” experimental value. At greater indentation depths, however, the agreement is better between modeling and the “corrected”

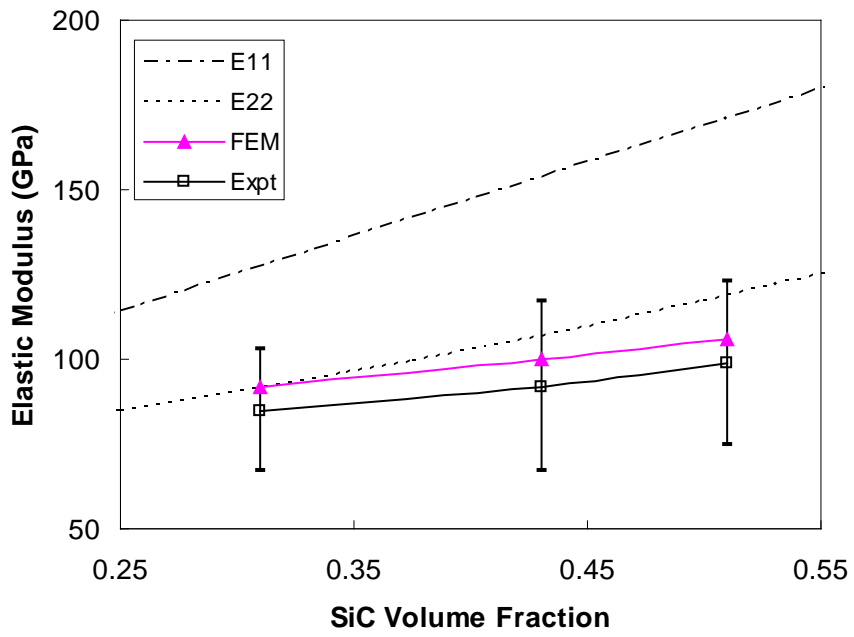
experimental data. This tendency implies a more accurate determination of the contact area (better confidence) at larger depths and an increasing influence of the pile-up effect in the actual measurement.

Although the indentation depth considered in this part of the study is relatively small, some insight can still be gained by comparing the result with the *true composite modulus* of the layered composite. When the entire Al/SiC laminates is treated as a composite, the material is anisotropic but possesses in-plane isotropy. In this case there are five independent elastic constants as described in Chapter 4. Our focus is on the longitudinal modulus E_{11} and transverse modulus E_{22} (i.e., the upper and lower bounds, respectively) where the coordinate system is defined in Figure 5.2. Figure 5.4 shows the calculated E_{11} and E_{22} overlaid on the indentation-derived modulus data resulting from the experiment (with corrected contact area) and modeling presented in Figure 5.3. Note E_{22} should be the true composite modulus when loaded along the indentation direction [77]. Parts (a), (b), (c) and (d) in Figure 5.4 show the comparisons corresponding to the indentation depths of 18 nm, 23 nm, 42 nm and 60 nm, respectively, and the different layer thicknesses are represented by the SiC volume fraction of the Al/SiC composite. When the indentation depth is small, the indentation results are seen to fall below the E_{22} curve (Figures 5.4(a) and (b)). As the depth increases to 42 nm (Figure 5.4 (c)), the indentation-derived modulus already exceeds the composite E_{22} value for any fixed SiC volume fraction. We attribute this mainly to the Si substrate effect, especially because this indentation depth is already about 10 to 15% of the total thickness of the Al/SiC film stack. The SiC layers underneath are not able to give rise to such an increase in modulus

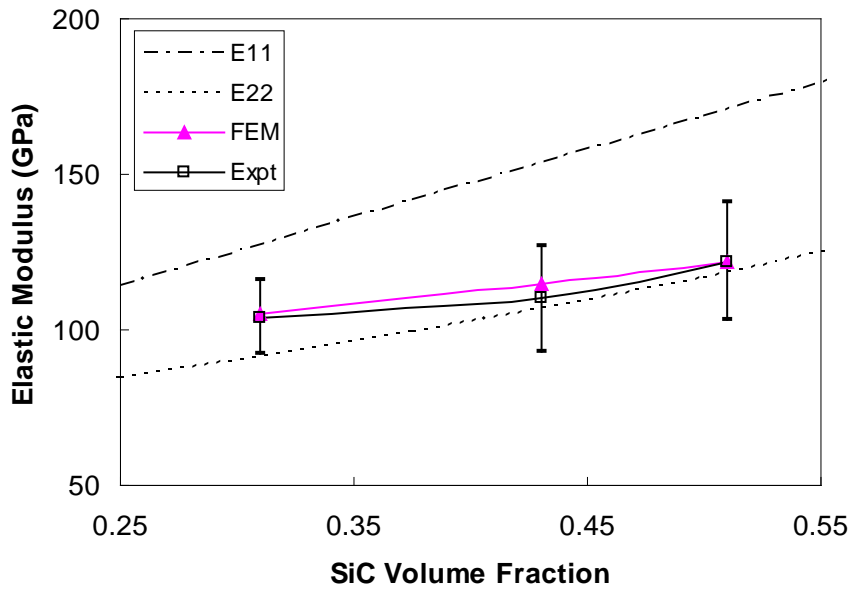
(beyond E_{22}), as was found in our previous study free of the substrate effect in Chapter 4. At a depth of 60 nm (Figure 5.4 (d)), the indentation result is at an even higher position relative to E_{22} . Note that the case of the lowest SiC volume fraction corresponds to the highest ratio of penetration depth/total film thickness, and hence the greatest influence of the substrate. This can explain the trend in Figures 5.4 (c) and (d) that a smaller SiC volume fraction results in a relatively higher modulus over the span between E_{11} and E_{22} .



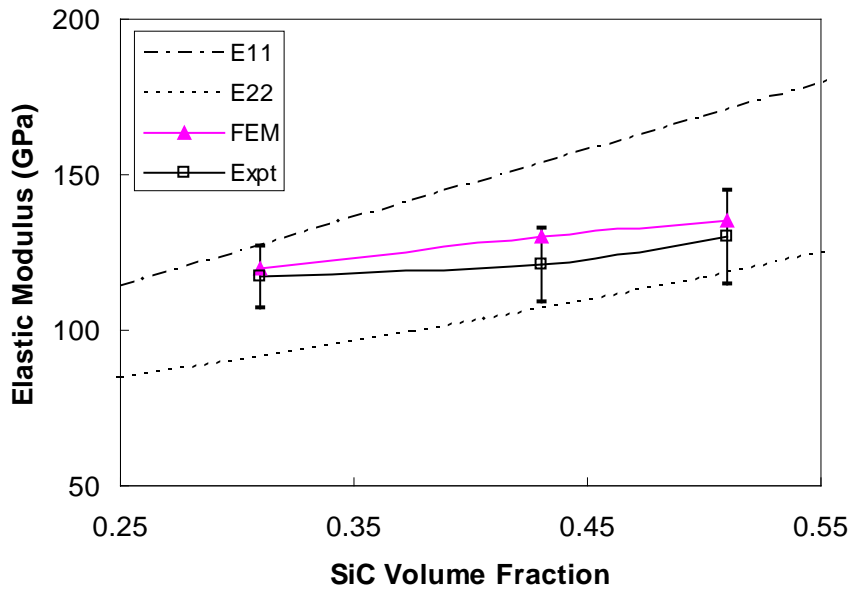
(a)



(b)



(c)



(d)

Figure 5.4: Comparison of elastic modulus obtained from experimental indentation measurement (“Expt”), indentation modeling (“FEM”), and modeling of overall composite modulus (“E11” and “E22”) when the indentation depth is at (a) 18 nm, (b) 23 nm, (c) 42 nm and (d) 60 nm.

b) 41-layer Al/SiC on Si

In this section both the indentation-derived elastic modulus and hardness are included in the discussion. Figure 5.5 shows the modeled load-displacement curve with a maximum indentation depth at $0.5 \mu\text{m}$ (which corresponds to 10 initial layer thickness).

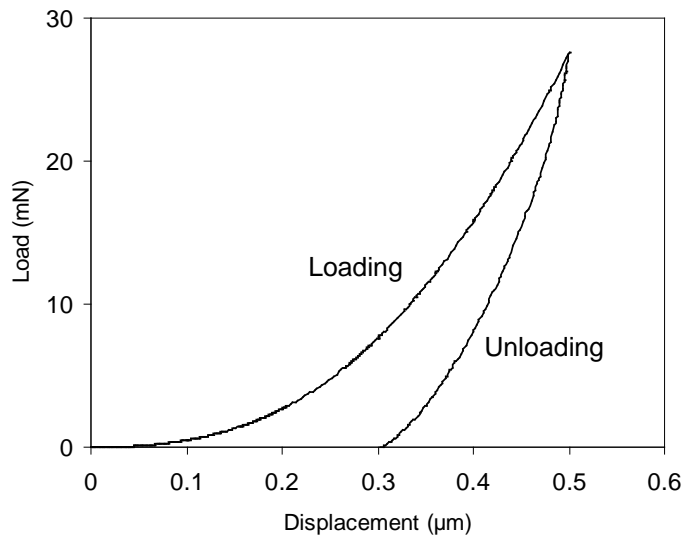
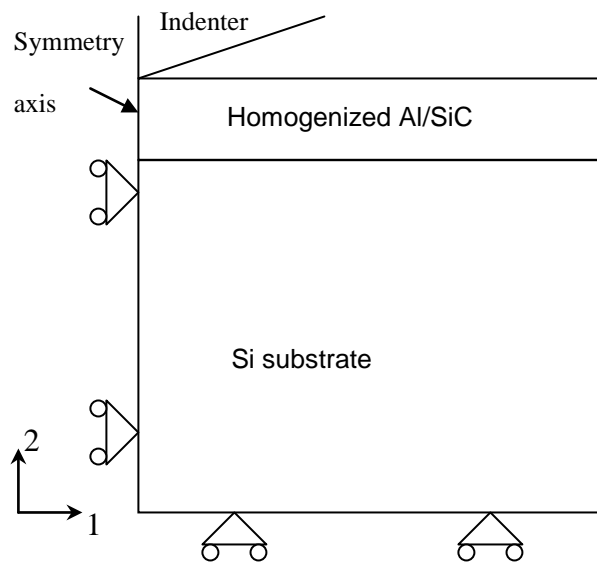


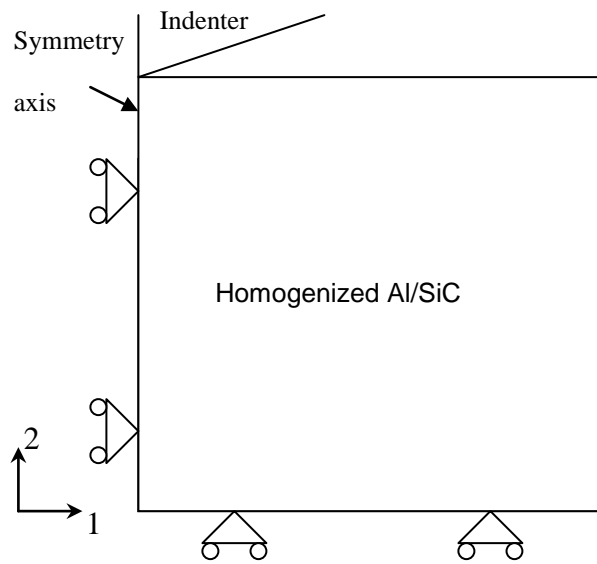
Figure 5.5: Simulated load-displacement curve during indentation loading and unloading.

For the purpose of gaining fundamental insight into the indentation response, two additional models are used here as depicted in Figures 5.6 (a) and (b). First, the 41 layers of Al/SiC in Figure 5.2 are replaced by a homogeneous material having the effective properties of the Al/SiC multilayered composite, Figure 5.6 (a). The Si substrate in the model remains unchanged. The effective elastic-plastic stress-strain response of the homogenized material was obtained by a separate finite element analysis of overall compression loading along the through-thickness direction of the Al/SiC multilayers. In particular, the anisotropic elastic behavior, with five independent elastic constants for the transversely isotropic composite, is

accounted for in the homogenized model as discussed in Chapter 4. In Figure 5.6 (b), the Si substrate is also replaced by the homogenized Al/SiC multilayers. The difference between the cases in Figures 5.6 (a) and 5.6 (b) is that the effect of the Si substrate on the indentation response can be examined. The models in Figures 5.2, 5.6 (a) and 5.6 (b) are henceforth termed “Al/SiC multilayers on Si,” “homogenized Al/SiC on Si,” and “homogenized Al/SiC,” respectively.



(a)



(b)

Figure 5.6: Schematics showing the two additional models: (a) the 41 layers of Al/SiC is replaced by the homogenized Al/SiC composite above the Si substrate; (b) the entire material is the homogenized Al/SiC composite.

Figure 5.7 shows the simulated indentation hardness as a function of indentation depth for the three models, up to a maximum depth of 1000 nm (about one half of the total thickness of the multilayers). It can be seen, by comparing the cases of “homogenized Al/SiC on Si” and “homogenized Al/SiC,” that the Si substrate effect on hardness is negligible when the indentation is shallower than about 500 nm. The influence of the substrate becomes apparent at a depth of 1000 nm, where an approximately 12% increase in hardness is observed. The model “Al/SiC multilayers on Si” in Figure 5.7, however, shows much lower hardness values compared to the other two. At small indentation depths, the top Al layer plays a relatively important role in affecting the composite modulus so a lower hardness results. The overall hardness increases as the indentation goes deeper (due to the increasing influence of SiC layers as well as the Si substrate). However, at 1000 nm the hardness is still quite far behind the homogenized composite response.

It is worth mentioning that the difference resulting from utilizing explicit multilayers and homogenized composite in the model, observed in Figure 5.7, is not merely a consequence of the indentation depth considered in the analysis. We found that, with the homogenized approach the pile-up at the indentation edge is much reduced compared to the case with the individual Al/SiC multilayers. Therefore the projected contact area, A , used in obtaining the hardness, is also significantly affected. This fundamental difference, along with the discrepancy shown in Figure 5.7, illustrate that, when modeling the indentation behavior of a heterogeneous structure such as the multilayers considered here, a homogenization approach may yield very inaccurate results. (Similar findings for particle-reinforced composite systems

have also been reported [84, 85].)

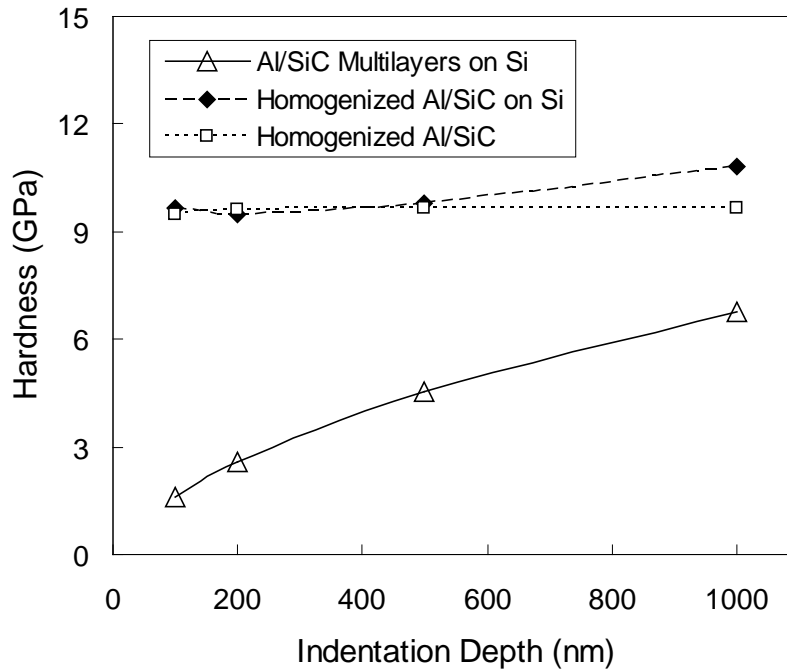


Figure 5.7: Simulated indentation hardness as a function of indentation depth, for the three models “Al/SiC multilayers on Si” (Figure 1), “homogenized Al/SiC on Si” (Figure 10(a)), and “homogenized Al/SiC” (Figure 10(b)).

Figure 5.8 shows the simulated elastic modulus, obtained from the indentation unloading response, as a function of indentation depth for the three models “Al/SiC multilayers on Si,” “homogenized Al/SiC on Si,” and “homogenized Al/SiC.” A comparison between the cases of “homogenized Al/SiC on Si” and “homogenized Al/SiC” reveals the Si substrate effect. Note the Young’s modulus of Si, 187 GPa, is still much greater than the effective modulus of the Al/SiC composite along the thickness direction, so an increasing trend is seen in the model due to the increasing substrate effect. From Figures 5.7 and 5.8 it can be seen that the

effect of substrate on the elastic property is much more pronounced than on the hardness. The effect on the elastic modulus is significant even when the indentation is shallow (e.g., well within 10% of the homogenized multilayered film thickness). This finding is consistent with that reported in Chapter 3, where a homogeneous Al film on a Si substrate is considered.

When the explicit Al and SiC layers are included in the model (“Al/SiC multilayers on Si”), however, a different behavior of the indentation-derived elastic modulus is observed as in Figure 5.8. Here the modulus remains relatively constant throughout the range of indentation depth. The curve deviates from that of the “homogenized Al/SiC on Si” model as the indentation depth increases, and the apparent substrate effect no longer exists. This may be attributed to the extensive plastic deformation in Al during unloading, which will be reported in the next chapter. The result in Figure 5.8 again raises the issue about the accuracy of using instrumented indentation to quantify the elastic behavior of the multilayered composite.

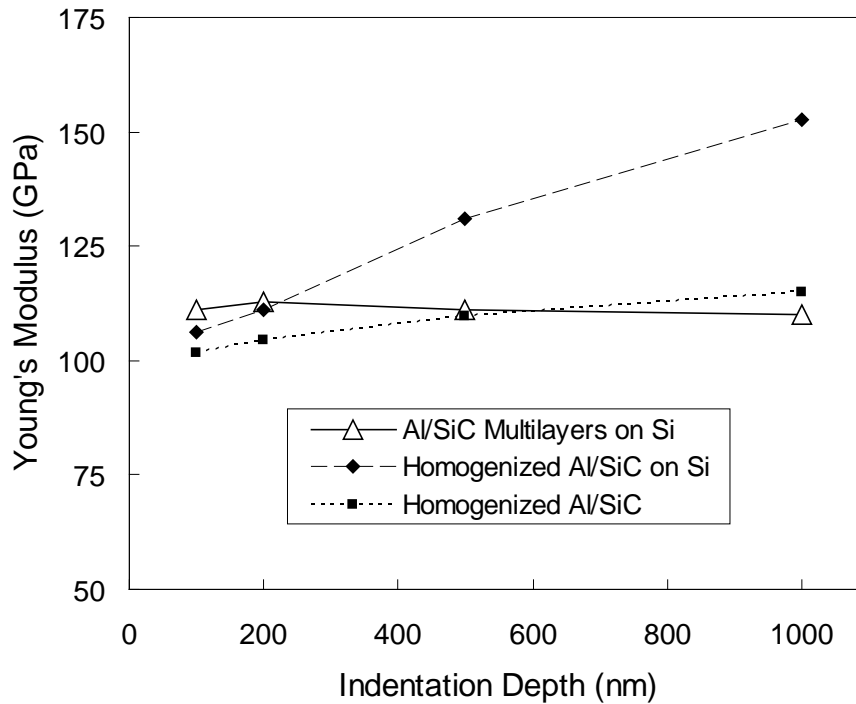


Figure 5.8: Simulated elastic modulus as a function of indentation depth obtained from the simulated unloading part of the indentation curve, for the three models “Al/SiC multilayers on Si” (Figure 5.2), “homogenized Al/SiC on Si” (Figure 5.7(a)), and “homogenized Al/SiC” (Figure 5.7(b)).

Next we consider the overall hardness and elastic modulus obtained from the indentation experiments. The hardness values as a function of indentation depth, obtained from experiments and finite element modeling, are shown in Figure 5.9. The range of indentation depth considered here spans from 100 nm to 1000 nm. In the figure there are two sets of experimental data, which were obtained based on two different calculated contact areas. The labels “assuming no pileup” and “corrected contact area” are defined previously in this chapter. From the finite element analysis, the hardness increases significantly with

indentation depth for the range considered (same as the model “Al/SiC multilayers on Si” shown already in Figure 5.7). The corrected experimental values in Figure 5.9 show a similar trend, although the measured hardness is higher than the numerical prediction when the indentation is shallower and it becomes close to, although a little lower than, the numerical prediction when the indentation is deeper. The discrepancy may be due to the uncertainty of the quantitative yield behavior used as input in the continuum-based model. It is worth pointing out that, compared to the numerical results of “Al/SiC multilayers on Si” and “homogenized Al/SiC on Si” presented in Figure 5.7, the experimental results in Figure 5.9 are much closer to the model “Al/SiC multilayers on Si,” further illustrating the importance of incorporating the explicit layered structure in the modeling analysis.

Figure 5.10 shows the comparison of elastic modulus obtained from the indentation measurement and finite element modeling. As in the case of hardness, two sets of experimental data, one assuming no pile-up and the other with corrected contact area are included in the figure. It can be seen that the corrected experimental modulus values are 10-40 GPa greater than the numerical prediction. The difference is smaller when the indentation depth is small. Further discussion will be given in section 5.4 and in Chapter 6 when the deformation field in the Al layers is investigated.

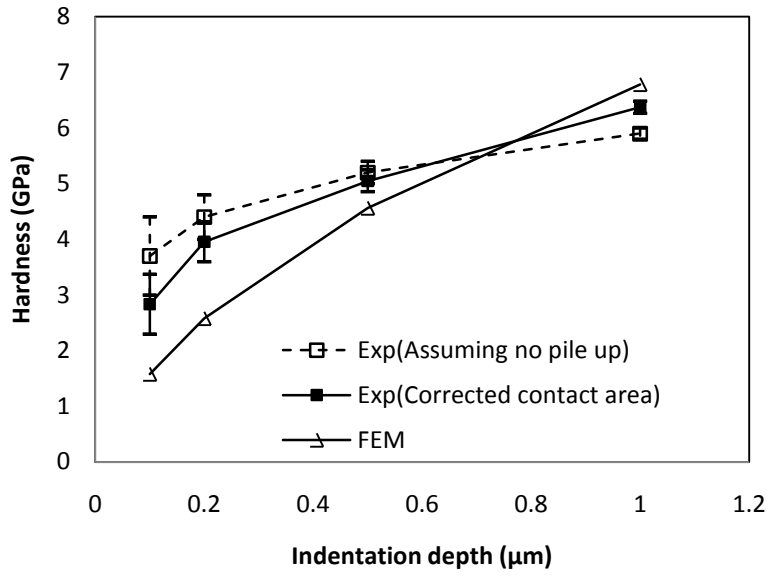


Figure 5.9: Comparison of experimental and modeling results on the hardness as a function of indentation depth.

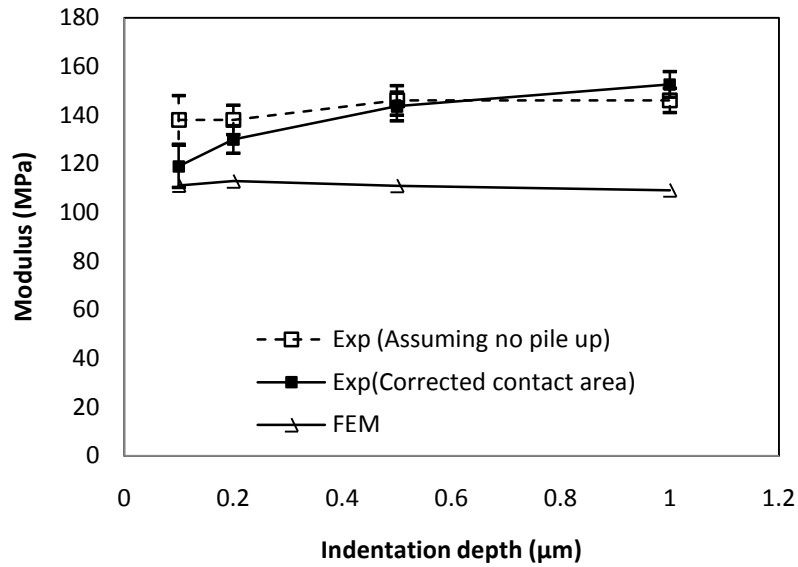


Figure 5.10: Comparison of experimental and modeling results on the indentation-derived Young's modulus as a function of indentation depth.

5.4 Conclusions

The numerical modeling is based on simple elastic-plastic response of the constituents. The finite element model assumed perfect interfaces between the layers (i.e., the displacement field is continuous so sliding along interfaces is prohibited). The quantitative mechanical characteristic of the Al-SiC interface is not known. Hence the interface compliance may also be a source of uncertainty. In the experiments, plastic deformation in metallic nanolayers can be strongly affected by interface-mediated dislocation mechanisms [86, 87], although this effect on elastic response is expected to be small because the elastic modulus is independent of dislocation activities. In addition the finite element modeling uses an ideal laminate geometry. In the actual materials there always exists non-ideal laminate geometry. The top Al layer is not smooth. Inside the layered structure, small “bulges” and depressions of SiC layers were also common (Figure 1.1), so the SiC layers are more of a wavy shape rather than a perfect thin flat plate. Note these geometric features represent a structurally stiffer layout (compared to a perfectly planar structure of uniform thickness) upon bending deflection, which is essentially what SiC experiences during indentation. Therefore a stiffer indentation response from actual experiments is to be expected.

In conclusion, we have found the importance of using explicit composite models in obtaining accurate indentation response. A homogenized model is prone to significant errors. As in the case of a single-layer film on a substrate, the substrate material also influence the indentation-derived elastic modulus of the metal-ceramic multilayers to a significant degree. The multilayer hardness, on the other hand, is relatively insensitive to the substrate. The

interaction between the substrate and multilayered thin films, along with their combined effect on nanoindentation behavior is apparently a complex problem. They may also contribute to internal local damages during indentation loading, as will be examined in the next chapter.

Chapter 6 **Analysis of Indentation Induced Deformation Field and Local Damage**

In this chapter we focus on the evolution of stress and deformation fields and internal damages during indentation tests. Some of the results presented in this chapter have been published in [34, 88].

6.1 Experiment observations

Figure 6.1 shows a FIB cross section of a representative indentation on the multilayers [31]. A part of the Berkovich indentation mark behind the sectioned surface is visible. It can be seen that a symmetric pattern of damage exists. Two mid-level cracks appeared below the edge of the indentation. Further below, cracking near the multilayers/substrate interface has also occurred. These cracks were confirmed to be inside the Al layer. It is noted that these localized failures only appeared below the indentation and are not a result of film deposition.

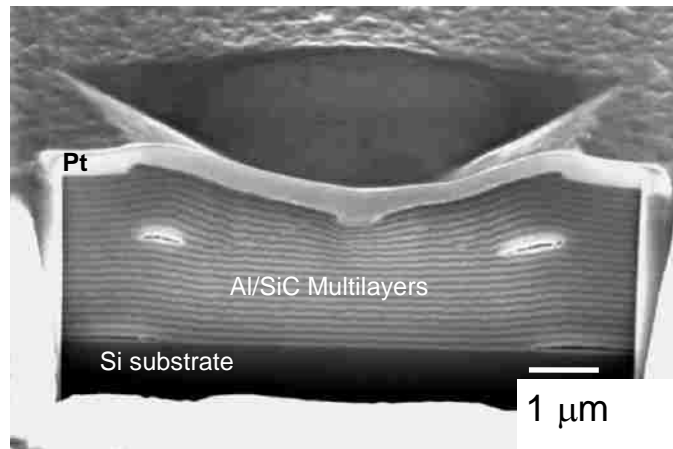


Figure 6.1: Cross-section image showing internal damage under the indentation in the Al/SiC nanolayers. Cracks in the Al layer and at the multilayers/substrate interface are visible, Courtesy of N. Chawla and D. R. P. Singh

In the sections below we present the finite element modeling results which can explain the internal failure patterns observed experimentally. The geometry of nanolayers in the experiment (41-layer Al/SiC on Si) is the same as that used in the numerical modeling.

6.2 Numerical simulations

The axisymmetric model is identical to the “Al/SiC multilayers on Si” used in Chapter 5.

a) Stress and deformation contours

In this section we present a series of contour plots to show the evolution of stress and deformation fields inside the layered structure during indentation loading and unloading.

Plastic yielding follows the von Mises criterion and the incremental flow theory. In terms of the principal stresses σ_1 , σ_2 and σ_3 , yielding commences when

$$\frac{1}{\sqrt{2}} \left[(\sigma_1 - \sigma_2)^2 + (\sigma_2 - \sigma_3)^2 + (\sigma_3 - \sigma_1)^2 \right]^{\frac{1}{2}} = \sigma_y \quad (6.1)$$

where σ_y is the yield strength of the material under uniaxial loading.

Figure 6.2 shows the hydrostatic stress developed in the model near the indentation contact when the indentation depth is at 200 nm (Figure 3(a)) and 500 nm (Figure 3(b)) during loading and after unloading from 500 nm (Figure 3(c)). The same legend scale is used in the three plots so the stress magnitudes can be easily compared. The deformed laminate geometry can be discerned in regions where a large color contrast exists. Figure 6.3 shows the corresponding contour plots of equivalent plastic strain. It can be seen from Figure 6.2 that, directly below the indentation contact, very large compressive hydrostatic stresses were generated. The compressive stress magnitudes in the Al layers are generally much greater than those in SiC. This is due to the different plastic yielding response of the two materials. The soft Al layers (with a small σ_y , Equation (6.1)) have undergone severe plastic deformation, as observed in Figure 6.3, and a large triaxial compressive stress state can be superimposed in the material. While the SiC layers directly below the indentation have also yielded (Figure 6.3), the large yield strength (σ_y) of SiC requires a much less compressive (or even tensile) stresses of σ_{11} and σ_{33} than the highly compressive σ_{22} (see the general relation given in Equation (6.1)). The combination of these primary stress components thus results in a much reduced hydrostatic compression in SiC. This interpretation is also supported by information provided by other stress contour plots to be given below. Even in the Si substrate, large hydrostatic compression exists below the indentation (Figure 6.2). This observation

suggests the importance of the substrate material in affecting the indentation response. Even when the indentation depth is within 10% of the total multilayer thickness (Figure 6.2(a)), significant stress buildup in the Si substrate has begun.

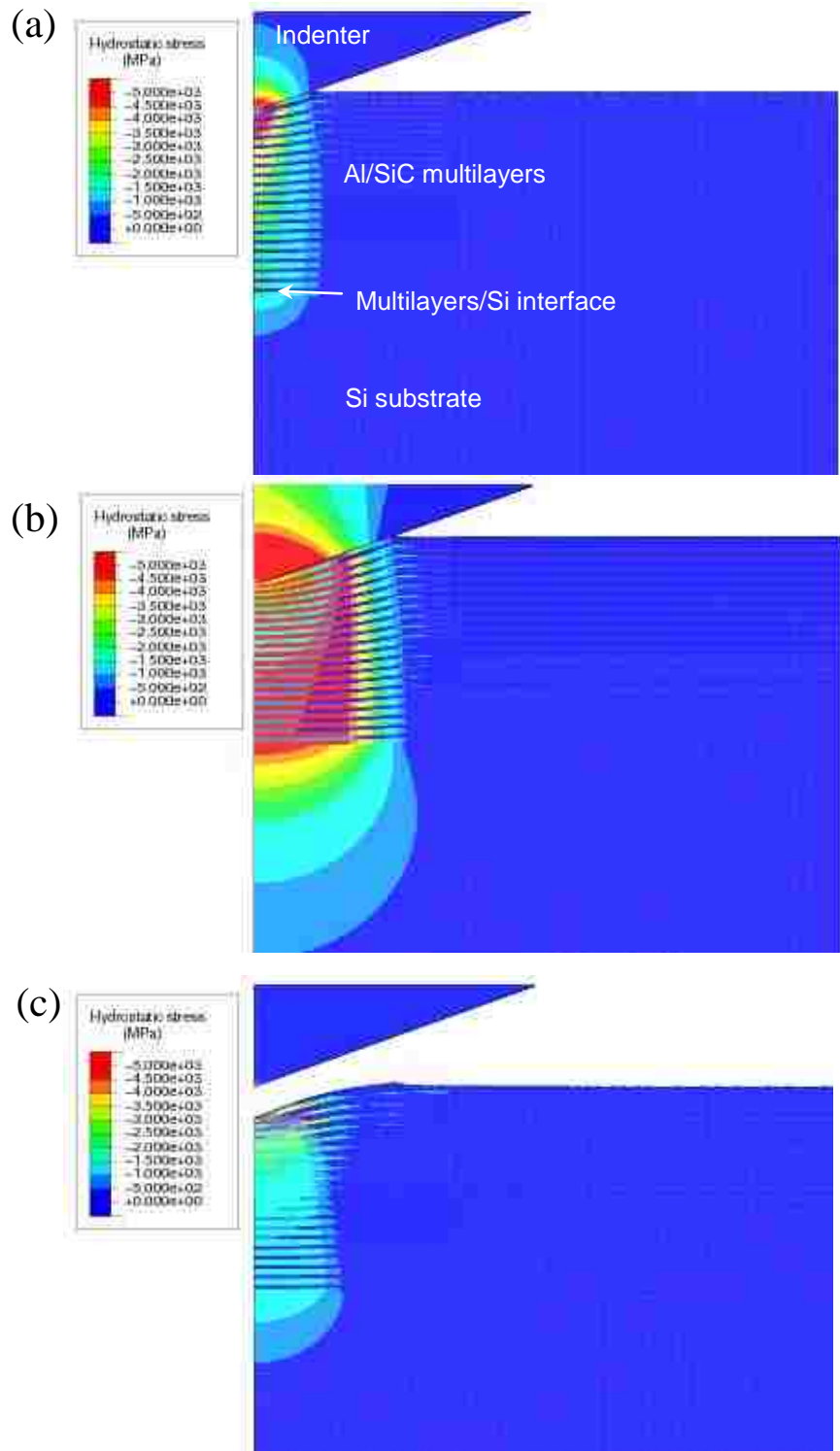


Figure 6.2 Contours of hydrostatic stress near the indentation site, when the indentation depth is at (a) 200 nm, (b) 500 nm, and (c) after unloading.

Upon unloading, the high stresses caused by the indentation were relieved to a great extent. However, considerably large areas, in both the multilayers and substrate, are still under residual compressive stresses well into the GPa range (Figure 6.2(c)). This is a manifestation of the severity of plastic deformation occurred during loading. Another notable attribute about unloading is the evolution of deformation field in Figure 6.3. A comparison between Figures 6.3(b) and 6.3(c) reveals that the equivalent plastic strains in Al have actually *increased* during the *unloading* process. This observation is unique because, in a homogeneous material, indentation unloading is a pure elastic recovery process and the accumulated plastic strain remains unchanged during unloading. (We have confirmed this by carrying out an independent simulation where the Al/SiC multilayers were replaced by a single Al layer of the same total thickness. It was observed that the equivalent plastic strain contours remained exactly the same during indentation unloading.) It is apparent that, in the present case of a heterogeneous structure, the internal constraint induced by the hard and stiff SiC layers has forced the much softer Al to endure continued deformation even though the composite as a whole is undergoing unloading. It is worth mentioning that the same qualitative feature was found to exist when the indentation depth is relatively small. We observed from our simulations that, if unloading starts from a depth of 200 nm (much shallower than the case in Figure 6.3), plastic deformation in some parts of the Al layers can already be detected in the model. The effect becomes more intensified as the indentation depth increases.

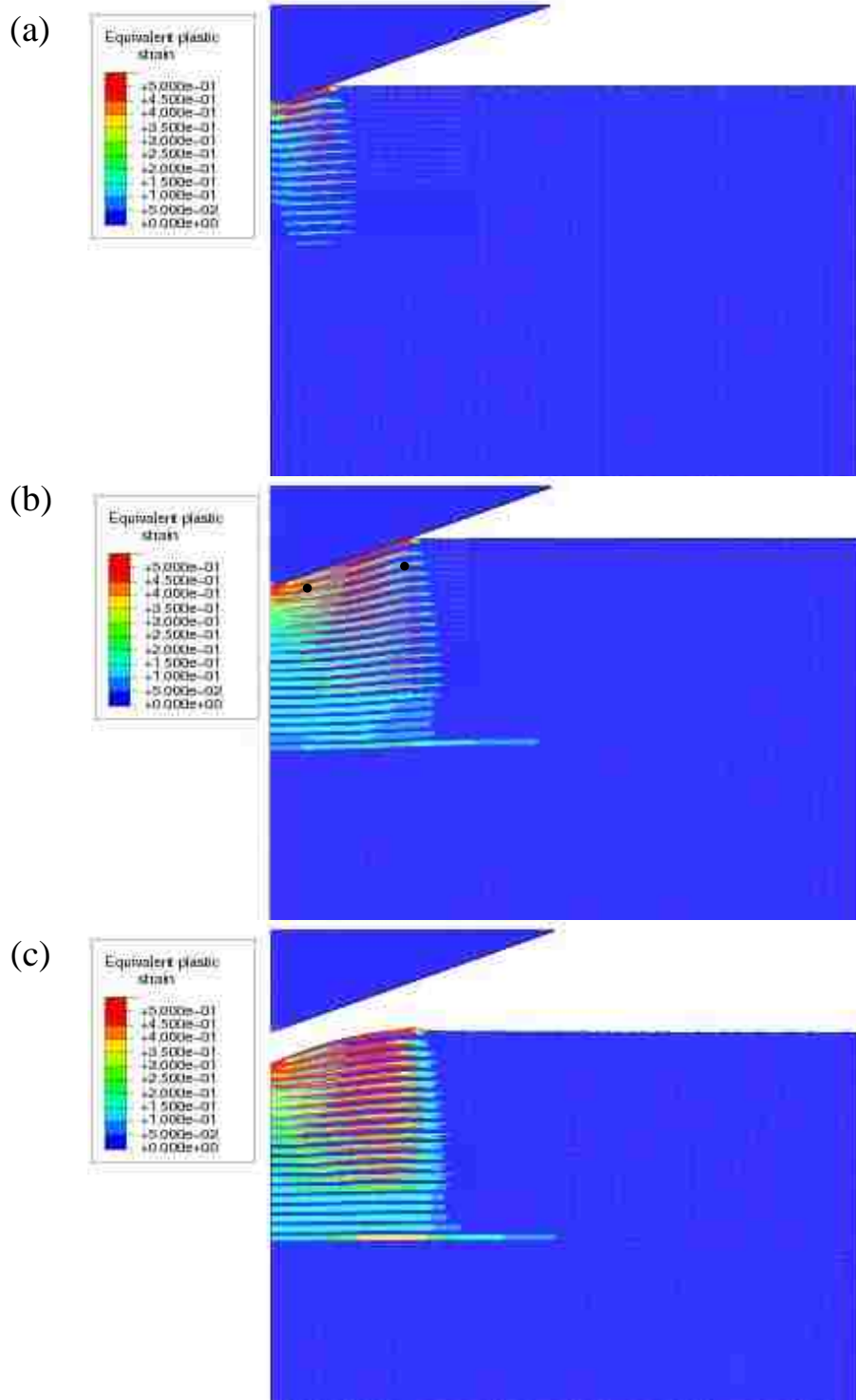


Figure 6.3 Contours of equivalent plastic strain near the indentation site, when the indentation depth is at (a) 200 nm, (b) 500 nm, and (c) after unloading.

Figures 6.4(a), (b) and (c) show the contour plots of maximum principal stress near the indentation contact at depths of 200 nm and 500 nm during loading and after unloading from 500 nm, respectively. It can be seen that, although the Al layers were under high compressive stresses directly below the indentation, significant tensile stresses have actually developed in the SiC layers. An examination of the individual stress components (not shown) revealed that the maximum principal stress in SiC is largely along the “hoop” direction (namely σ_{33}) of the axisymmetric model. Apparently the increased circumferential length associated with the indentation-induced “warping” has contributed to the generation of this in-plane tensile stress. In addition, some parts of the SiC layers have experienced significant tensile stresses of σ_{11} . Note that these tensile stresses in SiC have contributed to the reduced hydrostatic compression compared with Al as seen in Figure 6.2. Figure 6.4(b) also shows that large tensile stresses are present in a small region around the interface between the multilayers and Si substrate as highlighted by the arrow. After unloading, the residual stress remains high as seen in Figure 6.4(c).

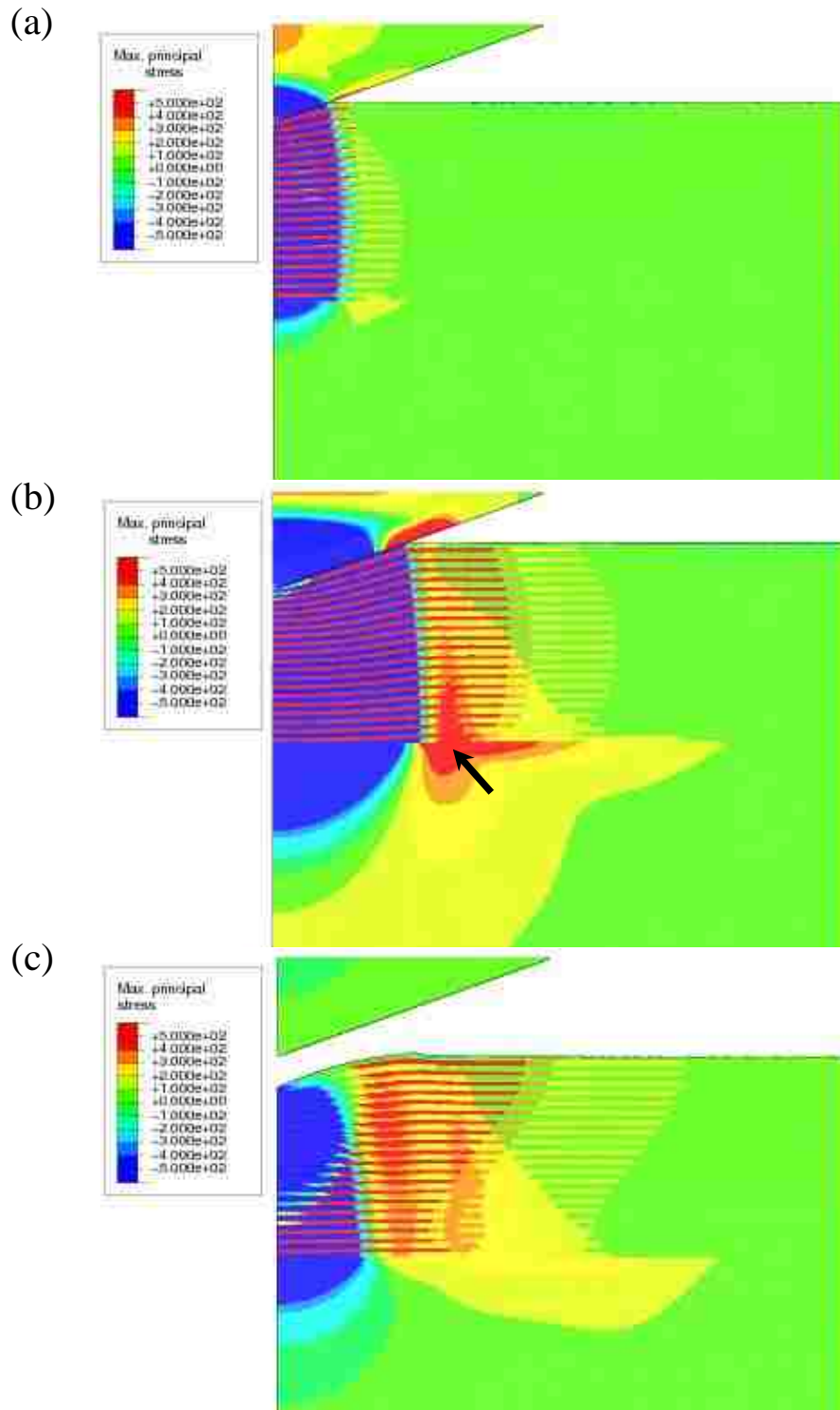


Figure 6.4 Contours of maximum principal stress near the indentation site, when the indentation depth is at (a) 200 nm, (b) 500 nm, and (c) after unloading.

Attention is now turned to the normal stress component acting perpendicular to the layer interfaces. Figure 6.5 shows the contour plots of σ_{22} when the indentation depth is at (a) 200 nm, (b) 500 nm, and (c) after unloading. The contour levels in these figures were adjusted so as to highlight the tensile σ_{22} stresses evolved during loading and unloading (otherwise the localized tensile stresses would be largely “hidden” by the predominant compressive field). It can be seen that tensile stresses in the vertical direction have developed in certain areas below and slightly outside the indentation edge since the early stages of deformation (Figure 6.5(a)). The tensile σ_{22} -stressed region gradually shifts outward and the stress magnitude increases as the indenter moves deeper. At an indentation depth of 500 nm, the maximum tensile stress has well exceeded 200 MPa in many Al and SiC layers as well as in a small region of the Si substrate (Figure 6.5(b)). Upon unloading, Figure 6.5(c), the region with high tensile stresses has shifted slightly inward and two distinct high-stress areas have developed. It is noticed from Figures 6.5(b) to 6.5(c) that the area with tensile σ_{22} stresses has actually *expanded* during *unloading*. This expansion is due to the fact that the heavily compressed material directly below the indentation contact has undergone elastic recovery during unloading, thus imposing a vertical pulling action on the region already under tension. According to our preliminary simulation, the same qualitative feature can in fact be seen even in a homogeneous material. The presence of the laminated structure with brittle SiC layers was found to further enhance this phenomenon.

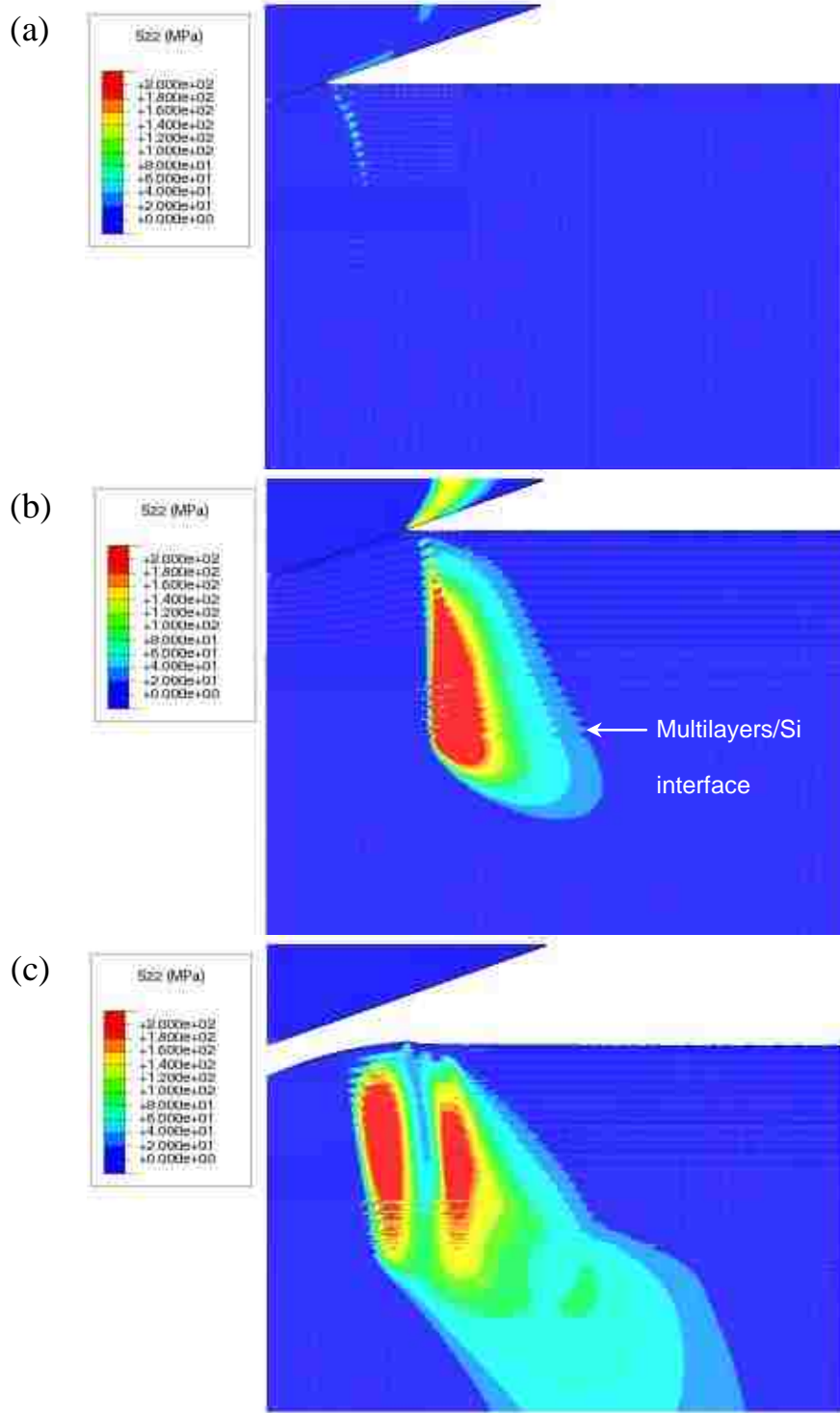


Figure 6.5 Contours of σ_{22} near the indentation site, when the indentation depth is at (a) 200 nm, (b) 500 nm, and (c) after unloading. The contour levels are adjusted to highlight the region with tensile stresses.

Figures 6.6(a), (b) and (c) show the contour plots of shear stress σ_{12} near the indentation contact, at depths of 200 nm, 500 nm during loading and after unloading from 500 nm, respectively. Local high shear stresses inside the several upper SiC layers can be observed. In Figure 6.6(b) a highly stressed region within the Si substrate is also evident. After unloading, the large shear stresses in the upper SiC layers changed sign and a reversed high shear state was developed (Figure 6.6(c)). The Al layers have also undergone significant variations in σ_{12} during unloading, although its relatively small values (compared to that in SiC) makes it less discernible in Figure 6.6 due to the chosen contour shading levels.

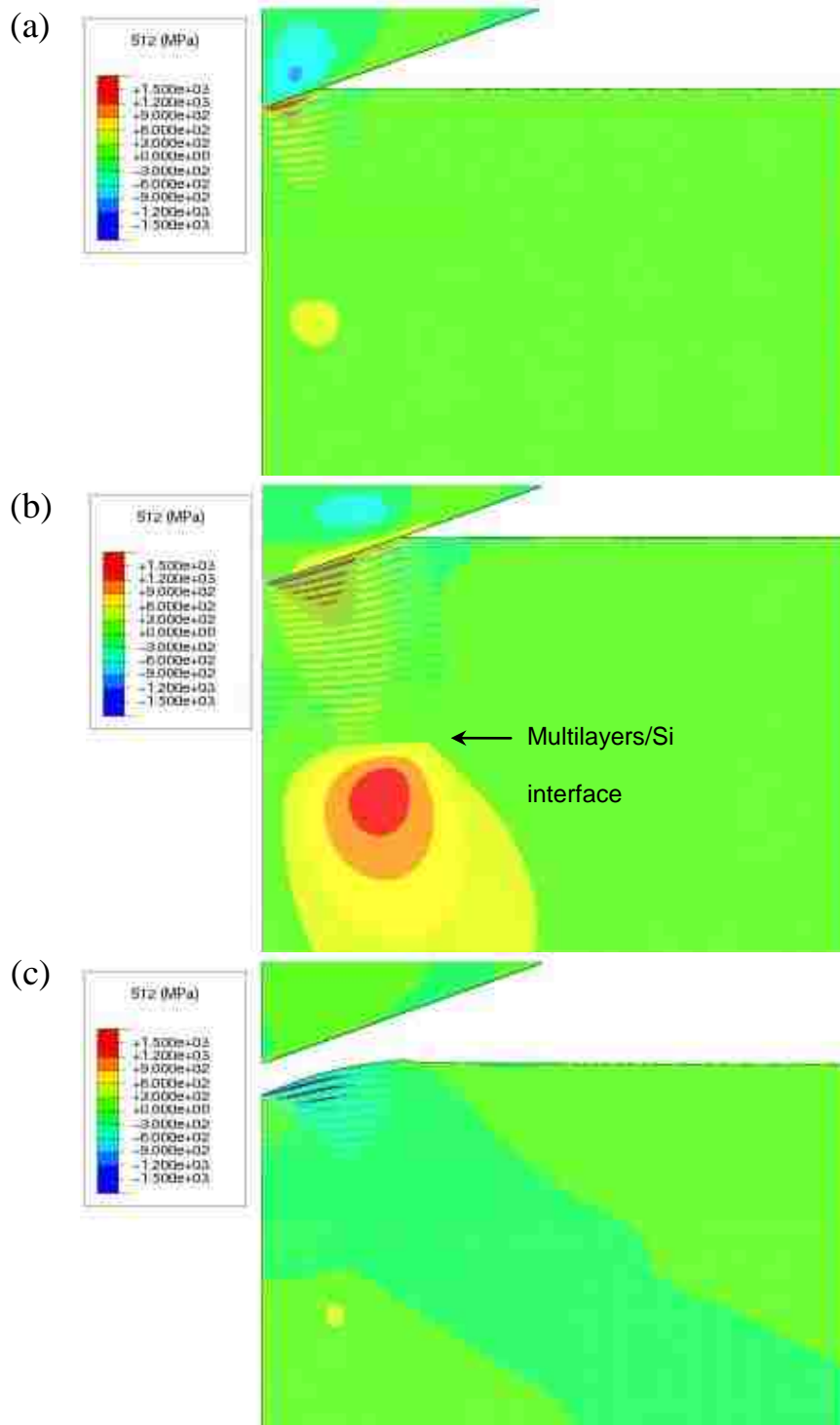


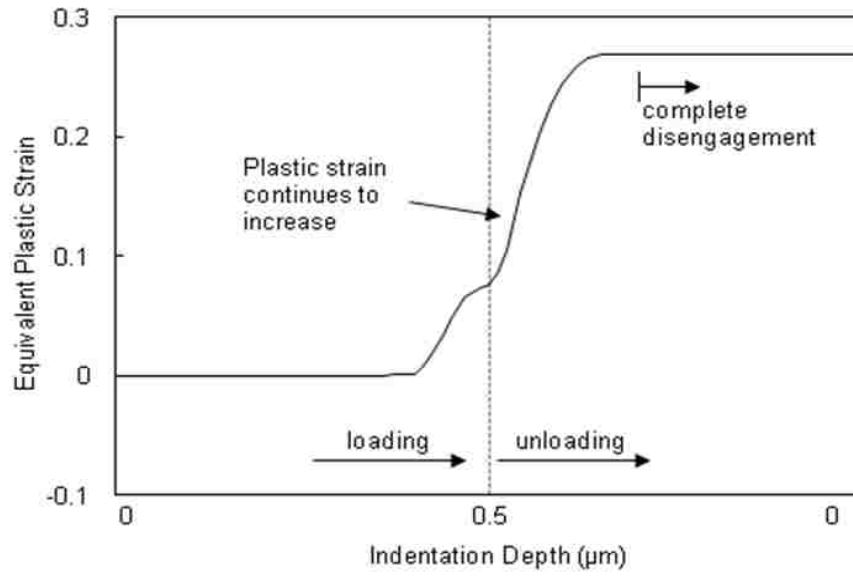
Figure 6.6 Contours of shear stress σ_{12} near the indentation site, when the indentation depth is at (a) 200 nm, (b) 500 nm, and (c) after unloading.

b) History of stress and strain

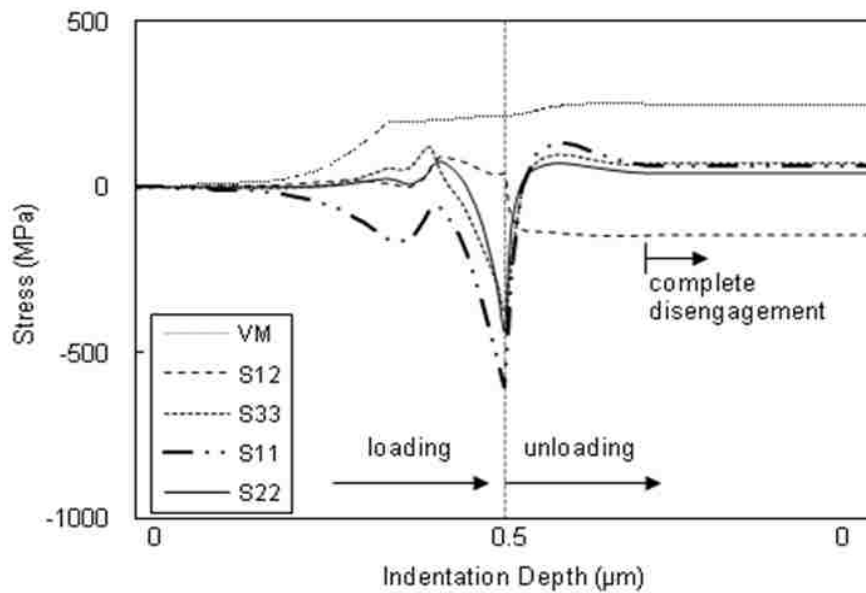
To better understand the unloading-induced plastic deformation described in the previous section (Figure 6.3), we selected a number of arbitrary material elements in the model and followed their deformation histories during loading and unloading. Here two such cases are presented. Figures 6.7(a) and (b) show the evolution of equivalent plastic strain and several stress components (von Mises effective stress, normal stresses σ_{11} , σ_{22} and σ_{33} , and shear stress σ_{12}), respectively, of an element inside the Al layer in a region highlighted by the circle on the right in Figure 6.3(b). The entire history of loading and unloading is included. In Figure 6.7(a), it can be seen that the equivalent plastic strain increases at the later stages of loading. The magnitude of plastic strain reaches about 0.08 when the indentation depth was at 0.5 μm . At the beginning of unloading, the equivalent plastic strain continues to increase and eventually attains a value of about 0.27. Note this is *not* the “reversed yielding” effect in typical cyclic loading because there is no elastic unloading part before the restart of plastic yielding. Here the plastic strain simply continues immediately upon load reversal. The plastic strain ceases to increase only after the indenter no longer makes contact with the surface.

In Figure 6.7(b), it can be seen that, toward the end of indentation loading, large magnitudes of compressive stresses σ_{11} , σ_{22} and σ_{33} have developed. The shear stress σ_{12} , on the other hand, remains relatively low. The von Mises effective stress stays relatively constant (it continues to increase slightly following the strain hardening response of the material). Upon unloading, the magnitude of the normal stress components decreases rapidly. However, the magnitude of the shear stress σ_{12} quickly becomes significant. The net effect is that the von

Mises effective stress remains at the yielding level so plastic deformation continues. The buildup of the shear stress during unloading may be attributed to the uneven elastic relief action of the adjacent SiC layers directly above and below.



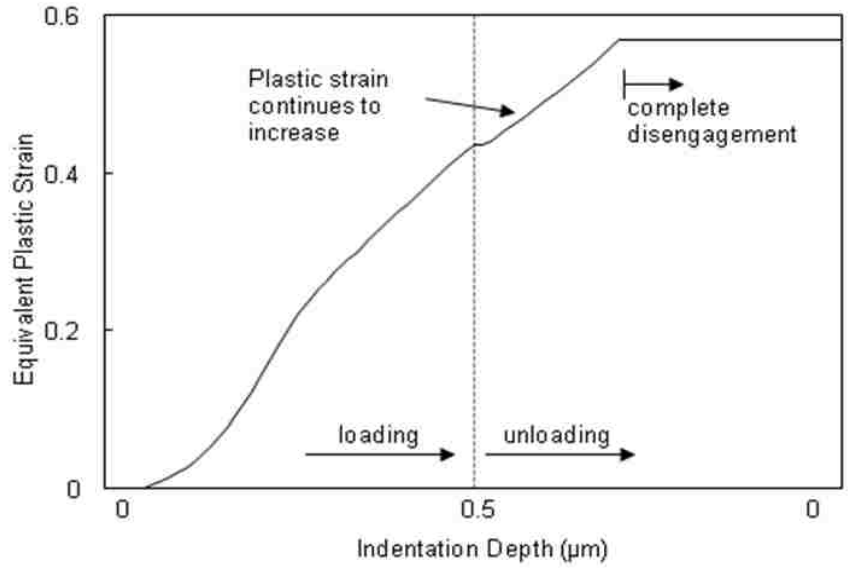
(a)



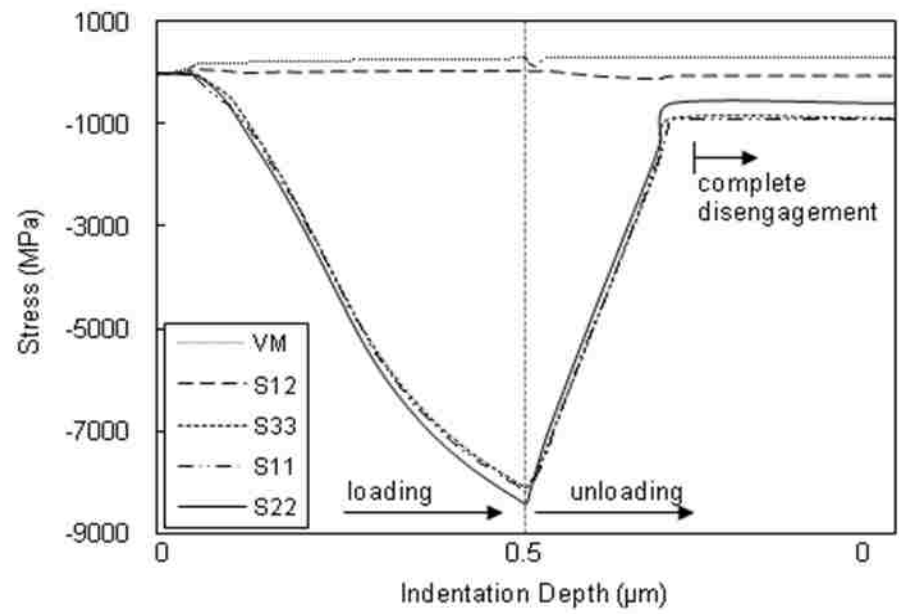
(b)

Figure 6.7 Evolution of (a) equivalent plastic strain and (b) several stress components of a material element, inside an Al layer in the region highlighted by the right circle in Figure 6.3 (b), during the indentation history. The symbols VM, S12, S33, S11 and S22 in (b) refer to the von Mises effective stress and the stress components σ_{12} , σ_{33} , σ_{11} and σ_{22} , respectively.

We now consider a second case, with the Al element in the region highlighted by the circle on the left in Figure 6.3(b). The evolution of equivalent plastic strain and several stress components (von Mises effective stress, normal stresses σ_{11} , σ_{22} and σ_{33} , and shear stress σ_{12}) in this element are shown in Figure 6.8. It can be seen that, compared to Figure 6.7, the buildup of plastic strain and stresses occurred earlier in the loading process because the material element in the present case is more directly underneath the indenter tip (rather than closer to the edge). At the end of the loading the magnitudes of equivalent plastic strain and normal stress components were also significantly greater. It is also noted that, toward the end of the loading process, the magnitude of σ_{22} exceeds those of σ_{11} and σ_{33} by 200-300 MPa (corresponding approximately to the flow strength of Al). The major qualitative difference between the cases in Figures 6.7 and 6.8 is that, in Figure 6.8(a), there is a brief pause in the increase in plastic strain at the beginning of the unloading process. This is also manifested by a temporary decrease in the von Mises effective stress shown in Figure 6.8(b). It is observed in Figure 6.8(b) that the development of the shear stress σ_{12} upon indentation unloading is not as sudden as in the case of Figure 6.7, and the difference between σ_{22} and the other normal stresses quickly diminishes. A reduction in the von Mises stress thus takes place. As a consequence, the material element experiences a brief elastic recovery at the onset of unloading. However, the yield condition soon re-establishes because the magnitude of σ_{22} falls below those of σ_{11} and σ_{33} , and the σ_{12} magnitude also gradually increases. The equivalent plastic strain continues to increase until the indentation contact is lost.



(a)



(b)

Figure 6.8 Evolution of (a) equivalent plastic strain and (b) several stress components of a material element, inside an Al layer in the region highlighted by the left circle in Figure 6.3 (b), during the indentation history. The symbols VM, S12, S33, S11 and S22 in (b) refer to the von Mises effective stress and the stress components σ_{12} , σ_{33} , σ_{11} and σ_{22} , respectively.

The above presentation has demonstrated an important feature: plastic yielding during unloading is associated with the buildup of shear stress and/or the rapid adjustment of relative quantities of the normal stress components. As mentioned above the nonuniform elastic relief of the SiC layers directly above and below may be the primary cause. It is worth mentioning that, when we tracked the deformation histories of material elements inside the much harder SiC layers, only elastic recovery during unloading was found (although SiC has also experienced plasticity during loading). The continuation of plastic deformation in Al during unloading is therefore a consequence of the internal mechanical constraint imposed by the hard ceramic layers. This finding does raise the issue about the accuracy of using instrumented indentation to quantify the elastic behavior of heterogeneous materials, because the unloading process is no longer a simple elastic event. This may contribute to the uncertainty of the elastic modulus results in Chapter 5.

c) Correlation with local damages

As shown in Fig 6.1 the positions of the cracks may now be correlated with the modeling result. In Figure 6.4(b) where the contour plot of maximum principal stress at the peak indentation is shown, large tensile stresses can be seen in a small region around the interface between the multilayers and Si substrate. This location coincides with the near-interface cracking observed in Figure 6.1. The large maximum principal stress was found to be a result of significant triaxial tension, with however the σ_{22} component being the most relevant because the crack orientation is perpendicular to the 2-axis. It can be seen that the general locations of both the mid-level and near-substrate cracks fall within the region with high

tensile σ_{22} stress shown in Figure 6.5(b). The stress value is well over 200 MPa. If the Al-SiC and Al-Si interfaces are sufficiently strong, cracking inside the Al layer is then prone to occur. One can also observe from Figures 6.5(b) and (c) that, the tension-stressed region expands during unloading, and even upon complete unloading high residual tension is still present. It is unclear if the internal failures in experiments took place during the loading or unloading phases of the indentation (once local failure occurs, the stress field will be altered significantly). Nevertheless, the numerical result in Figure 6.5 points to the interesting possibility that indentation-induced local damage may also be driven by the unloading process, if the layers have stayed intact during loading.

6.3 Conclusions

During indentation tests, local damages could happen within the specimen, such as void, cracking and delamination. Some of these behaviors could be explained by the stress field through modeling. Salient findings are summarized below.

1. The indentation stress field was seen to spread to the substrate material during the early stages of the loading process. After complete unloading, significant residual stresses remained in the composite structure due to the severe plastic deformation.
2. Under indentation loading, the magnitudes of compressive hydrostatic stress were much greater in the severely deformed Al layers than in the SiC layers, some parts of which carried large tensile stresses along the radial and transverse directions.
3. Significant tensile stresses along the vertical direction were found to exist below and slightly outside the indentation edge, despite the predominant compressive stresses directly

below the indentation contact. This vertical tensile stress field has actually expanded and the stress magnitudes remained high after unloading. The local tensile stress field can explain cracking in the mid-level Al layer and near the multilayers/substrate interface, observed experimentally in post-indented specimens.

4. During unloading, the equivalent plastic strain in the Al layers can continue to increase (either immediately upon unloading or after a very brief pause). Therefore the unloading process is not a simple recovery of elastic deformation as observed in single-phase homogeneous materials.

Chapter 7 Loading rate effects

In the previous chapters, all the numerical simulations are rate independent, as in the vast majority of numerical studies on indentation using the finite element method. In reality, however materials under indentation tend to display a certain degree of rate effect even at room temperature. As a consequence, during experiment a hold time at the peak load is frequently required so the material can reach a stable state. In this chapter we explore the effects of indentation loading rate and hold time using a viscoplasticity model for the metallic layer.

7.1 Model

Two models are employed to study the viscoplastic effect. One is a single Al film on a Si substrate; the other is Al/SiC multilayers on a Si substrate under indentation, as schematically shown in Fig 7.1. The thickness of single Al film is 2.05 μm with a Si substrate of 40.95 μm . The thickness of each Al or SiC layer is 50 nm with a Si substrate of 40.95 μm .

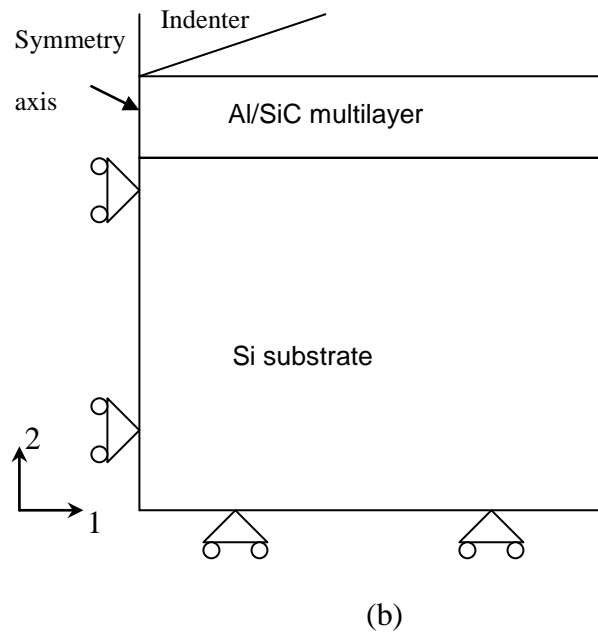
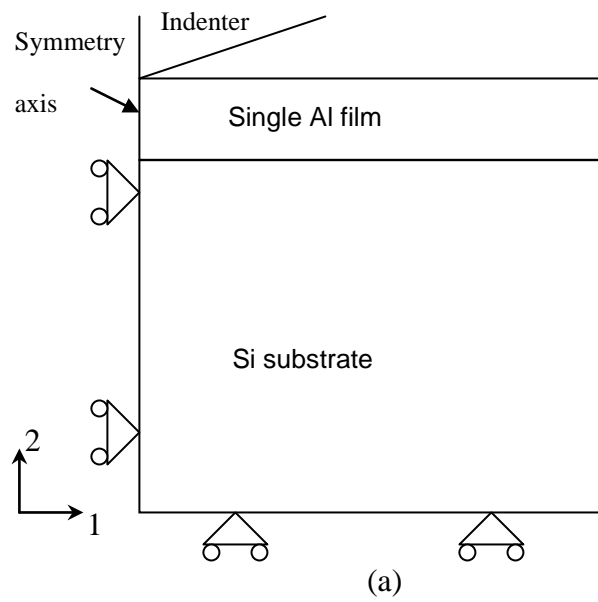


Figure 7.1: Schematics showing the two rate dependent models: (a) Single Al film above the Si substrate; (b) Al/SiC composite above the Si substrate.

The boundary conditions are the same as those in previous chapters. The properties of the materials are the same except for one difference, which is the rate dependent yielding of Al. The basic plastic yielding parameter is given for a “slow strain rate” behavior. The plastic flow stresses at other strain rates, higher than the “slow strain rate”, can be obtained from the basic plastic yielding information and the yield ratio R , which is given by

$$R = \sigma / \sigma^0 \quad (7.1)$$

where σ is the plastic flow stress at current strain rate and σ^0 is the flow stress for the “slow strain rate”. The true viscoplastic response of pure Al thin film is not available (it should also depend on the deposition condition, thermal history and microstructure). Therefore, we use the previous rate-independent plastic curve as the basis for the “slow strain rate” behavior. A strain rate of 10^{-6} is chosen to be the “slow strain rate” and the plastic flow stresses are given in Table 7.1. The strain-rate hardening response (yield ratio) is chosen to follow that of a bulk Al alloy 2024-T351 [89], which is provided in Table 7.2. In between the specified strain rates, interpolation is used. It is noted that we do not attempt to carry out a comprehensive study on the viscoplastic effect. Rather, we seek to gain some qualitative insight using the current modeling framework.

Table 7.1 Plastic property of Al at strain rate of 10^{-6}

Plastic strain	Plastic flow stress (MPa)
0	200
0.5	300
3	400

Table 7.2 Strain rate hardening

Strain rate	Yield ratio R
$1 * 10^{-6}$	1
$5 * 10^{-6}$	1.0305
$1 * 10^{-5}$	1.0436
$5 * 10^{-5}$	1.074
$1 * 10^{-4}$	1.0871
$5 * 10^{-4}$	1.1176
$1 * 10^{-3}$	1.1307
$5 * 10^{-3}$	1.1612
$1 * 10^{-2}$	1.1743
$5 * 10^{-2}$	1.2047
$1 * 10^{-1}$	1.2178
$5 * 10^{-1}$	1.2483

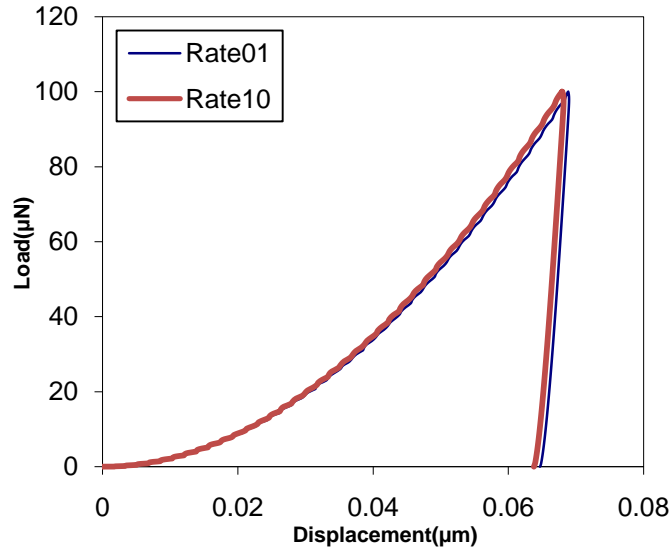
7.2 Numerical results

(a) Load-displacement curve of Al/Si model

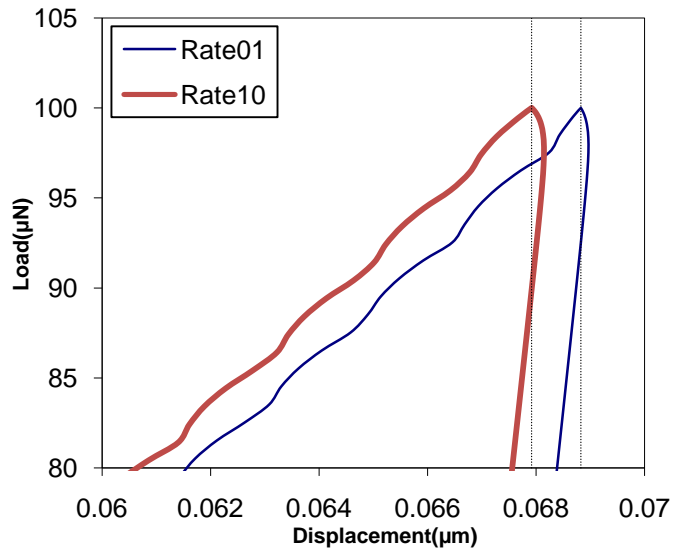
Figure 7.2 shows the indentation load-displacement curve of the Al film/Si substrate model with a maximum load of 100 μN with two different loading rates. The loading sequence is load –unload (without any holding time before unloading). The red curve shows the one with a loading rate 10 $\mu\text{N/s}$ and the blue of 1 $\mu\text{N/s}$. With the same peak load, the rate of 1 $\mu\text{N/s}$ results in a slightly larger displacement than the one with rate of 10 $\mu\text{N/s}$. From Figure 7.2 (b), at beginning of unloading, the displacement continues to increase when the load starts to drop due to the viscous material behavior. This leads to a “nose” shape at the onset of unloading. The curve with the higher loading rate (10 $\mu\text{N/s}$) shows a more pronounced nose compared to the case of 1 $\mu\text{N/s}$ loading rate meaning that the higher rate results in a less “settled” state at the peak load.

Figure 7.3 shows the load-displacement curve of the Al film/Si substrate model, with a maximum load of 100 μN with different loading rates. The loading sequence is load-hold-unload. The red curve shows the one with a loading rate 10 $\mu\text{N/s}$ and the blue curve of 1 $\mu\text{N/s}$. The holding time is 10 s in both cases. With the same peak load first reached, the one with rate of 1 $\mu\text{N/s}$ has a larger displacement than that of 10 $\mu\text{N/s}$. During holding, the displacements continue to increase for both cases. The fact that the displacement increases to approximately the same values for both models suggests that 10 s duration is sufficient for the Al to reach a stable state. At the beginning of unloading, the displacements start to drop with the load without forming a “nose” shape. Therefore, the experimental practice of including a

hold time before unloading is now validated numerically.



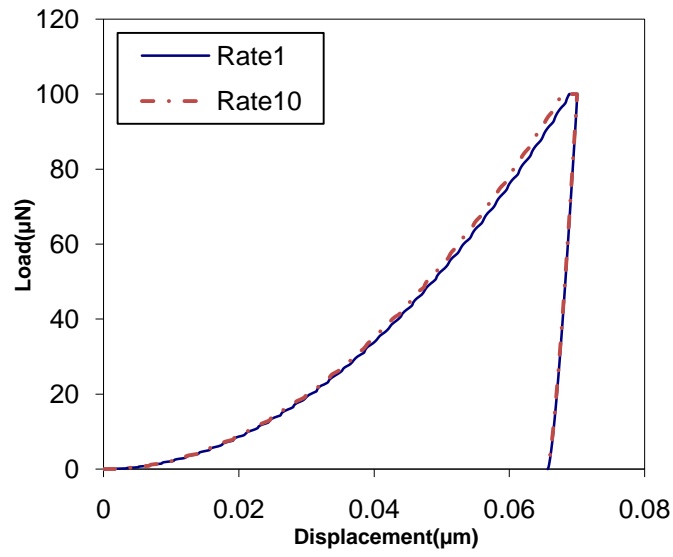
(a)



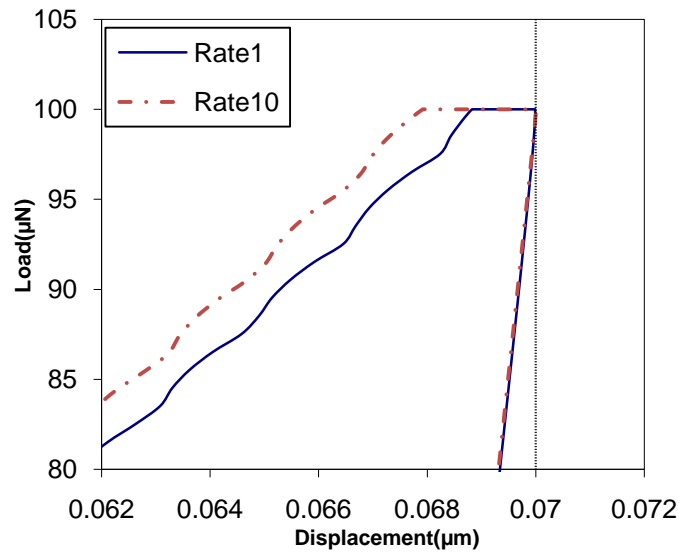
(b)

Figure 7.2: Load-displacement curves of the Al/Si model with loading rates of 10 μN/s and 1 μN/s (a)

Overall curve (b) Beginning part of the unloading curve.



(a)

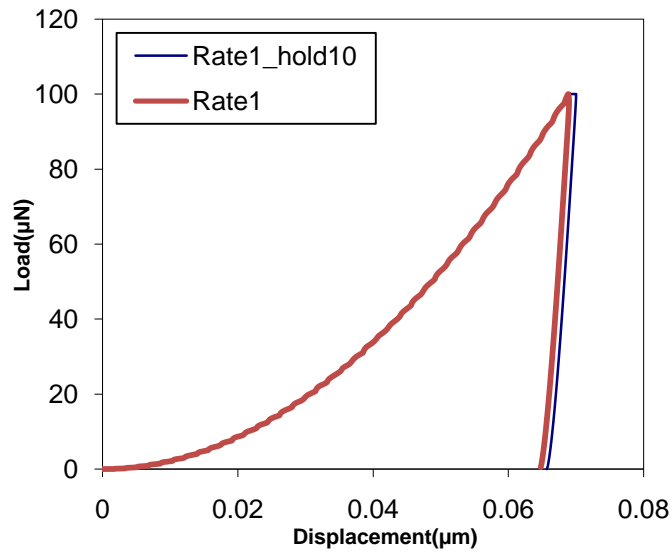


(b)

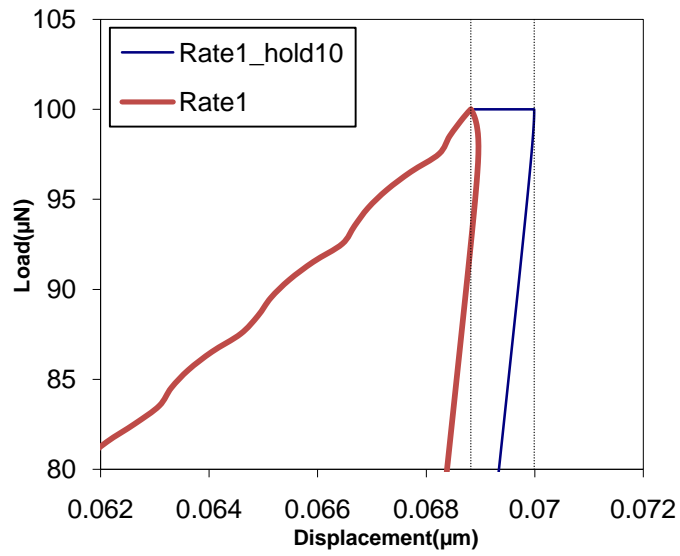
Figure 7.3: Load-displacement curves of the Al/Si model with loading rates of 10 $\mu\text{N/s}$ and 1 $\mu\text{N/s}$ with 10 s holding time(a) Overall curve (b) Beginning part of the unloading curve.

Figure 7.4 shows the load-displacement curves of the Al/Si model with a maximum load of 100 μN with a loading rate of 1 $\mu\text{N/s}$. The red curve shows the one with loading sequence of load-unload, while the blue curve shows the one with a loading sequence of load-hold-unload. In order to obtain the elastic modulus, the slope of the beginning part of the unloading is needed. With the rate-dependent behavior, it is seen that holding is necessary to give rise to a proper slope of the unloading curve if one uses the very beginning part of the unloading curve for the modulus calculation.

Figure 7.5 shows the load-displacement curves of the Al/Si model with a maximum load of 100 μN with a loading rate of 10 $\mu\text{N/s}$. The red curve shows the one with loading sequence of load-unload, while the blue curve show the one with a loading sequence of load-hold-unload. The same observations were made as in the case with a loading rate of 1 $\mu\text{N/s}$.

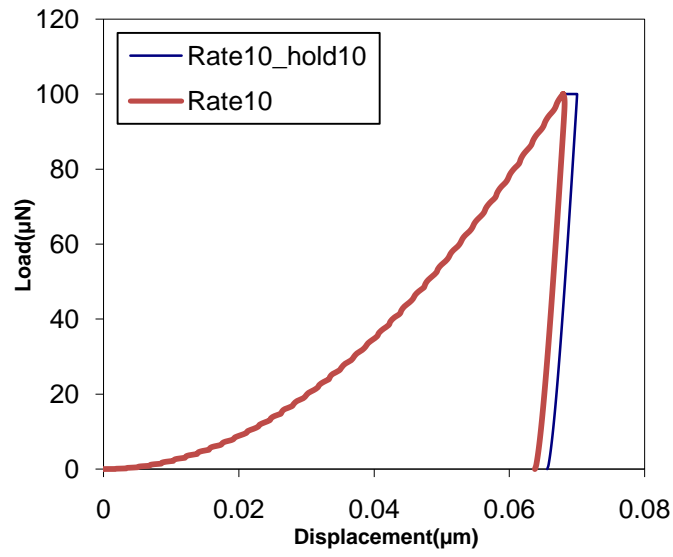


(a)

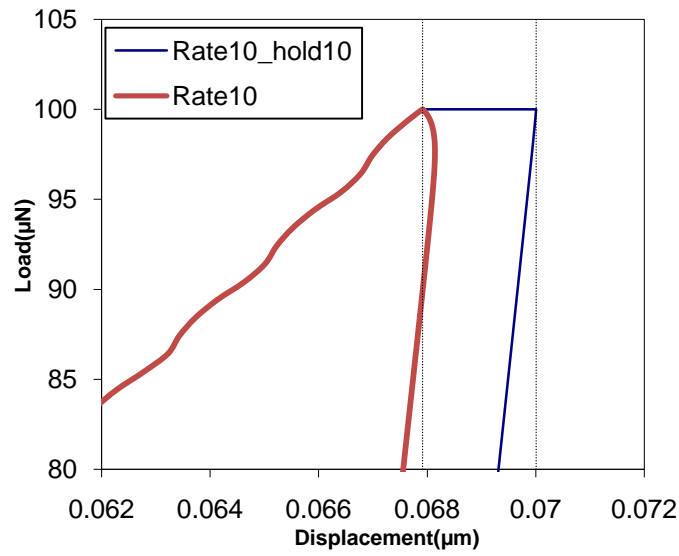


(b)

Figure 7.4: Load-displacement curves of the Al/Si model with loading rate of 1 $\mu\text{N/s}$ with no holding time and 10 s holding time (a) Overall curve (b) Beginning part of the unloading curve.



(a)



(b)

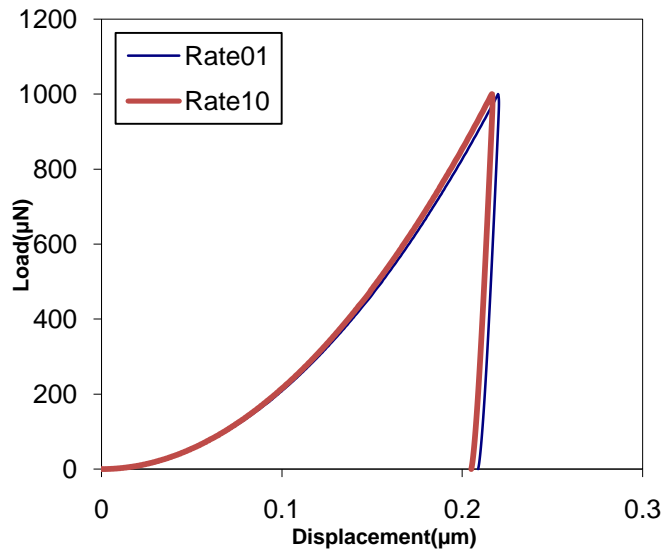
Figure 7.5: Load-displacement curves of the Al/Si model with loading rate of 10 $\mu\text{N/s}$ with no holding time and 10 s holding time (a) Overall curve (b) Beginning part of the unloading curve.

We now consider the cases with a higher peak load. Figure 7.6 shows the load-displacement curve of Al/Si model with a maximum load of 1000 μN with two different loading rates.

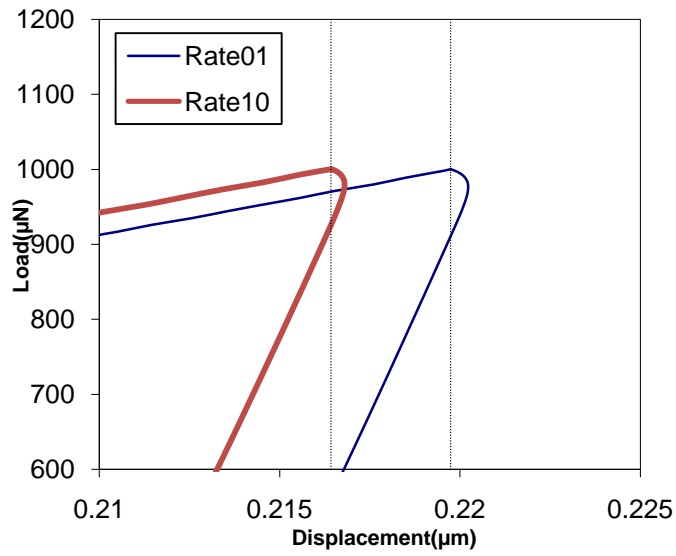
There is no holding time included here. The red curve shows the one with a loading rate 10 $\mu\text{N/s}$ and the blue curve of 1 $\mu\text{N/s}$. Very similar observations were made as the models with a maximum load of 100 μN in the previous section. With the same peak load of 1000 μN , the one with a rate of 1 $\mu\text{N/s}$ has a slightly larger displacement than the one with a rate of 10 $\mu\text{N/s}$. At the beginning of unloading, the displacements continue to increase when the loads start to drop due to the viscoplastic effect as seen in Figure 7.6 (b). The “nose” portion within the unloading curve has a similar size.

Figure 7.7 shows the load-displacement curve of the Al/Si model with a maximum load of 1000 μN with different loading rates. The loading sequence is load-hold-unload. The red curve shows the one with a loading rate 10 $\mu\text{N/s}$ and the blue curve of 1 $\mu\text{N/s}$. The holding time is 10 s in both cases. During holding, the displacements of the two models continue to increase, but to different values at the end of the 10 s duration. The maximum displacement of loading rate 1 $\mu\text{N/s}$ is still larger than the maximum displacement of loading rate 10 $\mu\text{N/s}$. This is different from the case with a peak load of 100 μN (Figure 7.3 (b)), which suggests that, at a higher peak load, a longer hold time is needed to reach a stable condition. From Figure 7.7 (b), at the beginning of unloading, the displacement with loading rate of 10 $\mu\text{N/s}$ starts to decrease with the load; while the displacement with loading rate of 1 $\mu\text{N/s}$ continues to increase first and then decreases. The holding time is not long enough in this case of a loading rate of 1 $\mu\text{N/s}$ to avoid the time dependent phenomenon during unloading. The main

implication of this analysis is that, during nanoindentation testing, the minimum hold time required to reach stabilization depends on the applied peak load and loading rate as well as on the detailed viscoplastic properties of the materials.



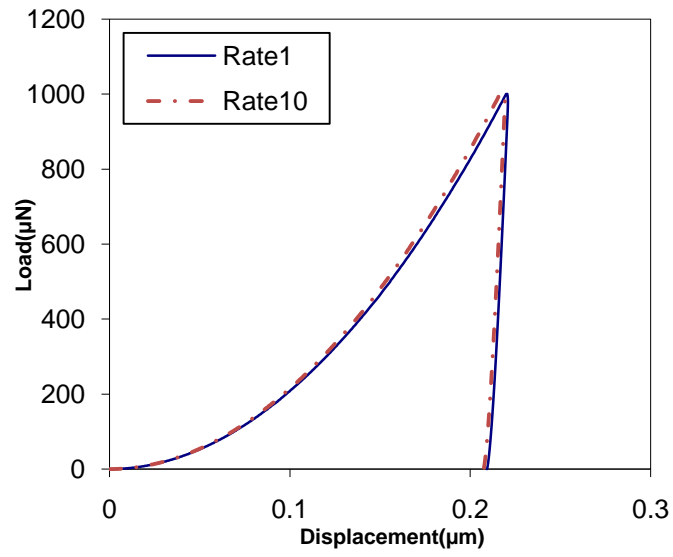
(a)



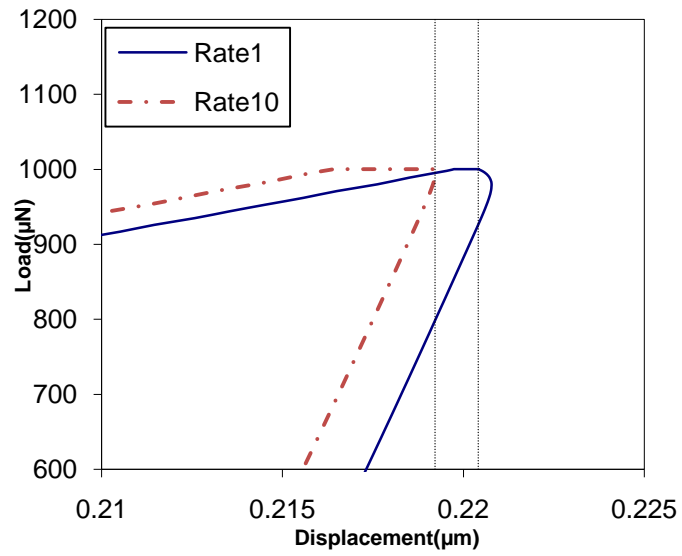
(b)

Figure 7.6: Load-displacement curves of Al on Si model with loading rates of 10 $\mu\text{N/s}$ and 1 $10 \mu\text{N/s}$ (a)

Overall curve (b) Beginning part of the unloading curve.



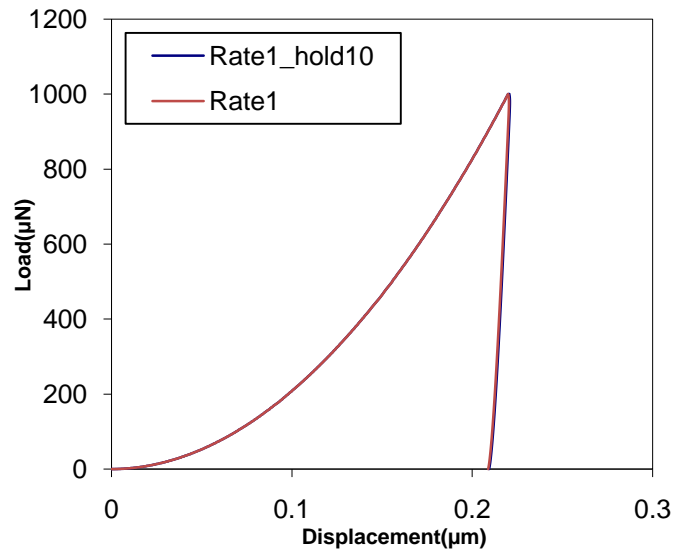
(a)



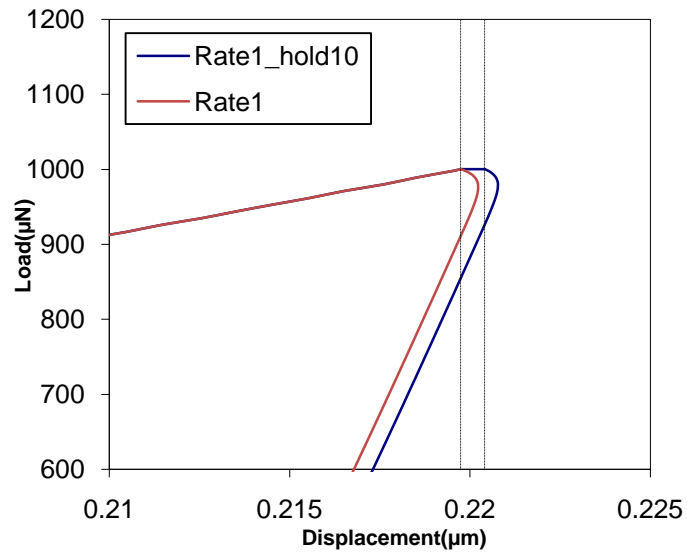
(b)

Figure 7.7: Load-displacement curves of Al on Si model with loading rates of 1 $\mu\text{N/s}$ and 10 $\mu\text{N/s}$ with 10 s holding time(a) Overall curve (b) Beginning part of the unloading curve.

Figure 7.8 shows the load-displacement curves for the case of a maximum load of 1000 μN with a loading rate of 1 $\mu\text{N/s}$. The corresponding plots for the loading rate of 10 $\mu\text{N/s}$ are shown in Figure 7.9. They were plotted to compare the holding and no holding results.

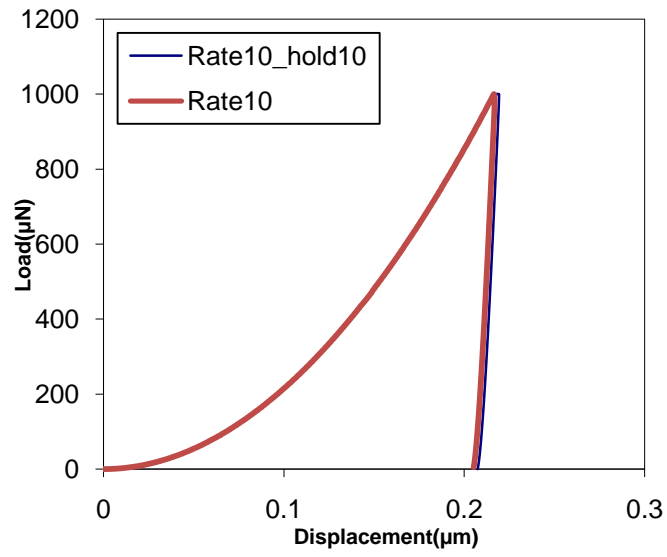


(a)

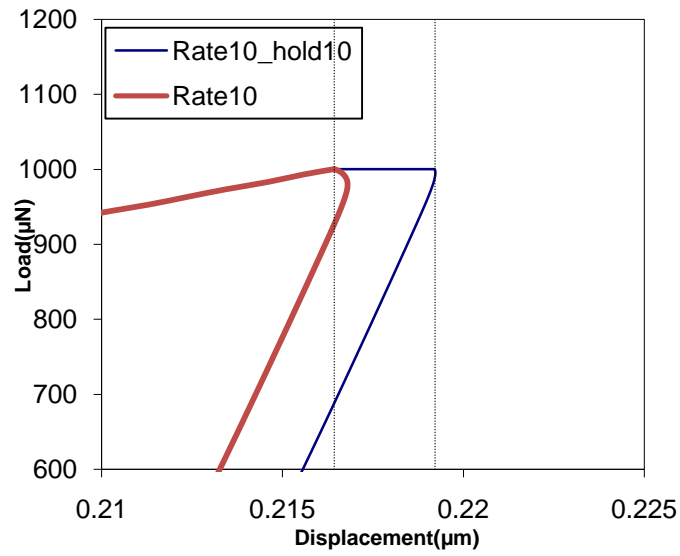


(b)

Figure 7.8: Load-displacement curves of Al on Si model with loading rate of 1 $\mu\text{N/s}$ with no holding time and 10 s holding time (a) Overall curve (b) Beginning part of the unloading curve.



(a)



(b)

Figure 7.9: Load-displacement curves of Al on Si model with loading rate of 10 $\mu\text{N/s}$ with no holding time and 10 s holding time (a) Overall curve (b) Beginning part of the unloading curve.

(b) Young's modulus and hardness of the Al/Si model

For all the cases presented above, we follow the same method in Chapter 5 to obtain the modulus and hardness of the Al film. The results are listed in Table 7.3 and 7.4. Note that in the cases with a “nose” at the beginning of unloading, the data in the “nose” part is ignored in the curve fitting procedure so a more accurate modulus value can be obtained. For a maximum load of 100 μN , the modulus values are around 62 GPa, which is slightly higher than the input value of 59 GPa. For a maximum load of 1000 μN , the modulus values are around 72 GPa, which is no doubt affected by the Si substrate. The loading rate does not seem to play a significant role. In addition, although the hold time results in a “better shape” of the unloading curve, it does not necessarily generate a modulus value closer to the model input.

Table 7.3 Modulus of the Al/Si model

		No holding (GPa)	10 s holding time (GPa)
Peak load=100 μN	Rate=1 $\mu\text{N/s}$	62.2	63.2
	Rate=10 $\mu\text{N/s}$	62.5	60.4
Peak load=1000 μN	Rate=1 $\mu\text{N/s}$	71.9	72.3
	Rate=10 $\mu\text{N/s}$	72.2	73.3

For a maximum load of 100 μN , the hardness values in the no hold cases are much higher than the values in the cases with hold (Table 7.4). This is apparently due to the continuous

increase in contact area during the 10 s hold. For a maximum load of 1000 μN , the hardness values are less affected by the hold. The relatively constant values in the right-most column in Table 7.4 suggest the importance of employing a hold duration when performing nanoindentation tests to measure the hardness.

Table 7.4 Hardness of the Al/Si model

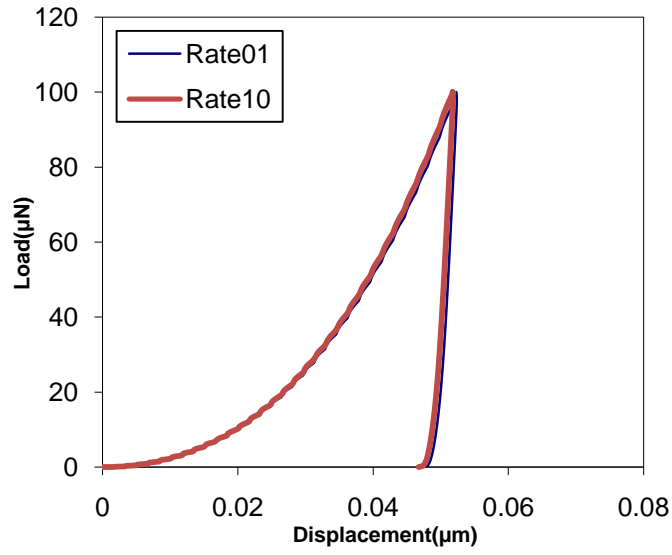
		No holding (MPa)	10 s holding time (MPa)
Peak load=100 μN	Rate=1 $\mu\text{N/s}$	772.0	734.6
	Rate=10 $\mu\text{N/s}$	812.5	735.3
Peak load=1000 μN	Rate=1 $\mu\text{N/s}$	737.5	736.8
	Rate=10 $\mu\text{N/s}$	763.0	749.3

(c) Load-displacement curve of the Multilayer/Si model

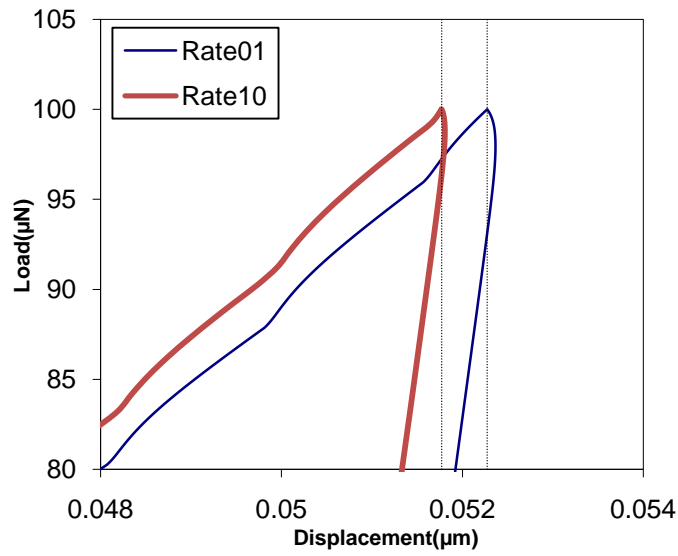
Attention is now turned to the model with 41 layers of Al/SiC on a Si substrate. Figure 7.10 shows the load-displacement curve with a maximum load of 100 μN with two different loading rates. The loading sequence is load –unload with no holding time. The red curve shows the one with a loading rate 10 $\mu\text{N/s}$ and the blue curve of 1 $\mu\text{N/s}$. The corresponding plots for the cases with a 10 s hold time are shown in Figure 7.11.

Figure 7.12 shows the load-displacement curves with a maximum load of 100 μN with a loading rate of 1 $\mu\text{N/s}$. The red curve shows the one with the loading sequence of load-

unload; while the blue curve shows the one with the loading sequence of load-hold-unload. For comparison the corresponding plots for the cases of loading rate of $10 \mu\text{N/s}$ are shown in Figure 7.13. In all these figures, the curves behave in a qualitatively similar way as the Al film/Si model. However, the time-dependent effects appear to be less significant for multilayers.

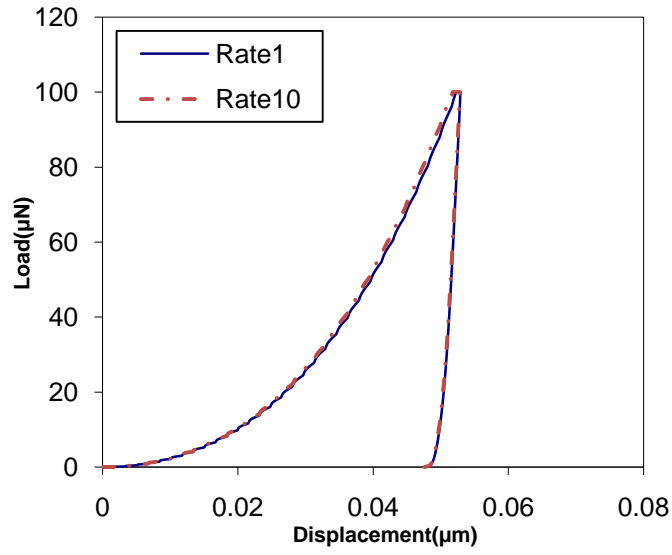


(a)

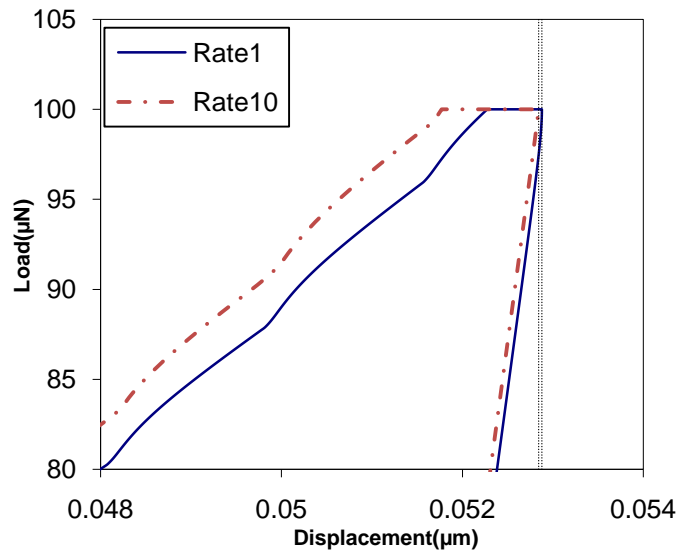


(b)

Figure 7.10: Load-displacement curves of 41-layer Al/SiC on Si model with loading rates of 10 $\mu\text{N/s}$ and 1 $\mu\text{N/s}$ (a) Overall curve (b) Beginning part of the unloading curve.

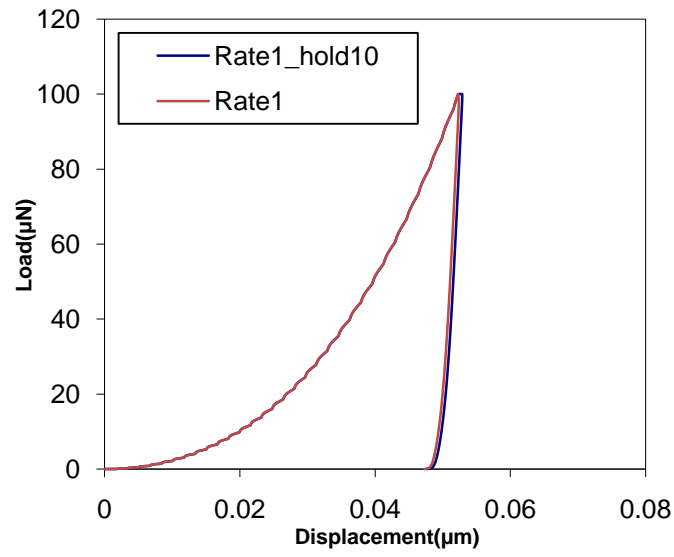


(a)

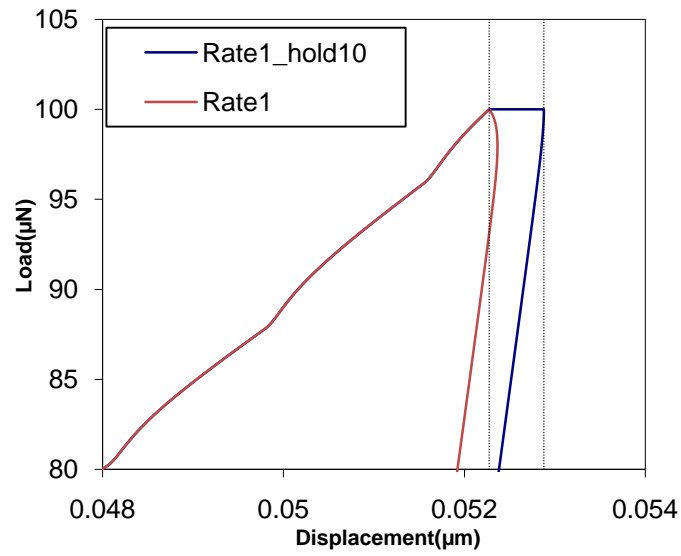


(b)

Figure 7.11: Load-displacement curves of 41-layer Al/SiC on Si model with loading rates of 10 $\mu\text{N/s}$ and 1 $\mu\text{N/s}$ with 10 s holding time (a) Overall curve (b) Beginning part of the unloading curve.

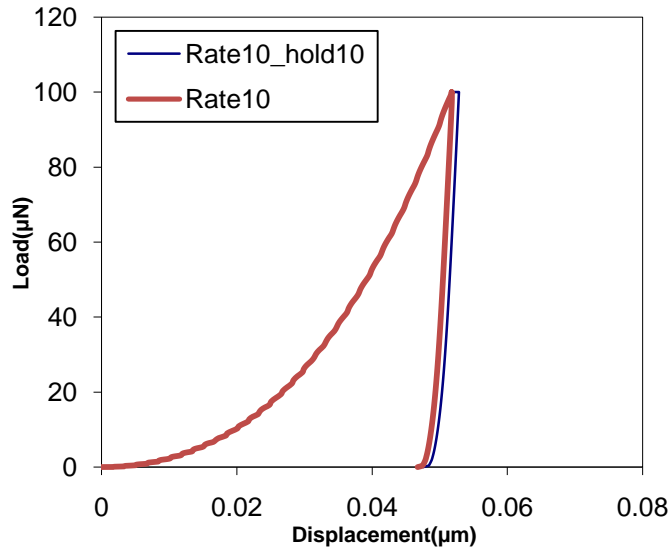


(a)

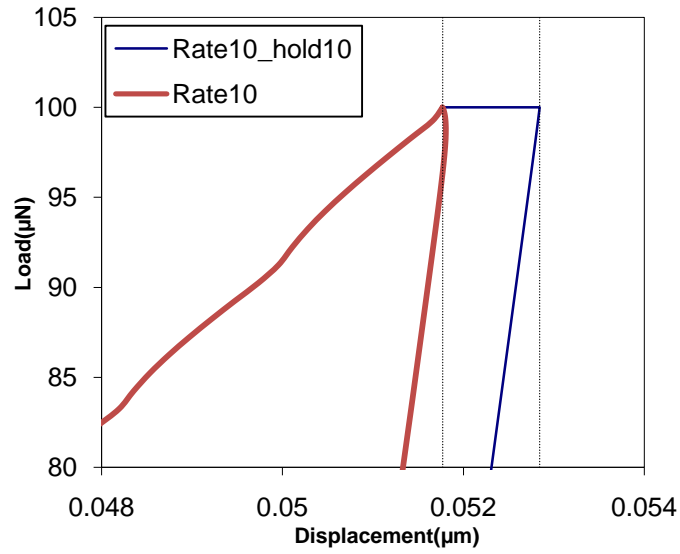


(b)

Figure 7.12: Load-displacement curves of 41-layer Al/SiC on Si model with loading rate of 1 $\mu\text{N/s}$ with no holding time and 10 s holding time (a) Overall curve (b) Beginning part of the unloading curve.



(a)



(b)

Figure 7.13: Load-displacement curves of 41-layer Al/SiC on Si model with loading rate of 10 $\mu\text{N/s}$ with no holding time and 10 s holding time (a) Overall curve (b) Beginning part of the unloading curve.

(d) Young's modulus and hardness of the multilayer/Si model

The modulus and hardness values are calculated and listed in Table 7.5 and 7.6.

For a maximum load of 100 μN , the modulus values are around 104 GPa, which is a little lower than the true composite modulus value of 117 GPa. However, since the maximum indentation depth considered here is only slightly over one initial layer thickness, a lower modulus value is to be expected.

Table 7.5 Modulus of 41 layer Al/SiC on Si

		No holding (GPa)	10 s holding time (GPa)
Peak load=100 μN	Rate=1 $\mu\text{N/s}$	105.1	105.1
	Rate=10 $\mu\text{N/s}$	103.4	103.0

In Table 7.6, the hardness values in the no hold cases are slightly higher than the values in the cases with a 10 s hold. The hold time appears to lead to a more reliable result (apparently the same hardness values for different loading rates), although the influence by the hold is much smaller compared to the case of a single Al film.

Table 7.6 Hardness of 41 layer Al/SiC on Si

		No holding (MPa)	10 s holding time (MPa)
Peak load=100 μ N	Rate=1 μ N/s	1085.7	1075.7
	Rate=10 μ N/s	1096.0	1077.5

7.3 Conclusions

With the simulation framework considered in this chapter, we conclude that the viscoplastic behavior of the material can affect its indentation response. The inclusion of a hold time at the peak load can help stabilize the indentation load-displacement curve. The hardness obtained after the hold is more reliable; the elastic modulus, on the other hand, does not seem to be affected much. The required minimum hold time is sensitive to the actual peak load used in the indentation. Within the load rate range of 1-10 μ N/s, the loading rate itself plays only a small role in affecting the indentation result. Compared to the case of a single Al film, the Al/SiC multilayers display a less significant time-dependent behavior during indentation.

Chapter 8 Microcompression of pillars

In conjunction with the experimental effort by our collaborators in Arizona State University, we also performed finite element modeling on the microcompression loading of Al/SiC multilayer pillars. As introduced in Chapter 2, this is a special form of “indentation” test, where a flat-bottom indenter is used to press onto a rod-like specimen prepared by FIB-milling, shown schematically in Figure 8.1.

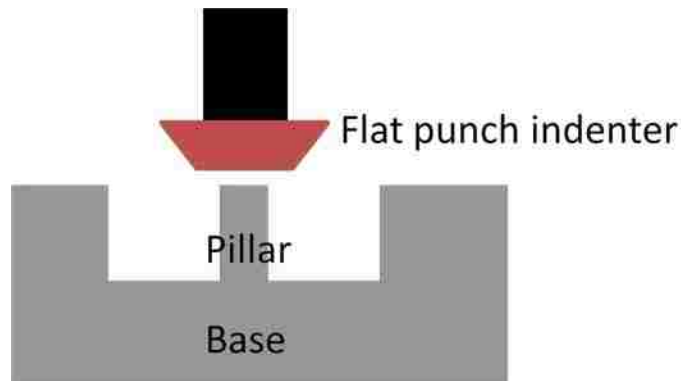


Figure 8.1: Schematics showing microcompression on a pillar with base.

8.1 Numerical simulation of Si pillar

Two dimensional axisymmetric models were constructed for the analysis. Figure 8.2 (a) and (b) show the models of a stand-alone pillar and a pillar connected to a base, respectively. Note in reality that there is always a deformable base (the substrate), so Figure 8.2 (a) represents an idealized configuration. One important issue is that the base always absorbs some deformation during loading, so it is essential to numerically quantify the deformation

experienced by the pillar itself. The geometry of the model is defined by the pillar height h , pillar cross section radius r (or cross section diameter d), base height H and base width W . The aspect ratio of the pillar is defined as the ratio of pillar height over pillar cross section diameter (h/d).

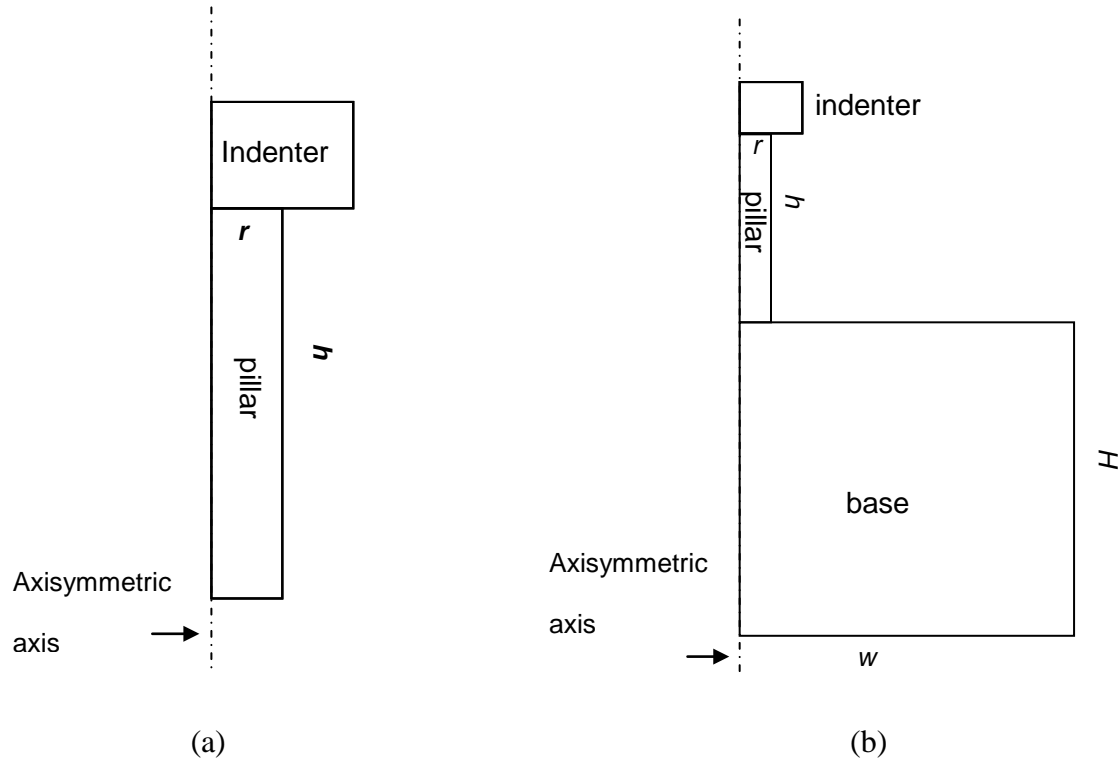


Figure 8.2: Schematics showing the two pillar model: (a) Single pillar under microcompression; (b) Pillar with base under microcompression

(a) Base height effect of Si pillar model

To gain a basic understanding of pillar deformation, we first consider a reference case of Si pillar and Si base. Two models with different pillar aspect ratios are considered. Model I was

constructed with the following dimensions: pillar height $h=3\mu\text{m}$, cross section diameter $d=2\mu\text{m}$, and a resulting aspect ratio of 1.5. Model II was constructed with the following dimensions: pillar height $h=6\mu\text{m}$, cross section diameter $d=2\mu\text{m}$, and a resulting aspect ratio of 3. For each model, the following four cases with different base heights were first studied: i) $W=500\mu\text{m}$, $H=500\mu\text{m}$, ii) $W=500\mu\text{m}$, $H=50\mu\text{m}$, iii) $W=500\mu\text{m}$, $H=5\mu\text{m}$, iv) no base. The input elastic modulus is 187 GPa and the Poisson ratio is 0.28. Compression tests were carried out, with the coefficient of friction between the diamond indenter and the pillar top being indented on to be 0.1. The apparent Young's modulus is obtained from the slope of stress-strain curve as shown in Figure 8.3.

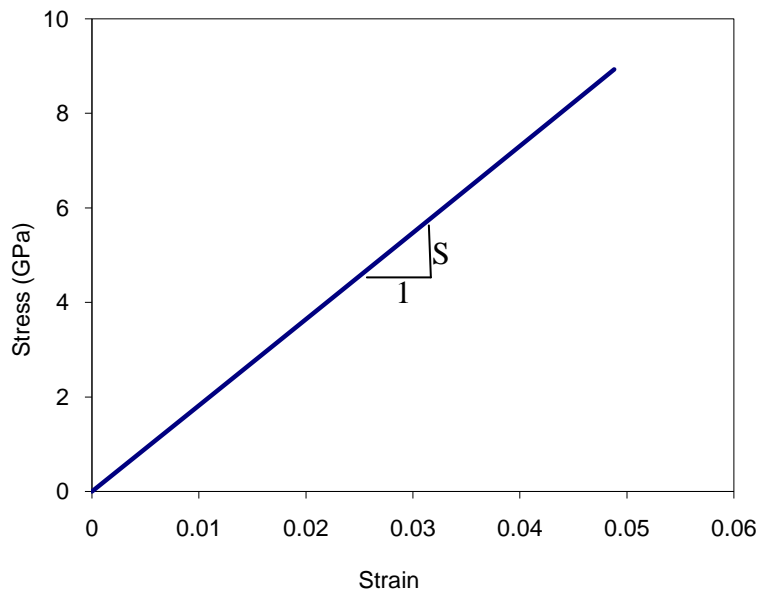


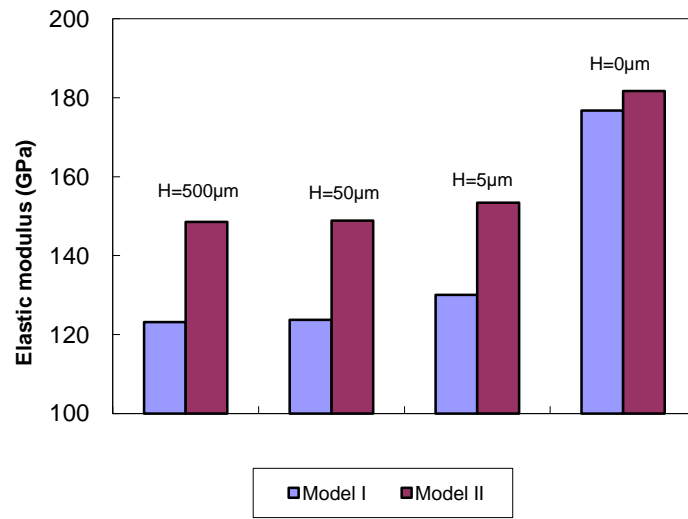
Figure 8.3 Representative stress-strain curve of microcompression simulation on Si

All the modulus values are given in Table 8.1. The data are also plotted in Figure 8.4. The apparent modulus of Si, in the Si pillar model with no base, is close to the input value of Si.

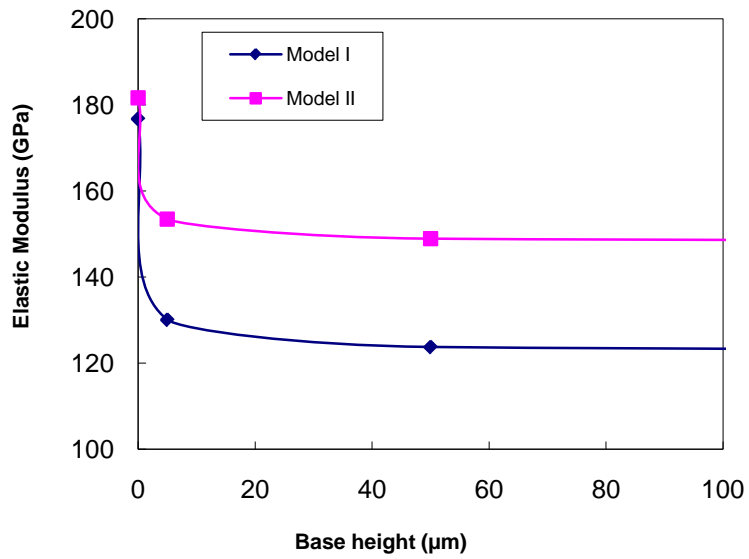
The apparent modulus of Si, in the Si pillar model with a base, is lower. The elastic modulus is closer to the input value when the base is thinner; it is much lower than the input value when the base is thicker. The modulus values is affected by the thickness of the base.

Table 8.1 Young's modulus of Si pillar with a base width of 500 μm .

Base height (μm)	Model I (GPa) Aspect ratio=1.5	Model II (GPa) Aspect ratio=3
0	176.8	181.7
5	130.1	153.4
50	123.7	148.9
500	123.1	148.5



(a)



(b)

Figure 8.4: a) Simulated modulus values of Si pillar with different base heights and aspect ratios. b) The same data presented in a different graphical form.

(b) Base width effect of the Si pillar model

The effect of base width under a fixed base height is now examined. Model I and Model II are still used for denoting the two pillar aspect ratios: 1.5 and 3, respectively. For each model, the following four cases with different base geometries were studied: i) $W=500\mu\text{m}$, $H=500\mu\text{m}$, ii) $W=50\mu\text{m}$, $H=500\mu\text{m}$, iii) $W=5\mu\text{m}$, $H=500\mu\text{m}$, iv) no base. The input properties of the Si and the friction between the diamond indenter and the pillar top are the same as those in section (a). The simulated modulus values are given in table 8.2 and plotted in Figure 8.5. The calculated elastic modulus is closer to the input value when the base is wider; it decreases dramatically with the width of the base. Therefore, it is necessary to have a wider base in order to get a more accurate stress-strain behavior for the pillar.

Table 8.2 Young's modulus of Si pillar with a base height of 500 μm

Base width (μm)	Model I (GPa) Aspect ratio=1.5	Model II (GPa) Aspect ratio=3
0	176.8	181.7
5	23.2	41.3
50	118.8	145.3
500	123.1	148.5

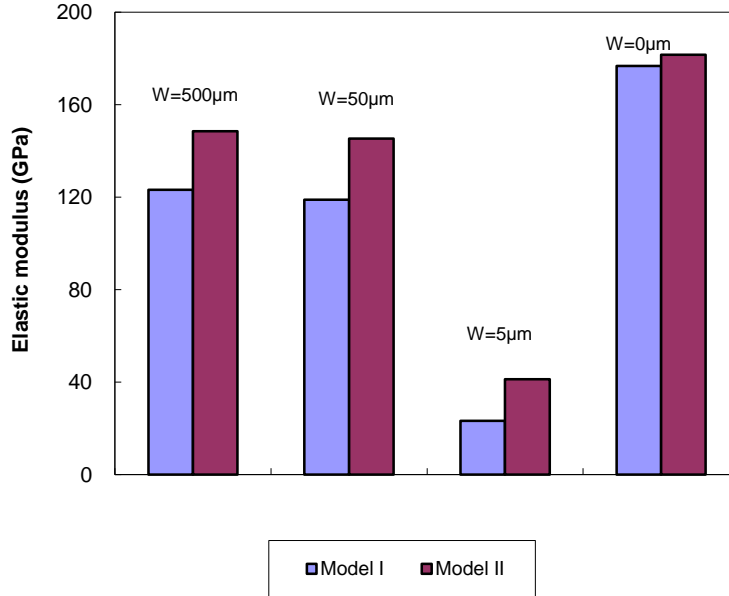


Figure 8.5: Simulated modulus of Si pillar with different base widths and aspect ratios.

(c) Friction and fillets

We also investigated the effects of the contact friction and the possible fillets at the corner of the pillar bottom and the base. For the previous simulations the friction between the diamond indenter and the pillar top is set to be 0.1. We construct a free sliding (coefficient of friction to be zero) model with the following geometry: pillar height $h=3\mu\text{m}$, cross section diameter $d=2\mu\text{m}$, and a resulting aspect ratio of 1.5 with no base. The apparent modulus of Si is found to be 175.4 GPa, close to 176.8 GPa (modulus of the same model with a coefficient of friction of 0.1) given in Table 8.1. Therefore the friction has no significant effects on the modulus values obtained from the compression tests.

There are no fillets considered in the previous models. We now include fillet , which has a radius of $0.2\ \mu\text{m}$, between the pillar and the base. The following geometry is used: pillar height $h=3\ \mu\text{m}$, cross section diameter $d=2\ \mu\text{m}$, and a resulting aspect ratio of 1.5 with base height and width both to be $500\ \mu\text{m}$. The apparent modulus is found to be $126.0\ \text{GPa}$, slightly higher, but close to $123.0\ \text{GPa}$ (modulus of the same model without a fillet) given in Table 8.1. There does not seem to be any significant effects if the fillet radius is kept sufficiently small.

8.2 Numerical simulation of the Al/SiC pillar

(a) Elastic modulus of the multilayer composite pillar

We now consider pillars made of Al/SiC multilayers. Figure 8.6 shows the schematics of a 41-layer Al/SiC pillar on Si base. The compression axis is perpendicular to the layer directions.

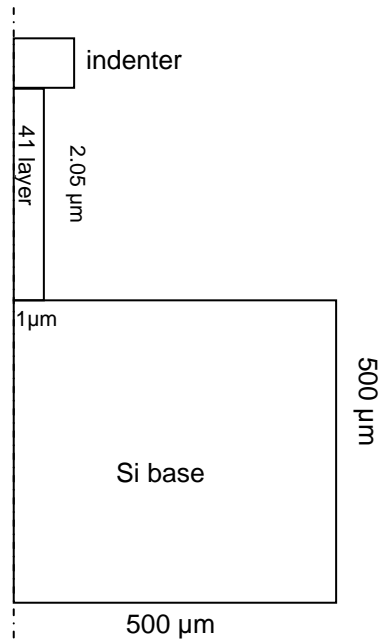


Figure 8.6: Schematics showing the Al/SiC multilayer pillar on a Si base

The stress-strain curve and apparent Young's modulus can be directly obtained from the finite element analysis. Table 8.3 lists the simulated Young's modulus for the model. The apparent modulus is 77 GPa, much below the true modulus value for the Al/SiC multilayers of 117 GPa, which was obtained in Chapter 4. This is attributed to the compliance of the Si base and diamond indenter. The corrected pillar modulus can be obtained by subtracting the axial strains of the indenter and/or base from the total axial strain. The results are also shown in Table 8.3. It can be seen that the contribution of the Si base is very significant and that of the indenter is moderate. When the compliances of both are accounted for, the true Al/SiC composite modulus of 117 GPa can be recovered. This finding suggests the importance of correcting the raw data by accounting for the base and "machine" deformation when conducting experimental studies.

Table 8.3 Young's modulus of the multilayer pillar (Figure 8.6)

	Modulus (GPa)
FEM-direct	77.2
FEM-diamond compliance correction	80.7
FEM-Si compliance correction	110.0
FEM-diamond & Si compliance correction	117.3
True E_{22} of Al ₁₅ SiC ₅₀ composite	117

We now focus on the stress-strain curves when the deformation is sufficiently large to cause significant plastic yielding. During deformation, the cross section area changes in a non-uniform manner. Here we use the cross section area in the middle of the pillar for calculating the stress. The stress-strain curve of the pillar structure, together with the stress-strain curve of the true composite, are plotted in Figure 8.7. The stress-strain curve of the true composite is plotted using the data from the model of uniaxial loading discussed in Chapter 4. The stress-strain curve of multilayer pillar is significantly below the curve of the true composite. One reason could be the compliance of the indenter and the base. At the nominal strain, the actual strain of the pillar itself is smaller than the nominal strain, so the stress is much lower than the stress of the true composite. Another reason could be the extrusion of the Al layer under compression which will be discussed in section (c).

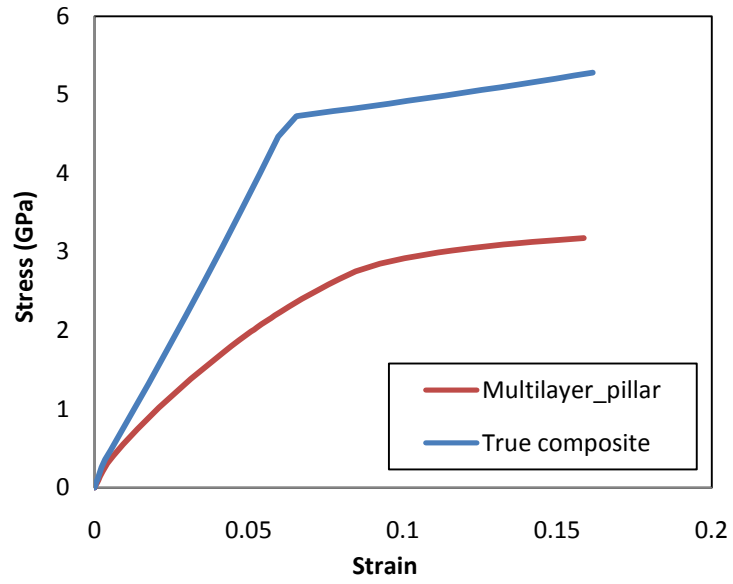


Figure 8.7: Stress strain curves of multilayer pillar model and true composite.

(b) Elastic modulus of the multilayer composite pillar with taper

In experiments, the pillar is produced by FIB milling. It is difficult to achieve a true vertical side wall from the process, so there is always an angle as schematically shown in Figure 8.8.

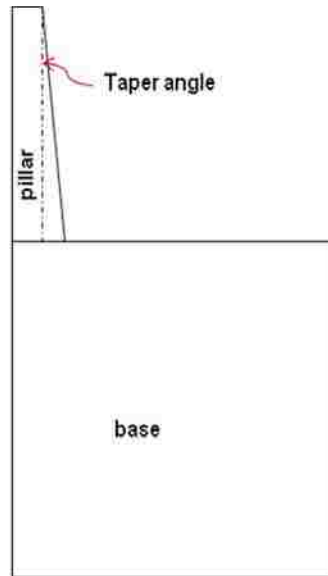


Figure 8.8: Schematics showing the pillar model with taper

To examine how this imperfect geometry may influence the test result, we constructed one set of models of the 41-layer pillar on a Si base with different taper angles of 1° , 2° and 4° . For comparison purposes, we also constructed another set of models of pure Al pillar on an Al base, with the same taper angles of 1° , 2° and 4° .

For each model, we have conducted the compression simulation with a displacement up to $0.3 \mu\text{m}$. The stress-strain curves of each model, together with the one with no taper, are plotted in Figure 8.9. When the strain is relatively small, all the curves are very close to one another. When the strain is large enough, the curves with taper are all below the curve of the non-tapered model. The difference increases with an increasing taper angle. For practical purpose, the effect may be ignored if the taper angle is within $1\text{-}2^\circ$.

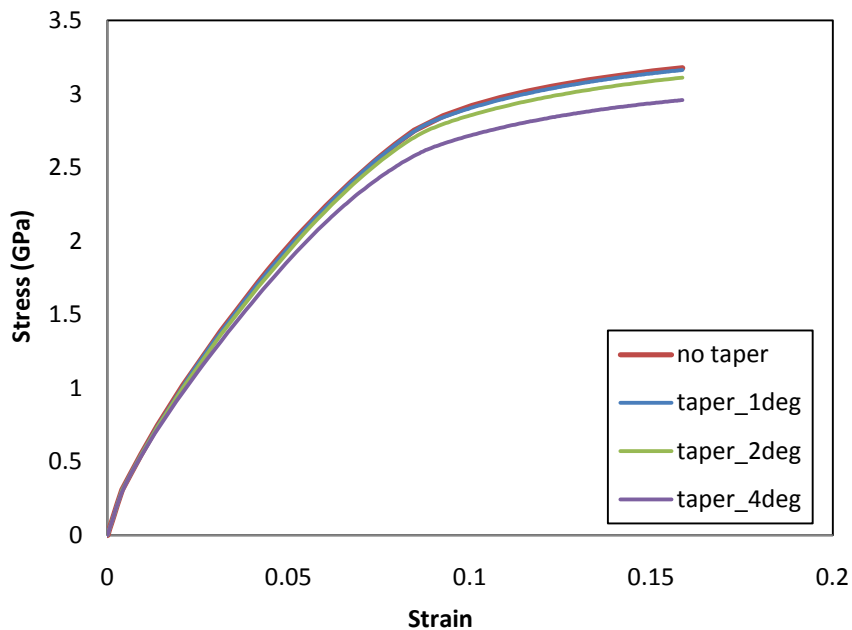


Figure 8.9: Stress strain curves of multilayer pillar with taper angle of 1°, 2° and 4°

The Young's modulus of all the multilayer pillar models with different taper angles are calculated and listed in Table 8.4. The values in the left column are those obtained directly from finite element analysis, while the ones in the right column are the ones with the compliance correction of diamond and Si following the same approach as in the previous section. One can see that the taper does not have any significant effect on the modulus values.

Table 8.4 Young's modulus of multilayer pillar with taper

	FEM-direct (GPa)	FEM-diamond & Si compliance correction (GPa)
No taper	77.2	117.0
1°	77.0	115.6
2°	76.8	115.4
4°	76.1	114.7

(c) Stress and deformation evolutions

Before examining the stress evolution of the multilayer pillar model, we first present the simulation results on the pure Al pillar with an Al base. Figure 8.10 (a) and (b) shows the equivalent plastic strain contours of the pure Al pillar with no taper, at the compression displacement of 100 nm and 325 nm respectively. Figure 8.11 (a) and (b) shows the equivalent plastic strain contours of the pure Al pillar with a 2 ° taper angle at 100 nm and 325 nm compression depths, respectively. The deformations for the tapered and non-tapered model are quite similar, with the deformation of the tapered model being a little stronger.

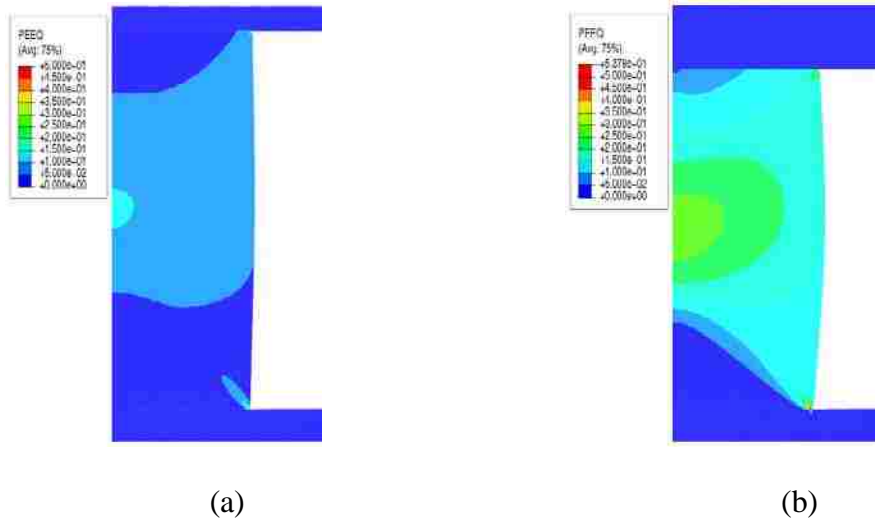


Figure 8.10: Equivalent plastic strain of the pure Al pillar at compression depths of (a) 100 nm and (b) 325 nm.

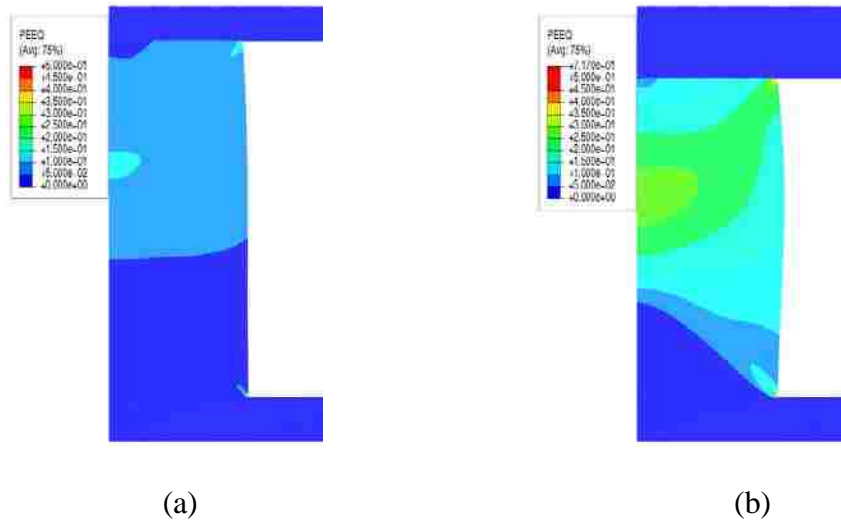


Figure 8.11: Equivalent plastic strain of the pure Al pillar with a 2° taper angle at compression depths of (a) 100 nm. and (b) 325 nm.

Figure 8.12 (a), (b) and (c) show the Von Mises stress contours of the multilayer pillar, with no taper, at compression depths of 100 nm, 200 nm and 325 nm, respectively. It is evident that the Al layers deformed much more than the SiC layers. At greater depths, a significant portion of the soft Al layers was extruded out from the side. This extrusion of Al layer could be the reason that the stress-strain curve of the multilayer pillar is below the curve of true composite. When Al extruded out the overall stress will become smaller than the theoretical stress.

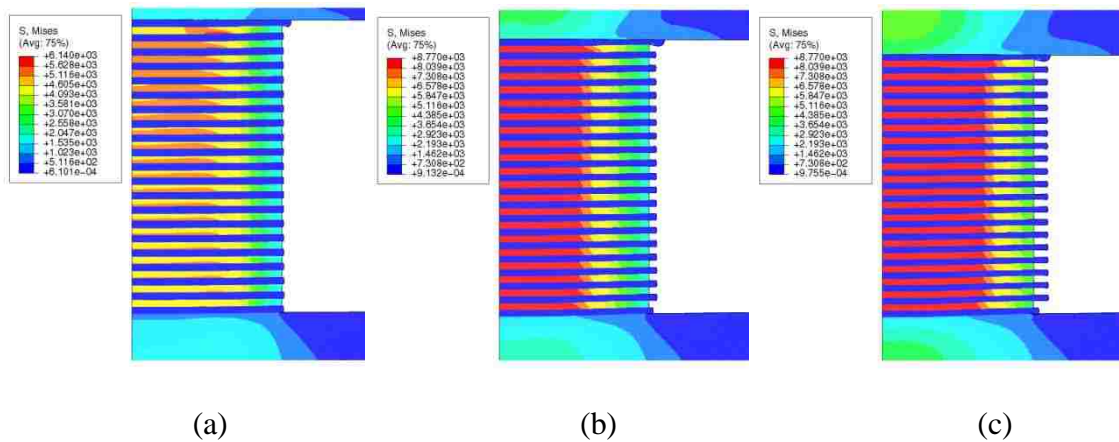


Figure 8.12: Von Mises stress contours of the Al/SiC multilayer pillar on a Si base at compression depths of (a) 100 nm, (b) 200 nm, and (c) 325 nm.

Figure 8.13 (a), (b) and (c) show the Von Mises stress contours of the multilayer pillar model with 2° taper angle at compression depths of 100 nm, 200 nm and 325 nm, respectively. The Al layer deformed much more than SiC layers. It is interesting to observe that, with only a small taper angle, the several Al layers near the top have undergone severe squeezing and were extruded much further out compared to the lower Al layers. It is worth pointing out that,

in the case of a pure Al pillar (Figure 8.11), such type of deformation was not observed even with taper. The uneven extrusion of Al is caused by the multilayer arrangement.

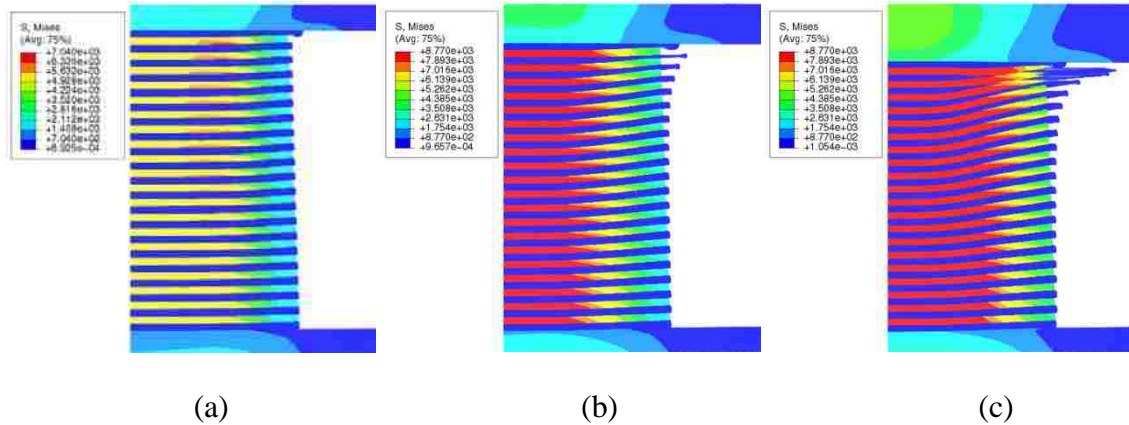


Figure 8.13: Von Mises stress contours of the Al/SiC multilayer pillar on a Si base with a 2° taper angle at compression depth of (a) 100 nm, (b) 200 nm, and (c) 325 nm.

8.3 Comparison with experiments

The measured overall stress-strain curves of the pillars are currently not available. Here we only focus on the deformed configuration of the Al/SiC multilayer pillar. Figure 8.14 (a) and (b) show the experimental SEM pictures of the pillar before and after, respectively, the compression tests. The 2° taper can be seen in the as-processed specimen (Figure 8.14 (a)). Figure 8.14 (b) shows a dramatic view that the upper half of the pillar has been crushed, while the lower half remains relatively intact. Although the experimental picture at smaller displacement is not available, the severe localization of deformation in the upper portion can still be correlated with the simulated result in Figure 13(c). This comparison, along with the other geometric features studied in the previous sections, serves to illustrate the versatility of

applying finite element modeling in studying the mechanical behavior of nano- and micro-scale materials.

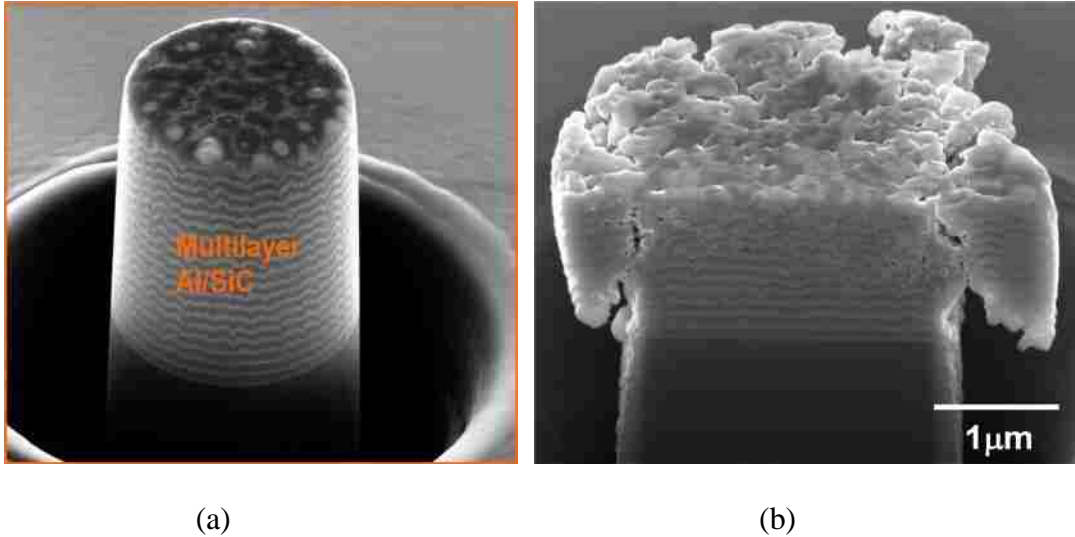


Figure 8.14: SEM images of multilayer pillar structure (a) before compression, and (b) after compression, Courtesy of N. Chawla and D. R. P. Singh

8.4 Conclusions

In a typical micro-pillar structure, the base (substrate) was found to play a significant role in the measured mechanical response. The apparent elastic modulus obtained from the stress-strain curve can be much smaller than the true modulus of the pillar. Correction accounting for the base and indenter compliance is needed. The overall stress-strain curve calculated from the pillar/base model is also significantly lower than that of the true Al/SiC composite. A tapered side wall of the pillar is seen to affect the modulus and stress-strain response only slightly. Taper, however, can affect the overall deformation configuration dramatically. In

the tapered Al/SiC multilayer pillar, the Al layers in the upper portion tend to deform much more severely and protrude sideways. The simulation result can be used to rationalize experimental observations.

Chapter 9 Conclusions and future work

In this research systematic numerical finite element analyses were carried out to study the indentation behavior of nano-scale composite laminates. The model system consists of multilayered Al and SiC thin films above a Si substrate. The main objectives were to gain a comprehensive understanding of how the nanocomposite responds to indentation loading, and to provide support and guidance for the experimental counterpart of this research.

Detailed analyses on the effective composite response, the evolution of deformation fields and their correlation with internal damage, the rate-dependent effect, the assessment of microcompression tests of the pillar structure, as well as many other geometric and material issues related to nanoindentation and microcompression are documented in this dissertation. Conclusions for the individual subtopics were given at the end of each chapter. Here, only several salient findings are summarized.

1. For both the simple film/substrate system and multilayers, the substrate material was found to have a strong influence on the indentation-derived elastic modulus, even when the indentation is relatively shallow. Hardness of the thin film or multilayers, however, is less affected by the substrate.
2. In cases where the influence of substrate does not exist (e.g., “infinite” number of layers), the effective composite elastic modulus can be retrieved when the indentation depth is beyond about several initial layer thicknesses. The composite modulus thus obtained represents the true transverse modulus of the laminates well. The hardness measurement, however, shows an entirely different behavior. Even when the indentation depth is very large (e.g., halfway into the total multilayer thickness), the

- hardness value is still far below the true composite hardness (represented by the homogenized composite).
3. During the unloading phase of the indentation, the soft Al layers can continue to undergo plastic deformation. The unloading response is thus much more complex than the conventional purely elastic recovery process observed in single-phase metals. This observation raises the issue about the accuracy, or even validity, of using instrumented indentation to quantify the elastic behavior of heterogeneous materials.
 4. Using a load-controlled modeling setup, the time-dependent effects in nanoindentation were illustrated. The existence of a hold time after reaching the peak load can help stabilize the indentation response. In comparison with the case of a single film, the multilayered composite displays a less time-dependent behavior.
 5. Results from the compression tests on the micro-pillar structure showed a strong dependence on the specimen geometry. It is essential to correct the raw data by taking into account the compliance of the pillar base and the machine. A tapered side wall affects the overall stress-strain response only slightly. However, in the case of Al/SiC multilayered pillar, a small degree of taper gives rise to severe extrusion of the Al layers out of the side boundary in the top portion of the pillar, leading to a highly non-uniform deformation configuration not seen in pillars made out of a homogeneous material.
 6. A general conclusion, and perhaps the most important one, resulting from this work is that, when performing indentation modeling (including microcompression), it is essential to incorporate the true heterogeneous nature of the composite structure into

the analysis. Homogenizing the composite may lead to very inaccurate results. Important information pertaining to the micro- and nano-scale features may also be lost due to the homogenization.

With the numerical findings listed above, we propose the following areas that merit further research:

1. To better understand the stress and deformation evolution under the indenter, a three-dimensional Berkovich indenter model could be used. It should be interesting to learn how the stress, deformation and pile-up appear under the edge and the side corner of the indenter and compare their difference. It will better explain the internal damages observed experimentally.
2. As discussed in Chapter 5 and 6, the current model utilized an idealized geometry. Some geometrical imperfections may be included in the model and their effects may be characterized. It will be particularly interesting to examine how the evolution of stress field and the continuation of plastic deformation during unloading will be affected by the more realistic model geometry.
3. For the viscoplastic behavior of the material under indentation, studies can be carried out to incorporate a wider range of the loading and unloading rates, different lengths of the holding time, and a more thorough analysis of the time-dependent indentation response of the layered composite. The actual viscoplastic property of Al thin films also need to be characterized experimentally for use as the model input.
4. For the pillar compression model, a more detailed stress-strain comparison between

the simulation and experiment can be carried out. It will be interesting to learn how misalignment between the indenter and the pillar affects the results using finite element modeling.

Overall, it is felt that the current understanding of the indentation behavior of heterogeneous materials is still primitive. This dissertation research may be viewed as an important early step for advancing the status of knowledge in this area.

References

1. D.R. Lesuer, C.K. Syn, O.D. Sherby, J. Wadsworth, J.J. Lewandowski, and W.H. Hunt, Mechanical behavior of laminated metal composites, Int. Mater. Rev., **41**, p. 169-197 (1996).
2. H. Huang and F. Spaepen, Tensile testing of free-standing Cu, Ag and Al thin films and Ag/Cu multilayers, Acta Mater., **48**, p. 3261-3269 (2000).
3. C. Daniel, A. Lasagni and F. Mucklich, Stress and texture evolution of Ni/Al multi-film by laser interference irradiation Surf. Coat. Technol., **180 –181**, p. 478–482 (2004).
4. J. Schumann, W. Brückner, and A. Heinrich, Properties and applications of vacuum-deposited CU-CR films, Thin Solid Films, **228**, p. 44-48 (1993).
5. X. Zhang, A. Misra, H. Wang, T. D. Shen, J. G. Swadener, J. D. Embury, H. Kung, R. G. Hoagland, and M. Nastasi, Strengthening mechanisms in nanostructured copper/304 stainless steel multilayers, J. Mater. Res., **18**, p. 1600-1606 (2003).
6. E. G. Fu, Nan Li, A. Misra, R. G. Hoagland, H. Wang, and X. Zhang, Mechanical properties of sputtered Cu/V and Al/Nb multiplayer films, Mater. Sci. Eng., A, **493**, p. 283-287 (2008).
7. J. B. Vella, A.B. Mann, H. Kung, C.L. Chien, T.P. Weihs, and R.C. Cammarata, Mechanical properties of nanostructured amorphous metal multilayer thin films, J. Mater. Res., **19**, p. 1840-1848 (2004).
8. M. Verdier, H. Huang, F. Spaepen, J. D. Embury and H. Kung, Microstructure, indentation and work hardening of Cu/Ag multilayers, Philos. Mag., **86**, p. 5009-5016 (2006).
9. A.T. Alpas, J.D. Embury, D.A. Hardwick, and R.W. Springer, The mechanical-properties of laminated microscale composites of Al/Al₂O₃, J. Mater. Sci., **25**, p. 1603-1609 (1990).
10. G.T. Mearini and R.W. Hoffman, Tensile properties of aluminum alumina multilayered thin-films, J. Electron. Mater., **22**, p. 623-629 (1993).
11. T.C. Chou, T.G. Nieh, T.Y. Tsui, G.M. Pharr, and W.C. Oliver, Mechanical properties and microstructures of metal ceramic microlaminates. 1. Nb/MoSi₂ systems. J. Mater. Res., **7**, p. 2765-2773 (1992).

12. T.C. Chou, T.G. Nieh, S.D. McAdams, G.M. Pharr, and W.C. Oliver, Mechanical properties and microstructures of metal ceramic microlaminates. 2. A Mo/Al₂O₃ system. J. Mater. Res., **7**, p. 2774-2784 (1992).
13. C.H. Liu, W.Z. Li, and H.D. Li, TiC/metal nanocrystalline structures and their fracture toughness increase, J. Mater. Res., **11**, p. 2231-2235 (1996).
14. Y.L. Shen and S. Suresh, Steady-state creep of metal-ceramic multilayered materials, Acta Mater., **44**, p. 1337-1348 (1996)
15. X. Deng, C. Cleveland, T. Karcher, M. Koopman, N. Chawla, and K.K. Chawla, Nanoindentation behavior of nanolayered metal-ceramic composites, J. Mater. Eng. Perform., **14**, p. 417-423 (2005).
16. H.C. Barshilia, M.S. Prakash, A. Poojari, and K.S. Rajan, Corrosion behavior of nanolayered TiN/NbN multilayer coatings prepared by reactive direct current magnetron sputtering process, Thin Solid Films, **460**, p. 133-142 (2004).
17. D.H. Kuo, and K.H. Tzeng, Characterization and properties of r.f.-sputtered thin films of the alumina-titania system, Thin Solid Films, **460**, p. 327-334 (2004).
18. H. Kung, T. R. Jervis, J. P. Hirvonen, J. D. Embury, T. E. Mitchell, and M. Nastasi, Structure and mechanical properties of MoSi₂-SiC nanolayer composites, Philos. Mag. A, **71**, p. 759-779 (1994).
19. G. Tang, Y.-L. Shen: Indentation Mechanics for Micro- and nano-layered composites, proceedings of MicroNano08, HongKong, July 2008.
20. X. Cai and H. Bangerth, Hardness measurements of thin films-determining the critical ratio of depth to thickness using FEM, Thin Solid Films **264**, 59-71 (1995)
21. V. Teixeira, Mechanical integrity in PVD coatings due to the presence of residual stresses, Thin Solid Films **392**, 276-281, (2001)
22. D.O. Northwood, and A.T. Alpas, Mechanical and tribological properties of nanocrystalline and nanolaminated surface coatings. Nanostruct. Mater., **10**, p. 777-793 (1998).
23. A. A. Voevodin, and J. S. Zabinski, Superhard, functionally gradient, nanolayered and nanocomposite diamond-like carbon coatings for wear protection. Diamond Relat. Mater., **7**, p. 463-467 (1998).
24. M.D. Ben, P. Aubert, S. Labdi, C. Sant, F. A. Sadi, P. Houdy, and J. L. Bozet, Nanoindentation investigation of Ti/TiN multilayers films. J. Appl. Phys., **87**, p. 7753-7757 (2000).

25. J. H. Lee, W.M. Kim, T.S. Lee, M.K. Chung, B.K. Cheong, and S.G. Kim, Mechanical and adhesion properties of Al/AlN multilayered thin films. Surf. Coat. Technol., **133**, p. 220-226 (2000).
26. A. Lousa, J. Romero, E. Martinez, J. Esteve, F. Montala, and L. Carreras, Multilayered chromium/chromium nitride coatings for use in pressure die-casting. Surf. Coat. Technol., **146**, p. 268-273 (2001).
27. T. D. Arcos, P. Oelhafen, U. Aebi, A. Hefti, M. Duggelin, D. Mathys, and R. Guggenheim, Preparation and characterization of TiN-Ag nanocomposite films, Vacuum, **67**, p. 463-470 (2002).
28. J. Romero, A. Lousa, E. Martinez, and J. Esteve, Nanometric chromium/chromium carbide multilayers for tribological applications. Surf. Coat. Technol., **163**, p. 392-397 (2003).
29. M. A. Phillips, B.M. Clemens, and W.D. Nix, Microstructure and nanoindentation hardness of Al/Al₃Sc multilayers. Acta Mater., **51**, p. 3171-3184 (2003).
30. X. Deng, N. Chawla, K.K. Chawla, M. Koopman, and J.P. Chu, Mechanical behavior of multilayered nanoscale meta-ceramic composites. Adv. Eng. Mater., **7**, p. 1099-1108 (2005).
31. N. Chawla, D.R.P. Singh, Y. Shen, G. Tang, and K.K. Chawla, Indentation mechanics and fracture behavior of metal/ceramic nanolaminate composites, J. Mater. Sci., **43**, p. 4383-4390 (2008).
32. N. A. M. Bhattacharyya, R. G. Hoagland, and A. Misra, Nanoindentation and microstructural studies of Al/TiN multilayers with unequal volume fractions, Scr. Mater., **58**, p. 981-984 (2008).
33. Y. Shen, Externally constrained plastic flow in miniaturized metallic structures: A continuum-based approach to thin films, lines, and joints, Prog. Mater. Sci., **53**, p. 838-891 (2008).
34. G. Tang, Y. Shen, and N. Chawla, Plastic deformation during indentation unloading in multilayered materials, J. Appl. Phys., **104**, p. 116-102 (2008).
35. P. C. Yashar, and W. D. Sproul, Nanometer scale multilayered hard coatings, Vacuum, **55**, p. 179-190 (1999).
36. Z. Xie, M. Hoffman, P. Munroe, A. Bendavid, and P. Martin, Deformation mechanisms of TiN multilayer coatings alternated by ductile or stiff interlayers, Acta Mater., **56**, p. 852-861 (2008).

37. A.C. Fischer-Cripps, Nanoindentation, Springer, New York, p. 20 (2002).
38. J. L.Hay and G. M. Pharr, Instrumented indentation testing, ASM Handbook, vol. 8, Mechanical testing and evaluation, (2003).
39. W. C. Oliver and G. M. Pharr, An improved technique for determining hardness and elastic-modulus using load and displacement sensing indentation experiments, J. Mater. Res., 7, p. 1564-1583, (1992),
40. W.C. Oliver, and G.M. Pharr, Review: Measurement of hardness and elastic modulus by instrumented indentation: Advances in understanding and refinements to methodology, J. Mater. Res., 19, p. 3 - 20 (2004).
41. A. Gouldstone, N. Chollacoop, M. Dao, J. Li, A. M. Minor, and Y.-L. Shen, Indentation across size scales and disciplines: Recent developments in experimentation and modeling. Acta Mater., 55, p. 4015-4039 (2007).
42. Y.-T. Cheng and C.-M. Cheng, Can stress-strain relationship be obtained from indentation curves using conical and pyramidal indenters? J. Mater. Res., 14, p. 3493-3496 (1999).
43. M. Dao, N. Chollacoop, K. J. Van Vliet, T. A. Venkatesh and S. Suresh, Computational modeling of the forward and reverse problems in instrumented sharp indentation, Acta Mater., 49, p. 3899-3918 (2001).
44. C. A. Schuh, Nanoindentation studies of materials, Mater. Today, 9(5), p. 32-40 (2006).
45. M. Zhao, X. Chen, Y. Xiang, J. J. Vlassak, D. Lee, N. Ogasawara, N. Chiba, and Y. X. Gan, Measuring elastoplastic properties of thin films on an elastic substrate using sharp indentation, Acta Mater., 55, p. 6260-6274 (2007).
46. N. Fujisawa, W. Li, and M. V. Swain, Observation and numerical simulation of an elastic-plastic solid loaded by a spherical indenter, J. Mater. Res., 19, p. 3474-3483 (2004).
47. X. Huang, and A. A. Pelegri, Finite element analysis on nanoindentation with friction contact at the film/substrate interface, Compos. Sci. Technol., 67, p. 1311-1319 (2007).
48. T. Y. Tsui, W. C. Oliver and G. M. Pharr, Influences of stress on the measurement of mechanical properties using nanoindentation: Part II. Finite element simulations, J. Mater. Res., 11, p. 760-768 (1996).

49. J. L. Bucaille, S. Stauss, E. Felder and J. Michler, Determination of plastic properties of metals by instrumented indentation using different sharp indenters, Acta Mater., **51**, p. 1663-1678 (2003).
50. N. A. Sakharovaa, J. V. Fernandes, J. M. Antunesa and M. C. Oliveira, Comparison between Berkovich, Vickers and conical indentation tests: A three-dimensional numerical simulation study, Int. J. Solids Struct., **46**, p. 1095-1104 (2009).
51. X. H. Tan and Y.-L. Shen, Modeling analysis of the indentation-derived yield properties of metallic multilayered composites, Compos. Sci. Technol., **65**, p. 1639-1646 (2005).
52. T. Y. Tsui and G. M. Pharr, Substrate effects on nanoindentation mechanical property measurement of soft films on hard substrates, J. Mater. Res., **14**, p. 292-301 (1999).
53. M. D. Uchic, D. M. Dimiduk, J. N. Florando and W. D. Nix, Sample Dimensions Influence Strength and Crystal Plasticity, Science, **305**, p. 986 – 989 (2004).
54. D.M. Dimiduka, M.D. Uchica and T.A. Parthasarathy, Size-affected single-slip behavior of pure nickel microcrystals, Acta Mater., **53**, p. 4065-4077 (2005).
55. J. R. Greera, W.C. Oliverb and W.D. Nix, Nanoscale gold pillars strengthened through dislocation starvation, Phys. Rev. B: Condens. Matter, **73**, 245410 (2006).
56. J. R. Greer, W.C. Oliver and W.D. Nix, Size dependence of mechanical properties of gold at the sub-micron scale, J. Appl. Phys. A, **80**, p. 1625-1629 (2005).
57. J. R. Greer, W.C. Oliver and W.D. Nix, Corrigendum to “Size dependence in mechanical properties of gold at the micron scale in the absence of strain gradients”, Acta Mater., **53**, p. 1821-1830 (2005).
58. K. S. Ng and A.H.W. Ngan, Stochastic nature of plasticity of aluminum micropillars, Acta Mater., **56**, p. 1712-1720 (2008).
59. S. X. Song,¹ Y. H. Lai,² J. C. Huang,² and T. G. Nieh, Homogeneous deformation of Au-based metallic glass micropillars in compression at elevated temperatures, Appl. Phys. Lett., **94**, 061911 (2009).
60. C. A. Volkert, and E. T. Lilleodden, Size effects in the deformation of sub-micron Au columns, Philos. Mag., **86**, p. 5567-5579 (2006).
61. J. Michler, K. Wasmer, S. Meier and F. Östlund, Plastic deformation of gallium arsenide micropillars under uniaxial compression at room temperature, Appl. Phys. Lett., **90**, 043123 (2007).

62. R. Maaß, S. Van Petegem, D. Grolimund, H. Van Swygenhoven, D. Kiener and G. Dehm, Crystal rotation in Cu single crystal micropillars: In situ Laue and electron backscatter diffraction, Appl. Phys. Lett., 92, 071905 (2008).
63. M. Uchic, D. Dimiduk, R. Wheeler, P. Shade and H. Fraser, Application of micro-sample testing to study fundamental aspects of plastic flow, Scr. Mater., 54, p. 759-764 (2006).
64. H. Bei and S. Shim, Effects of focused ion beam milling on the nanomechanical behavior of a molybdenum-alloy single crystal, Appl. Phys. Lett., 91, 111915 (2007).
65. H. Bei, S. Shim, G. Pharr and E. George, Effects of pre-strain on the compressive stress–strain response of Mo-alloy single-crystal micropillars, Acta Mater., 56, p. 4762-4770 (2008).
66. B. Moser, K. Wasmer, L. Barbieri and J. Michler, Strength and fracture of Si micropillars: A new scanning electron microscopy-based micro-compression test, J. Mater. Res., 22, p. 1004-1011 (2007).
67. K. Wasmer, T. Wermelinger, A. Bidiville, R. Spolenak and J. Michler, In situ compression tests on micron-sized silicon pillars by Raman microscopy—Stress measurements and deformation analysis, J. Mater. Res., 23, p. 3040-3047 (2008).
68. D. Kiener, W. Grosinger, G. Dehm and R. Pippan, A further step towards an understanding of size-dependent crystal plasticity: In situ tension experiments of miniaturized single-crystal copper samples, Acta Mater., 56, p. 580-592 (2008).
69. B. E. Schuster, Q. Wei, H. Zhang and K. T. Ramesh, Microcompression of nanocrystalline nickel, Appl. Phys. Lett., 88, 103112 (2006).
70. D. Kiener, C. Motz and G. Dehm, Dislocation-induced crystal rotations in micro-compressed single crystal copper columns, J. Mater. Sci., 43, p. 2503-2506 (2008).
71. M. D. Uchic and D. M. Dimiduk, A methodology to investigate size scale effects in crystalline plasticity using uniaxial compression testing, Mater. Sci. Eng. A, 400-401, p. 268-278 (2004).
72. D. Raabe, D. Ma and F. Roters, Effects of initial orientation, sample geometry and friction on anisotropy and crystallographic orientation changes in single crystal microcompression deformation: A crystal plasticity finite element study, Acta Mater., 55, p. 4567-4583 (2007).
73. H. Zhang, B. E. Schuster, Q. Wei and K. T. Ramesh, The design of accurate micro-compression experiments, Scr. Mater., 54, p. 181-186 (2006).

74. D. R. Lide, Handbook of Chemistry and Physics, 76th ed., CRC Press (1995).
75. J. L. Bucaille, S. Stauss, P. Schwaller, J. Michler, A new technique to determine the elastoplastic properties of thin metallic films using sharp indenters. Thin Solid Films, 447, p. 239-245 (2004).
76. H. Gao, C.-H. Chiu, J. Lee, Elastic contact versus indentation modeling of multi-layered materials. Int. J. Solids Struct., 29, p. 2471-2492 (1992).
77. G. Tang, Y.-L. Shen, D. R. P. Singh and N. Chawla, Analysis of indentation-derived effective elastic modulus of metal-ceramic multilayers, Int. J. Mech. Mater. Des., 4, p. 391-398 (2008).
78. R. M. Jones, Mechanics of Composite Materials. pp.37. Scripta Book Company, Washington, D.C (1975).
79. Y.-L. Shen, M. Finot, A. Needleman, S. Suresh, Effective elastic response of two-phase composites. Acta Metall. Mater., 42, p. 77-97 (1994).
80. T. Wilkins, Y.-L. Shen, Stress enhancement at inclusion particles in aluminum matrix composites: Computational modeling and implications to fatigue damage. Comput. Mater. Sci., 22, p. 291-299 (2001).
81. N. Chawla, and K. K. Chawla, Metal Matrix Composites. pp.146. Springer, New York (2006).
82. G. Tang, D. R. P. Singh, Y.-L. Shen and N. Chawla, Elastic properties of metal-ceramic nanolaminates measured by nanoindentation, Mater. Sci. Eng. A, 502, p. 79-84 (2009).
83. X. Li, and B. Bhushan, A review of nanoindentation continuous stiffness measurement technique and its applications, Mater. Charact., 48, p. 11-36 (2002).
84. Y.-L. Shen, J. J. Williams, G. Piotrowski, N. Chawla and Y. L. Guo, Correlation between tensile and indentation behavior of particle-reinforced metal matrix composites: An experimental and numerical study, Acta Mater., 49, p. 3219-3229 (2001).
85. Y.-L. Shen and N. Chawla, On the correlation between hardness and tensile strength in particle reinforced metal matrix composites, Mater. Sci. Eng. A, 297, p. 44-47 (2001).
86. A. Misra and H. Kung, Deformation behavior of nanostructured metallic multilayers, Adv. Eng. Mater., 3, p. 217-222 (2001).

87. R. G. Hoagland, R. J. Kurtz, and C. H. Henager Jr., Slip resistance of interfaces and the strength of metallic multilayer composites, Scr. Mater., *50*, p. 775-779 (2004).
88. G. Tang and Y.-L. Shen, Effect of material heterogeneity on the evolution of internal deformation during nanoindentation, Int. J. Mater. Struct. Integrity, in press
89. N. Fang, A new quantitative sensitivity analysis of the flow stress of 18 engineering materials in machining, J. Mater. Sci. Technol., *127*, p. 192-196 (2005).
90. A. Widjaja, Discrete dislocation modelling of Nano- and Micro-indentation, <http://dissertations.ub.rug.nl/faculties/science/2007/a.widjaja/>, Chapter 2, (2007).